

VOLUME 37

APRIL 1959

NUMBER 4

# Canadian Journal of Physics

*Editor: H. E. DUCKWORTH*

*Associate Editors:*

L. G. ELLIOTT, *Atomic Energy of Canada, Ltd., Chalk River*  
J. S. FOSTER, *McGill University*  
G. HERZBERG, *National Research Council of Canada*  
L. LEPRINCE-RINGUET, *Ecole Polytechnique, Paris*  
B. W. SARGENT, *Queen's University*  
G. M. VOLKOFF, *University of British Columbia*  
W. H. WATSON, *University of Toronto*  
G. A. WOONTON, *McGill University*

*Published by THE NATIONAL RESEARCH COUNCIL*  
OTTAWA CANADA

## CANADIAN JOURNAL OF PHYSICS

Under the authority of the Chairman of the Committee of the Privy Council on Scientific and Industrial Research, the National Research Council issues THE CANADIAN JOURNAL OF PHYSICS and five other journals devoted to the publication, in English or French, of the results of original scientific research. Matters of general policy concerning these journals are the responsibility of a joint Editorial Board consisting of: members representing the National Research Council of Canada; the Editors of the Journals; and members representing the Royal Society of Canada and four other scientific societies.

### EDITORIAL BOARD

#### Representatives of the National Research Council

I. McT. Cowan, *University of British Columbia*  
A. Gauthier, *University of Montreal*

H. G. Thode (Chairman), *McMaster University*  
D. L. Thomson, *McGill University*

#### Editors of the Journals

D. L. Bailey, *University of Toronto*  
T. W. M. Cameron, *Macdonald College*  
H. E. Duckworth, *McMaster University*

K. A. C. Elliott, *Montreal Neurological Institute*  
Léo Marion, *National Research Council*  
R. G. E. Murray, *University of Western Ontario*

#### Representatives of Societies

D. L. Bailey, *University of Toronto*  
Royal Society of Canada  
T. W. M. Cameron, *Macdonald College*  
Royal Society of Canada  
H. E. Duckworth, *McMaster University*  
Royal Society of Canada  
Canadian Association of Physicists

K. A. C. Elliott, *Montreal Neurological Institute*  
Canadian Physiological Society  
P. R. Gendron, *University of Ottawa*  
Chemical Institute of Canada  
R. G. E. Murray, *University of Western Ontario*  
Canadian Society of Microbiologists  
T. Thorvaldson, *University of Saskatchewan*  
Royal Society of Canada

#### Ex officio

Léo Marion (Editor-in-Chief), *National Research Council*  
J. B. Marshall (Administration and Awards), *National Research Council*

---

*Manuscripts* for publication should be submitted to Dr. H. E. Duckworth, Editor, Canadian Journal of Physics, Hamilton College, McMaster University, Hamilton, Ontario.  
For instructions on preparation of copy, see **NOTES TO CONTRIBUTORS** (back cover).

*Proof, correspondence concerning proof, and orders for reprints* should be sent to the Manager, Editorial Office (Research Journals), Division of Administration and Awards, National Research Council, Ottawa 2, Canada.

*Subscriptions, renewals, requests for single or back numbers, and all remittances* should be sent to Division of Administration and Awards, National Research Council, Ottawa 2, Canada. Remittances should be made payable to the Receiver General of Canada, credit National Research Council.

The journals published, frequency of publication, and prices are:

Canadian Journal of Biochemistry and Physiology	Monthly	\$9.00 a year
Canadian Journal of Botany	Bimonthly	\$6.00 a year
Canadian Journal of Chemistry	Monthly	\$12.00 a year
Canadian Journal of Microbiology	Bimonthly	\$6.00 a year
Canadian Journal of Physics	Monthly	\$9.00 a year
Canadian Journal of Zoology	Bimonthly	\$5.00 a year

The price of regular single numbers of all journals is \$2.00.





# Canadian Journal of Physics

*Issued by THE NATIONAL RESEARCH COUNCIL OF CANADA*

VOLUME 37

APRIL 1959

NUMBER 4

## RADIOACTIVE DECAY OF $\text{Au}^{200}$ <sup>1</sup>

J. C. ROY AND L. P. ROY

### ABSTRACT

The half-life of  $\text{Au}^{200}$  has been measured to be  $48.4 \pm 0.3$  minutes. The beta radiations emitted in the decay of  $\text{Au}^{200}$  have been studied by absorption in aluminum, and the gamma radiations with a multichannel scintillation spectrometer. Two beta rays with end-point energies of  $2.25 \pm 0.20$  and  $0.7 \pm 0.1$  Mev and respective abundance of  $(75 \pm 3)\%$  and  $(25 \pm 3)\%$  were detected. Three gamma rays with energies of 0.367, 1.23, and 1.60 Mev were observed. It was established that the 0.367- and 1.23-Mev gamma rays are in coincidence. A decay scheme for  $\text{Au}^{200}$  is proposed.

### INTRODUCTION

A 48-minute activity in gold which was produced by the  $(n, p)$  reaction on mercury and by the  $(n, \alpha)$  reaction on thallium was first reported by Sherr *et al.* (1941) and Maurer and Ramm (1942). The activity was assigned to  $\text{Au}^{200}$ . Butement and Shillito (1952) by studying  $(\gamma, p)$  reactions on enriched isotopes of mercury showed that the mass assignment was correct. Sherr *et al.* (1941) established that  $\text{Au}^{200}$  emits an energetic beta ray with a maximum energy of about 2.5 Mev. Butement and Shillito observed two gamma rays of energies 0.39 and 1.13 Mev with beta rays of maximum energy of 2.2 Mev; the  $\beta/\gamma$  ratio was found to be 5. Preliminary results by Roy *et al.* (1957) indicated that the energy of one of these gamma rays is 1.23 Mev rather than 1.13 Mev and additional observations on the beta and gamma radiations from the decay of  $\text{Au}^{200}$  are reported here.

### EXPERIMENTAL

Sources of  $\text{Au}^{200}$  were obtained through the decay of  $\text{Pt}^{200}$ , formed by successive neutron capture in  $\text{Pt}^{198}$ . An experiment consisted in the irradiation of 0.5 to 1.0 g of natural platinum for 16 hours in the NRX reactor at a neutron flux of about  $7 \times 10^{13}$  n/cm<sup>2</sup> sec. One day after the end of the irradiation the  $\text{Au}^{199}$  produced by the decay of the 30-minute  $\text{Pt}^{199}$  was removed. Then  $\text{Au}^{200}$ , daughter of  $\text{Pt}^{200}$ , was separated and chemically purified. The parent-daughter separations were repeated at intervals of several hours. The details of the

<sup>1</sup>Manuscript received December 19, 1958.

Contribution from Research Chemistry Branch, Atomic Energy of Canada Limited, Chalk River, Ontario.

Issued as A.E.C.L. No. 762.

separation and purification have been described elsewhere (Roy *et al.* 1957). The activities of the sources were of the order of  $10^2$  to  $10^3$  disintegrations per second at the beginning of the measurement. The low activity of the source prevented a detailed investigation of the radiations of  $\text{Au}^{200}$ ; only the prominent beta and gamma rays could be identified positively.

The beta radiations were studied with an anthracene beta counter. The distance between source and window was 2.0 cm and the window thickness was 2.16 mg/cm<sup>2</sup>. The maximum energies of the beta radiations were estimated from an absorption curve made with aluminum absorbers by the method of Harley and Hallden (1955).

The gamma-ray spectrum was examined with a 1½ in.  $\times$  1 in. and a 3 in.  $\times$  3 in. NaI(Tl) scintillation spectrometer. The photomultiplier tubes were an RCA 5819 and a Dumont 6818 for the smaller and larger crystal respectively and the pulses were registered in a multichannel analyzer (Moody *et al.* 1951). The coincidence experiments were done with two 1½ in.  $\times$  1 in. NaI(Tl) crystals placed about 1 in. apart. All  $\gamma$ -ray pulses above a variable bias detected in one crystal were used to gate  $\gamma$ -ray pulses from the other crystal. In this way  $\gamma$ -ray pulses in coincidence with all pulses above the selected bias were accepted for display on a 30-channel pulse height analyzer. The apparatus was set up and calibrated with  $\text{Na}^{22}$  and  $\text{Co}^{60}$ .

## RESULTS

### A. Half-Life Determinations

The half-life of  $\text{Au}^{200}$  was measured by following the decay of the beta radiations with an anthracene crystal coupled to a RCA 6199 photomultiplier tube. The discriminator bias was set to accept all the pulses with an energy higher than 15 kev. A decay curve of one of the  $\text{Au}^{200}$  samples, corrected for the background of the counter and the presence of a residual  $\text{Au}^{199}$  activity, is shown in Fig. 1. The background of the counter was  $10 \pm 0.5$  counts per

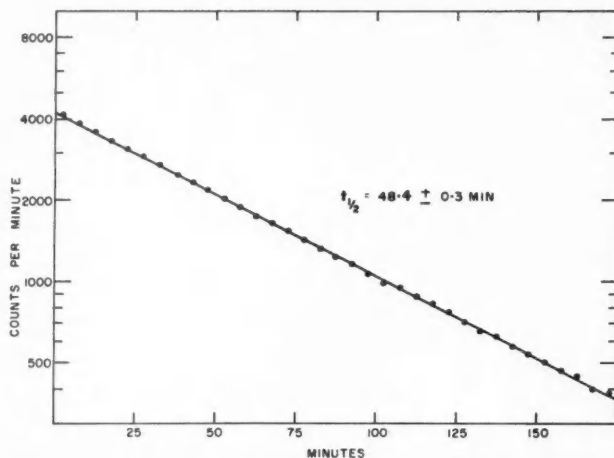


FIG. 1. Decay curve of  $\text{Au}^{200}$ , obtained from the decay of the beta radiations.

minute and the Au<sup>199</sup> activity was of the order of 30 to 50 counts per minute. Table I summarizes the results on the half-life determinations. These results

TABLE I  
Determination of the half-life of Au<sup>200</sup>

Experiment No.	Au <sup>200</sup> activity, counts/min	Total background, counts/min	Time obs., half-lives	Half-life, minutes
1	2000	40	3	48.39
2	4240	64	4	48.34
3	8140	42	4	48.32
4	6780	56	4	48.65

NOTE: Average of  $48.43 \pm 0.15$  minutes where the error is the standard deviation.

were subjected to analysis by the method of least squares and gave an average of  $48.4 \pm 0.3$  minutes; the standard deviation was doubled to take into account unknown systematic errors. The value is in agreement with the 48-minute period reported by earlier investigators.

#### B. Gamma Radiations

The NaI (Tl) pulse height distribution from the gamma rays of an Au<sup>200</sup> source is shown in Figs. 2, 3, and 4. The various peaks in the distribution, which were observed to decay with a half-life of 48 minutes, were assigned to Au<sup>200</sup>. They are interpreted as indicating the presence of three gamma rays

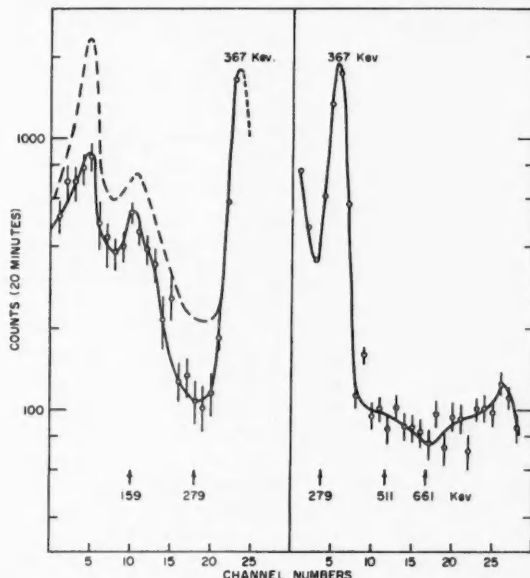


FIG. 2. Pulse height distribution of Au<sup>200</sup> from .03 to 1.0 Mev, taken with a 1 1/2 in.  $\times$  1 in. NaI(Tl) crystal. The dotted line on the left is the distribution before the subtraction of the residual background.

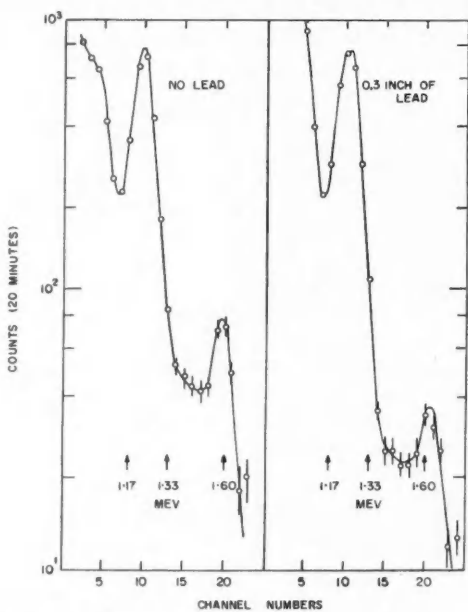


FIG. 3. Pulse height distribution of  $\text{Au}^{200}$  from 1.0 to 1.8 Mev, taken with a  $1\frac{1}{4}$  in.  $\times$  1 in. NaI(Tl) crystal. The spectrum shown on the right was taken through 0.3 in. of lead.

with energies of  $0.367 \pm 0.005$ ,  $1.23 \pm 0.01$ , and  $1.60 \pm 0.02$  Mev. The relative intensities of the 0.367- and 1.23-Mev radiations corrected for internal conversion are the same within  $\pm 5\%$ . The  $K$ -conversion coefficient for the 0.367-Mev  $\gamma$ -ray was taken to be 0.04 and the  $K/L$  ratio as 2.5 (Herrlander and Gerholm 1957). The pulse height distribution below 200 kev has been obtained after the subtraction of a large background due to the soft gamma rays emitted by the platinum isotopes still present in the  $\text{Au}^{200}$  sources. A large error is associated with each point forming the distribution in that region especially around 70 kev where the background was about equal to the activity of the sample. The peaks at 70 and 160 kev could be attributed respectively to  $K$  X rays from  $K$ -conversion and to the backscattering of the 0.367-Mev gamma ray; their intensity relative to 0.367-Mev gamma would be consistent with that interpretation. However, the presence of a gamma radiation in low abundance in that range cannot be ruled out on the basis of these data.

The peak at 1.60 Mev, shown on the spectra of Figs. 3 and 4, arises in part from the summation of the 0.367- and 1.23-Mev radiations. It was established that half of the intensity of the peak at 1.60 Mev is due to a gamma transition in the decay of  $\text{Au}^{200}$  by selective absorption of the 0.367-Mev radiation in 0.3 inch of lead (right side of Fig. 3). The intensity of the 1.60-Mev gamma ray is about 5% of that of the 1.23-Mev radiation.

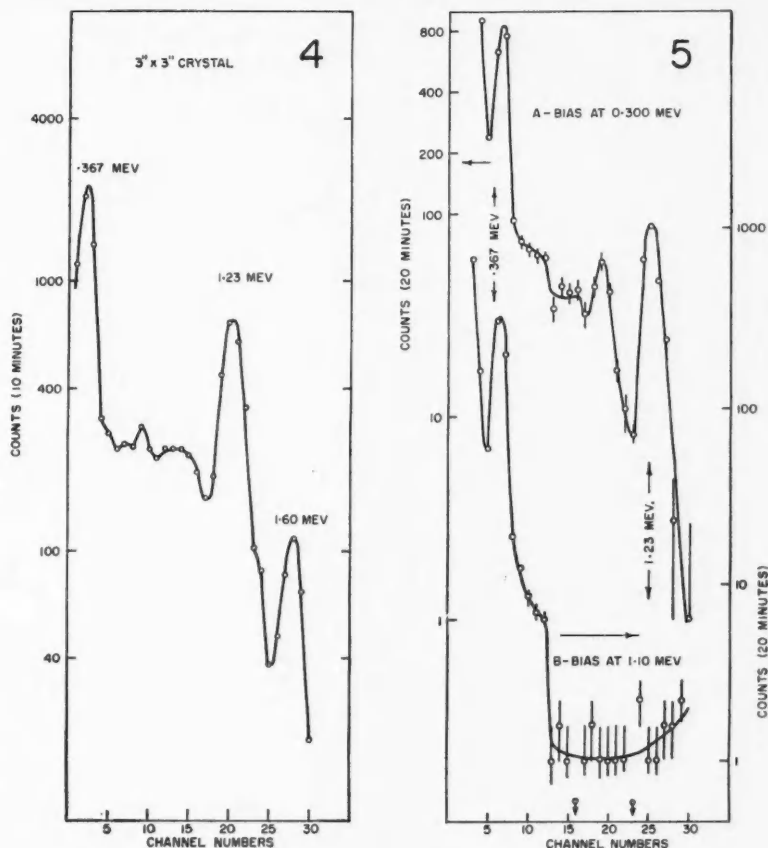


FIG. 4. Pulse height distribution of  $Au^{200}$  taken with a 3 in.  $\times$  3 in. NaI(Tl) crystal.  
 FIG. 5. Gamma-gamma coincidence spectra. The scale on the left is for spectrum A; on the right for spectrum B.

The gamma-gamma coincidence pulse height distribution of  $Au^{200}$ , shown in Fig. 5, indicates that the 0.367- and 1.230-Mev  $\gamma$ -rays are in coincidence. In B the variable bias of one spectrometer was selected to accept only the 1.23 Mev radiation; in A it was selected to accept both the 0.367- and 1.23-Mev radiations.

Special care has been taken to determine the energies of the 0.367- and 1.23-Mev  $\gamma$ -rays: the photopeaks of  $Hg^{203}$ ,  $Au^{198}$ ,  $Na^{22}$ , and  $Co^{60}$  at 0.279, 0.411, 0.511, 1.28, 1.17, and 1.33 Mev respectively were used as calibration lines. The errors assigned to the  $\gamma$ -ray energies are the estimated accuracies of the measurements.

### C. Beta Radiations

The beta-absorption curve of  $\text{Au}^{200}$  in aluminum is shown in Fig. 6; each point represents the average of four independent determinations. The method

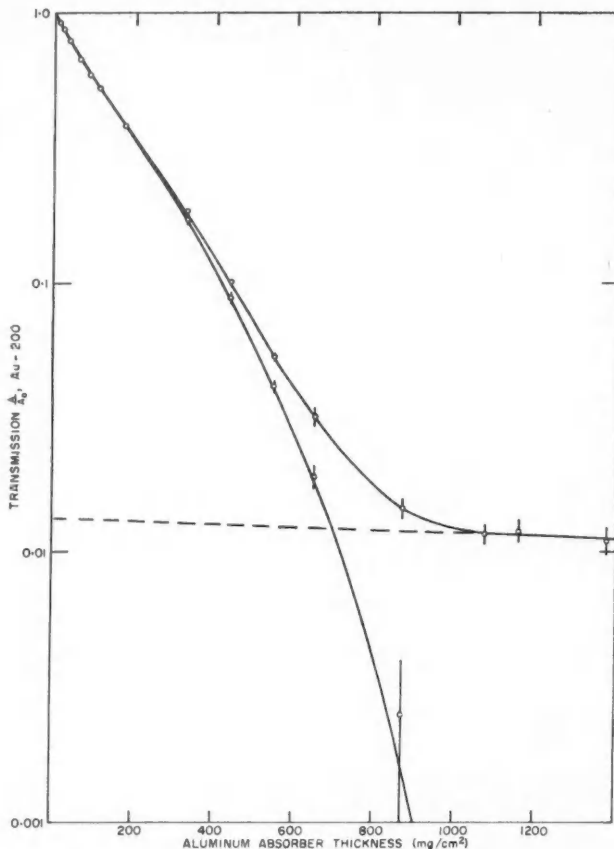


FIG. 6. Absorption curve of  $\text{Au}^{200}$  with aluminum absorbers.

of Harley and Hallden (1955) was used to analyze the beta-absorption curve and to determine the maximum energy of the beta components. The method is based on comparing the transmissions of an unknown and a standard emitter with the same absorber. When the logarithms of the transmissions of the two emitters are plotted against each other for each absorber, a linear relationship is found; a deviation from linearity indicates a complex beta spectrum. Duncan and Thomas (1957) have compared the three beta-absorption methods and have concluded that Harley-Hallden approach is the best

for a short-lived beta emitter when only low activities are available. It can give an accuracy of  $\pm 10\%$  under our experimental conditions.

In the present work the transmissions of  $Au^{200}$  were plotted against those of the following beta emitters:  $P^{32}$ ,  $Sr^{89}$ ,  $Y^{90}$ ,  $Cd^{115}$ , and  $Pr^{142}$ . Figure 7 shows the plot of  $P^{32}$  versus  $Au^{200}$ . With all the standards, there was a marked deviation

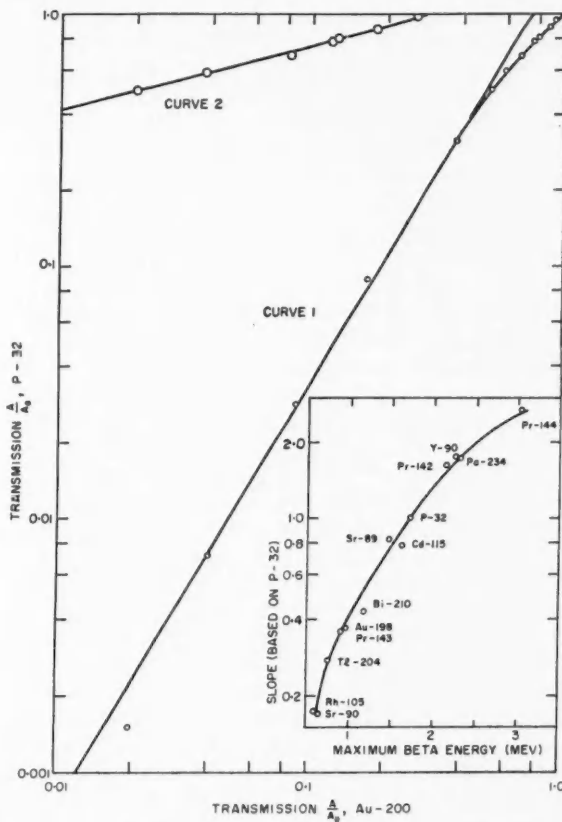


FIG. 7. Harley-Hallden curves for  $Au^{200}$ .  $P^{32}$  is the standard. Curve 1 is the contribution of the energetic component, curve 2 that of the soft component. In the figure at the bottom corner, the slopes of logarithmic curves that used  $P^{32}$  as standard are plotted versus maximum beta energy of different beta emitters.

from linearity, indicating the presence of soft beta radiations. The extrapolation of the linear portion of the transmission curve to unity on the abscissa gives the relative concentration of the more energetic component. Replotting the horizontal difference between the extrapolated and experimental curves against the  $P^{32}$  values for the same absorbers gives curve 2 in Fig. 7,

the contribution of the soft component. The mean of the five transmission curves gives a relative abundance of  $(74 \pm 5)\%$  and  $(26 \pm 5)\%$  for the energetic and soft beta components respectively. The maximum energy of each component was estimated from the slope-energy curve given at the bottom of Fig. 7. The slope-energy curve was constructed from the absorption curves of 14 beta emitters, taken under the same conditions as that of  $\text{Au}^{200}$ . The slope of the line for the energetic beta,  $\beta_1$  (curve 1 in Fig. 7), is 1.67 giving a maximum energy of  $2.25 \pm 0.2$  Mev; that of the soft component,  $\beta_2$  (curve 2 in Fig. 7), is 0.25 for a maximum energy of  $0.7 \pm 0.1$  Mev.

In one experiment the ratio of the total beta disintegrations,  $\beta_1 + \beta_2$ , to the abundance of the 1.23- plus the 1.60-Mev gamma disintegrations were determined. It was done by measuring first the disintegration rate of the gamma radiations of a given source of  $\text{Au}^{200}$  on the scintillation spectrometer; then the disintegration rate of the beta radiations from the same source of  $\text{Au}^{200}$  was measured on the beta-anthracene counter. From the known efficiencies of each detector and after correcting for the decay of the sample between the measurements, the ratio  $(\beta_1 + \beta_2)/\gamma$  ( $\gamma$  is the 1.23- plus the 1.60-Mev  $\gamma$ -rays) was found to be  $4.0 \pm 0.4$ . From this value of the ratio, the upper beta branch,  $\beta_2$ , is found to be  $(25 \pm 3)\%$ ; the other branch,  $\beta_1$ , becomes then  $(75 \pm 3)\%$ . These results are more accurate than those obtained from the absorption experiments. They are therefore considered as the best values for the relative abundance of  $\beta_2$  and  $\beta_1$  respectively.

#### DISCUSSION

Gold-200 decays to  $\text{Hg}^{200}$  and before discussing the characteristics of the  $\text{Au}^{200}$  transitions the available information on the excited states of  $\text{Hg}^{200}$ , reviewed recently by Herrlander and Gerholm (1957), will be presented.

Davis *et al.* (1955) and Barloutaud *et al.* (1956) have shown by Coulomb excitation that the first-excited state in  $\text{Hg}^{200}$  is at 368 kev. A large number of gamma rays was found by Israel and Wilkinson (1951), Bergstrom *et al.* (1953), Bergkvist *et al.* (1955), and Herrlander and Gerholm (1957) in the decay of  $\text{Tl}^{200}$ . It has been shown by Wilkinson in unpublished measurements (Bergstrom *et al.* 1953, ref. 3) and by Herrlander and Gerholm (1957) that all the gamma rays were in coincidence with the 368-kev transition. The excited levels in  $\text{Hg}^{200}$  proposed by Herrlander and Gerholm (1957) from the decay of  $\text{Tl}^{200}$  are shown in solid lines in Fig. 8. The spins are indicated when they are known. Adyasevich *et al.* (1955) and Segel (1958) have found low energy levels at 0.37, 0.95, 1.10, 1.59, 1.66, 1.73, 2.02, and 2.10 Mev in the gamma-ray decay in  $\text{Hg}^{200}$  from the reaction  $\text{Hg}^{199}(n, \gamma)\text{Hg}^{200}$ . The major difference between the results obtained from the neutron capture experiments and those from the decay of  $\text{Tl}^{200}$  are the transitions to the ground state which are not observed in the decay of  $\text{Tl}^{200}$ . The levels at 1.10 and 2.02 Mev in dotted lines in Fig. 8 have not been observed in the decay of  $\text{Tl}^{200}$ .

In the decay of  $\text{Au}^{200}$ , the 0.367-Mev  $\gamma$ -ray is the well-known transition from the first-excited to the ground state; the 1.23-Mev  $\gamma$ -ray is a transition from the 1.594 to the 0.367-Mev level as seen in Fig. 8. There is no doubt that

these two gamma rays are the same as those observed by Butement and Shillito (1952) at about 0.39 and 1.13 Mev. The low intensity 1.60-Mev  $\gamma$ -ray is interpreted as a crossover transition of the 1.594-Mev level to the ground state.

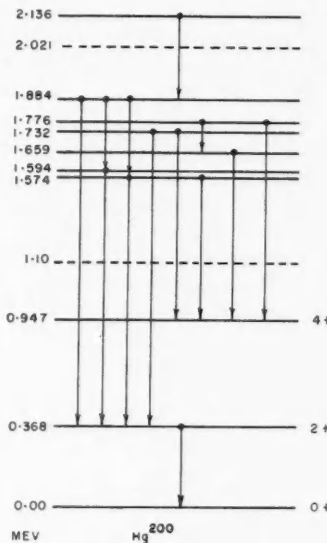


FIG. 8. Excited states of Hg<sup>200</sup>.

The data support the conclusion of Wilkinson (Herrlander and Gerholm 1957) that the 1.594 Mev level decays mostly ( $\sim 95\%$ ) to the first-excited state. However, they are in disagreement with the work of Adyasevich *et al.* (1955) and Segel (1958), who concluded that  $\sim 60\%$  of this level decays to the ground state.

No attempt was made to search for beta-gamma coincidences. The activity of Au<sup>200</sup> was too low for such a study. However, some conclusions can be drawn on the nature of the beta transitions from the relative abundances of the beta and gamma radiations. The  $(\beta_2 + \beta_1)/\beta_2$  and  $(\beta_2 + \beta_1)/\gamma$  ratios ( $\gamma$  is the 1.60- plus the 1.230-Mev rays) are the same within experimental error; moreover, the energy of the soft beta,  $\beta_2$ , corresponds to the difference between 2.25 Mev, the energy of  $\beta_1$ , and the sum of the two  $\gamma$ -rays at 0.367 and 1.23 Mev. From these facts it is concluded that  $\beta_2$  goes to the 1.597-Mev level and  $\beta_1$  to the ground state of Hg<sup>200</sup>. From the fact that the 0.367- and 1.23-Mev gamma rays have the same intensities within  $\pm 5\%$ , an upper limit of 3% can be set for the beta transition to the 0.367 level.

The log  $ft$  of 7.0 for the  $\beta_1$  transition which was calculated by the method of Moszkowski (1951) is consistent with a first-forbidden transition with

spin changes of 0 or 1 and parity change. This means that the spin of  $\text{Au}^{200}$  in the ground state is either  $1^-$  or  $0^-$ .

The 79th proton is found to be in the  $d_{3/2}$  state in  $\text{Au}^{197}$  and  $\text{Au}^{199}$  and this is accepted also for the other isotopes of gold (Bergstrom and Andersson 1957; Zeldes 1958). The 121st neutron is found to be in  $p_{3/2}$  state in  $\text{Hg}^{201}$ , but for  $\text{Pb}^{203}$  it is believed to be in the  $f_{5/2}$  state (Bergstrom and Andersson 1957). If one accepts the interpretation that the 79th proton and the 121st neutron in  $\text{Au}^{200}$  are in the  $d_{3/2}$  and  $p_{3/2}$  states respectively, their spins are antiparallel and therefore according to Nordheim's strong rule (Nordheim 1951) the spin of the ground state in  $\text{Au}^{200}$  would be  $0^-$ . The experimental results favor such a spin. In fact, if the spin of the ground state in  $\text{Au}^{200}$  were  $1^-$ , the transitions to the first-excited and ground states would be of the same degree of forbiddenness and therefore the beta branching to the two states should be roughly equal. This is not the case, since only one beta is seen in the high energy part of the absorption and transmission curves in Figs. 6 and 7. Moreover a transition to the first-excited state would have made the abundance ratio of the gamma rays at 0.367 and 1.23 Mev greater than one.

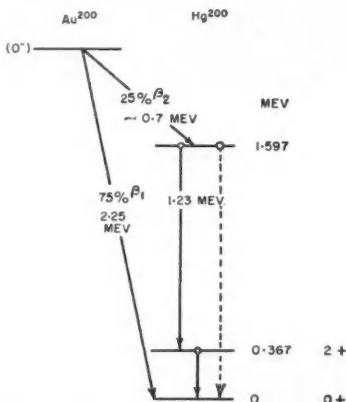


FIG. 9. Proposed decay scheme of  $\text{Au}^{200}$ .

In Fig. 9 a decay scheme for  $\text{Au}^{200}$  has been constructed which is consistent with our results and those obtained by Herrlander and Gerholm (1957) on the decay of  $\text{Tl}^{200}$ .

#### ACKNOWLEDGMENTS

The authors wish to thank Dr. T. A. Eastwood and D. A. S. Walker for their assistance in setting up the coincidence spectrometer, R. C. Hawkinings for the use of the 3 in.  $\times$  3 in. crystal, and Mrs. J. S. Merritt for the preparation of standard sources of  $\text{Na}^{22}$ ,  $\text{Au}^{199}$ , and  $\text{Hg}^{201}$ . We are also indebted to Dr. R. L. Graham of Nuclear Physics for his critical reviews of the manuscript.

## REFERENCES

ADYASEVICH, B. P., GROSHEV, L. V., and DENIDOV, A. N. 1955. Conf. Acad. Sci. U.S.S.R. Peaceful Uses of Atomic Energy, Moscow. Session Div. Phys. Phys. Math. Sci. July, p. 270. Consultants Bureau Trans. p. 195.

BARLOTAUD, R., GRJEBINE, T., and RIOU, M. 1956. Compt. rend. **242**, 1284.

BERGKVIST, K. E., BERGSTROM, I., HERRLANDER, C. J., HULTBERG, S., SLATIS, H., SOKOLOWSKI, E., WAPSTRA, A. H., and WIEDLING, T. 1955. Phil. Mag. **46**, 65.

BERGSTROM, I. and ANDERSSON, G. 1957. Arkiv Fysik, **12**, 415.

BERGSTROM, I., HILL, R. D., and DE PASQUALI, G. 1953. Phys. Rev. **92**, 918.

BUTEMENT, F. D. S. and SHILLITO, R. 1952. Proc. Phys. Soc. (London), A, **65**, 945.

DAVIS, R. H., DIVATIA, A. S., MOFFAT, R. D., and LIND, D. A. 1955. Phys. Rev. **100**, 1266.

DUNCAN, J. F. and THOMAS, F. G. 1957. Nucleonics, **15** (10), 82.

HARLEY, J. and HALDEN, N. 1955. Nucleonics, **13** (1), 32.

HERRLANDER, C. J. and GERHOLM, T. R. 1957. Nuclear Phys. **3** (2), 161.

ISRAEL, H. I. and WILKINSON, R. G. 1951. Phys. Rev. **83**, 1051.

MAURER, W. and RAMM, W. Z. 1942. Z. Physik, **119**, 1602.

MOODY, N. F., BATTELL, W. J., HOWELL, W. D., and TAPLIN, R. H. 1951. Rev. Sci. Instr. **22**, 551.

MOSZKOWSKI, S. A. 1951. Phys. Rev. **82**, 35.

NORDHEIM, L. W. 1951. Revs. Modern Phys. **23**, 322.

ROY, L. P., ROY, J. C., and MERRITT, J. S. 1957. Phys. Rev. **105**, 1337.

SEGEL, R. E. 1958. Phys. Rev. **111**, 1620.

SHERR, R., BAINBRIDGE, K. T., and ANDERSON, H. H. 1941. Phys. Rev. **60**, 473.

ZELDES, N. 1958. Nuclear Phys. **7** (1), 27.

# MEASUREMENT OF THE ENERGIES OF NUCLEAR STATES EXCITED BY INELASTIC NEUTRON SCATTERING, AND A SEARCH FOR ELECTRIC MONOPOLE TRANSITIONS IN Pb<sup>1</sup>

J. E. EVANS, B. B. KINSEY,<sup>2</sup> AND B. G. WHITMORE<sup>3</sup>

## ABSTRACT

A method of measuring the energies of nuclear states excited by inelastic neutron scattering is described, in which an energy-selective detector is used. The neutron source was Li or H<sup>3</sup> bombarded by protons from a Van de Graaff generator. The ratio of the counting rate produced in this detector by the material under study to that produced by a long counter was plotted against the proton energy. Peaks in this curve occur when the energy of the scattered neutrons is equal to the resonance energy of the selective detector (255 kev). The energies of the excited states responsible for these neutrons were determined with some precision by a step-by-step comparison with those produced by a standard material for which the energies of the excited states are already well known (e.g. Fe<sup>56</sup>). A weak peak, not corresponding to any known state, was found in Zr. Two states in Fe<sup>56</sup> were used to determine the energies of peaks obtained from Pb. One of these was that due to the well-known state at 2.62 Mev. However, peaks were observed corresponding to both lower and higher energies, none of which agree with those of known excited states. Except for that caused by the 803-kev state of Pb<sup>206</sup>, no other peaks were observed from a target of Pb<sup>208</sup>. Th<sup>232</sup> produced strong peaks corresponding to excited states at 760 and 1080 kev; U<sup>238</sup> produced a peak at 710 kev and another (unresolved from higher energy peaks) at 940 kev. Both peaks near 700 kev from these two nuclei showed unresolved structure.

A peak was found from natural Pb corresponding to an excited state at 3.185 Mev. Reasons are given for believing that this state is 0<sup>+</sup>. An unsuccessful search was made for annihilation radiation using coincident NaI crystals in a rectilinear arrangement. This apparatus detected readily the pair production from the 0<sup>+</sup> state in Zr<sup>90</sup>, but was apparently responsible for a spurious effect in Pb. If pairs are emitted by a 3.185-Mev state in Pb<sup>208</sup>, the cross section for this process for neutrons with energy 0.5 Mev above threshold is probably less than one half of that from Zr<sup>90</sup> for an equal energy excess above threshold.

## 1. INTRODUCTION

Bonner and his associates (1954) have used slow neutron detectors to determine the energies of neutrons emitted by various targets. Such detectors, responding to neutrons in a limited energy range, mark the 'threshold' at which a group of neutrons passes a specified energy. Selective scattering of neutrons of a definite energy from resonance scatterers has been used by Stelson and Preston (1951a) for similar purposes. In this paper we describe a modification of the latter method adapted to the determination of the energies of inelastically scattered neutrons. For the resonance scatterer we have used lithium, for which the resonance energy is 255 kev (Stelson and Preston 1951b) with a width at half-maximum cross section of 30 kev. Lithium has only one sharp resonance over a wide range of neutron energies. Attempts to use the 110-kev resonance in sulphur were not very satisfactory owing to the effects of resonances at higher energies. An elementary calculation on the

<sup>1</sup>Manuscript received January 9, 1959.

Contribution from the Atomic Energy Research Establishment, Harwell, England.

<sup>2</sup>Now at the University of Texas, Austin, Texas.

<sup>3</sup>On leave of absence from the University of Manitoba, Winnipeg, Manitoba.

basis of Hauser and Feshbach's theory (1952) shows that, in intermediate and heavy nuclei, the only states in the target nucleus which are excited to a degree sufficient to enable the inelastically scattered neutrons to be detected by this method are those for which the spins differ by 3 units or less from that of the target nucleus. This method of excitation, therefore, is of limited application. However, our present knowledge of the level structure of many nuclei is largely dependent on studies of  $\gamma$ -emission following  $\beta$ -decay, and the level sequence so disclosed is selected mainly by the difference in spins between the ground states and daughter nuclei. The present method, therefore, can be of value in finding states not excited in  $\beta$ -decay; it can also be useful in finding levels in heavy nuclei, which, because of the Coulomb barrier, are not easily excited by bombardment by charged particles.

## 2. EXPERIMENTAL METHOD

The apparatus is shown in Fig. 1. The neutron source consisted, for the lowest neutron energies, of LiF bombarded by protons, and for higher energies, of tritium absorbed in Ti. Both materials were mounted on gold foils in a

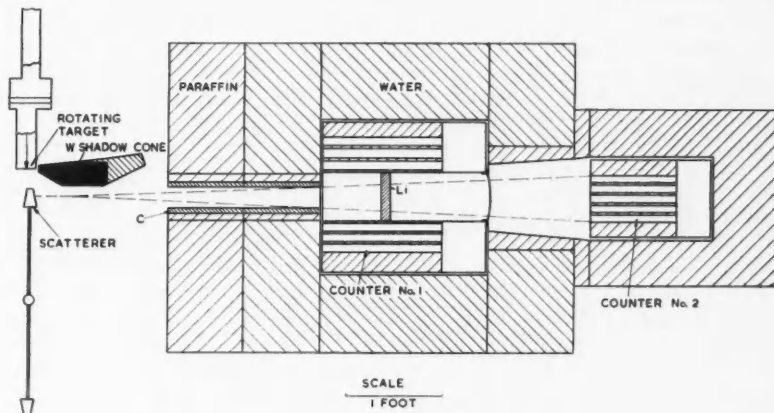


FIG. 1. Experimental arrangement.

rotating assembly and bombarded by protons from a Van de Graaff accelerator. The exact location of the position where the beam hits these targets was very important because the screening of the neutrons from the detectors (and therefore the background counting rates) was critically dependent on it. The target to be examined was made in the form of a truncated cone, the angle in the apex being  $30^\circ$ ; it was mounted on a horizontal axis on to a thin steel tube attached to a vertical rotatable support. Turning this shaft through  $180^\circ$  allowed the target under examination to be replaced by another in an identical position. To ensure that the part of the target bombarded by the proton beam was always opposite the apex of the cone, the proton beam was

limited by a  $\frac{1}{4}$ -in. diameter hole in a tantalum plate, placed 12 inches in front of the target, the beam alignment being made by replacing the target by a quartz plate. The detector consisted of some 35  $\text{B}^{10}\text{F}_3$  counters embedded in paraffin and mounted cylindrically round the resonance scatterer, a plate of Li metal, 1 in. thick and 5 in. in diameter, cast into a thin steel can. This secondary scatterer (which we shall henceforth call the 'scatterer') lay in full view of the primary scatterer (the 'target') and was shielded from the neutron source by a polythene cone tipped with a wedge of tungsten. A monitoring counter, consisting of some eight  $\text{B}^{10}\text{F}_3$  counters, likewise embedded in paraffin, was placed behind the scatterer, with its center on an axis passing through the centers of target and scatterer. Both counters were screened with water tanks and paraffin blocks, the neutron beam incident on the scatterer being defined by a conical hole 18 in. deep. The inner surface of this hole, which was cut in paraffin blocks, was lined with graphite.

The experimental procedure consisted in plotting the ratio of the counts recorded by the two sets of counters (for a given proton charge collected at the source) against the proton energy. When neutrons are scattered by the target with an energy near the resonance energy of the scatterer, the number of neutrons scattered by it to the surrounding counters is augmented while the number of those which pass through to the monitor is depleted. The ratio of the counts recorded by the former to that recorded by the latter, when plotted against the proton energy, rises to a peak when the energy of a neutron group is exactly equal to the resonance energy. Thus the energy of the excited state responsible for the neutron group could be calculated from the corresponding proton energy. Precision in such a measurement, however, requires a precise knowledge of the proton energy, the thickness of the neutron source, and the extent to which the neutron energy is degraded in the angle of the cone forming the target. All of these quantities in principle can be determined; however, in the present instrument, the proton energy was known only approximately and it was found more convenient to calibrate the apparatus by comparing the nominal proton energy corresponding to a peak from the material under study with that produced by scattering from a similar cone of a material (e.g., Fe) for which the energies of the excited states are accurately known.

Let  $Q$  and  $Q_0$  be the energy of the state to be determined and that of a state in the comparison material, respectively;  $A$  and  $A_0$  the mass numbers of the nuclei;  $E_n$  the resonant energy of the scatterer; and let  $E$  and  $E_0$  be the energies of the neutrons emitted by the source in the forward direction when the counting rate ratios are at their peak. Then approximately for scattering at  $90^\circ$  to the target:

$$(1) \quad Q - Q_0 = (E - E_0)(1 - 1/A) - (2E_n + Q_0) \cdot (1/A - 1/A_0).$$

Provided the neutrons emitted by the source have an energy of 0.5 Mev or more, it is sufficiently accurate to equate the difference in the neutron energies ( $E - E_0$ ) to the difference in the nominal proton energies corresponding to the peaks in the counting rate ratios. Thus equation (1) will compare the energy

of the excited state under study with that of a known state with a precision depending on the accuracy to which the peak in the counting rate can be plotted. The width of this peak depends mainly on the natural width of the Li resonance (30 kev). In practice the width was somewhat larger than this owing to the effect of target thickness (usually 20 kev), the spread in energies of the neutrons produced by the source within the angle of the target cone (about 15 kev), and effects caused by exponential transmission in the Li scatterer. Usually it was found that the width of a peak at half maximum was about 50 kev and that it was possible to determine  $Q - Q_0$  to an accuracy of 5 to 10 kev.

The collinear arrangement of monitor counter, scatterer, and target has the advantage, as pointed out above, of enhancing the peak in the counting rate ratio. However, it has another important feature. Some materials, like Fe, Ni, and the Pb isotopes, have resonance properties which are responsible for rapid fluctuations in the yield of scattered neutrons as the proton energy is changed. Both sets of counters, however, record numbers of neutrons which, when corrected for backgrounds, are proportional to the neutron emission from the target; their ratio, therefore, is independent of resonance effects.

### 3. EXPERIMENTAL LIMITATIONS

The peak value of the scattering cross section of Li is near 10.8 barns (Stelson and Preston 1951). On either side of the peak the cross section is about 1 barn. On the higher energy side, the cross section rises slowly (Adair 1950) as the energy is increased, reaching 1.5 barn at 1 Mev and 2.3 barns at 4.5 Mev. If it is assumed that the neutrons passing axially through the apparatus are monoergic, the ratio of the peak counting rate ratio to that on either side of the peak is:

$$R = T_0(1 - T_p)/T_p(1 - T_0)$$

where  $T_p$  and  $T_0$  are respectively the transmissions of the Li plate for neutrons at exact resonance, and for neutrons with energies corresponding to the flat part of the cross section curve on either side of it.

The theoretical value of  $R$  for a Li plate 1 in. thick is 17; it increases with increasing thickness. Figure 2 shows the counting rate ratio plotted against the proton energy for a  $\text{Li}(p, n)$  neutron source about 20 kev thick, placed directly in the view of the scatterer. The peak here is about half the theoretical value; presumably this reduction is caused by the spread in neutron energy. When elastically scattered neutrons are detected, the peak is lower still. In this case, the further reduction is caused by the additional spread in energies which derive from the angle of the target cone. Figure 3 shows the peak produced by elastically scattered neutrons from Fe, which (for  $\text{Fe}^{56}$ ) has no low-lying excited state, and from  $\text{Th}^{232}$ , where the effect of the neutrons scattered inelastically to the 50-kev state is clearly shown. Similar results were obtained from  $\text{U}^{238}$ .

It should be possible in principle to obtain weak peaks caused by the

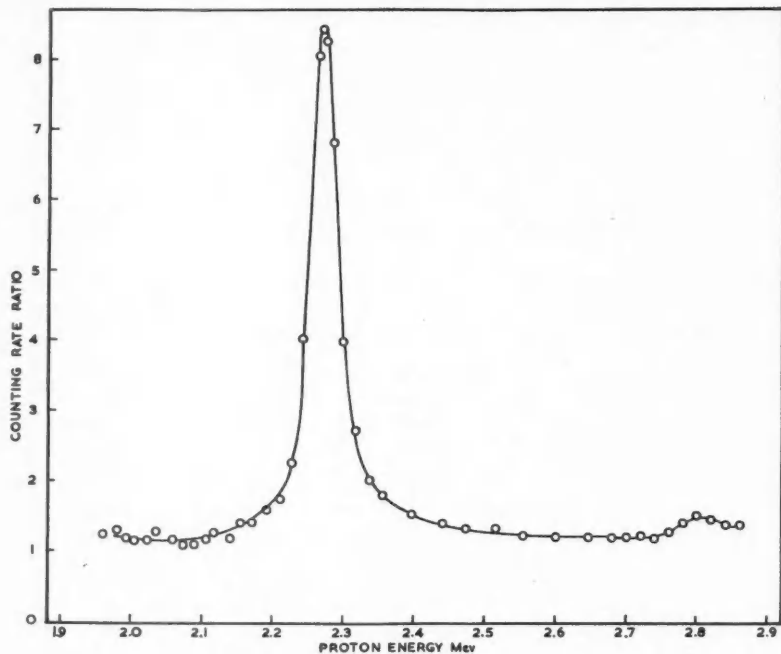


FIG. 2. Counting rate ratio for neutrons emitted from the  $\text{Li}^7(p, n)\text{Be}^7$  reaction.

elastic scattering of neutrons produced by  $(p, n)$  reactions with Ti isotopes. In fact, none were found.

The peaks produced by inelastically scattered neutrons are much less pronounced than those caused by elastically scattered neutrons. Usually the strongest is that caused by the first-excited state. Higher states produce, in general, progressively weaker peaks because the neutrons producing them are in competition with those producing lower-lying states and with the compound-elastic scattering. The peak caused by neutrons producing the 845-kev state in  $\text{Fe}^{56}$  is shown in Fig. 4. The height of this peak is about 1.6 times the counting rate on either side of it. A similar value may be obtained by calculation if it is assumed that the number of inelastically scattered neutrons with an energy of 255 kev is about 1/10th of those scattered elastically, a figure in rough agreement with that to be expected on the basis of Hauser and Feshbach's theory. Theoretical inelastic scattering cross sections leading to states with different spins, calculated for Th, are shown in Fig. 5. It will be seen that the excitation of the  $2^+$  state is much stronger than that of states with higher or lower spin. It is clear that  $4^+$  states and states of higher spin would not be detected.

As pointed out above the width of peaks produced by inelastic scattering

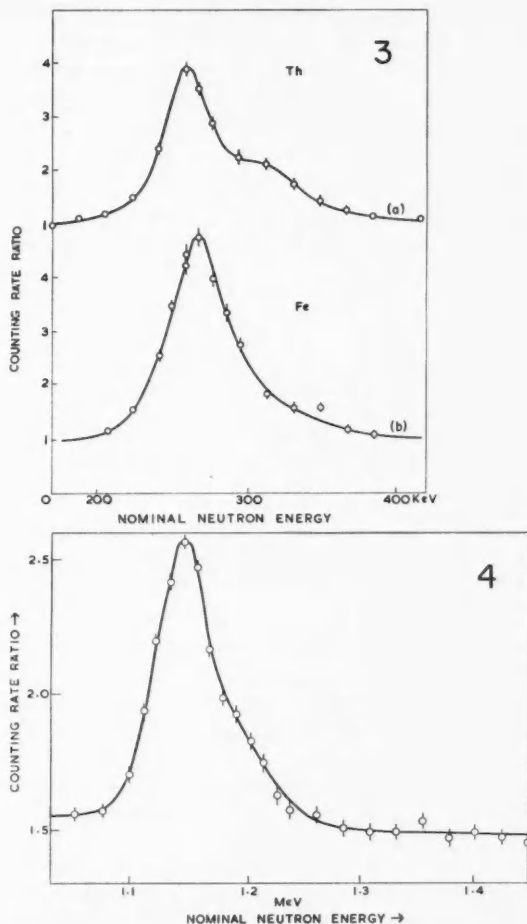


FIG. 3. Counting rate ratio for neutrons scattered elastically by (a) Th, (b) Fe. The Fe peak lies slightly to the right of the Th peak. This is caused by the lower mass of Fe which requires a somewhat higher incident neutron energy for scattering to 90° at exact resonance.

FIG. 4. Counting rate ratio for iron: the peak is caused by the 845-kev state in Fe<sup>58</sup>.

was about 50 kev. Increasing the thickness of the Li plate increases the width of the peak and reduces its height, while reducing the thickness reduces the desired counting rate relative to the background counting rate. The 1-in. plate used in the present measurements represents a compromise between these opposing effects. Higher counting rates were obtained by using wide entrance channels. Increasing the channel diameter, however, increases the background relative to the desired counting rate from the target; the channel diameter

(4 in.) of the present apparatus is a compromise between higher counting rates with high backgrounds obtained by using a wide channel, and low counting rates with relatively lower backgrounds obtained with a narrow channel. Most of the background counting rates were found to be produced by neutrons

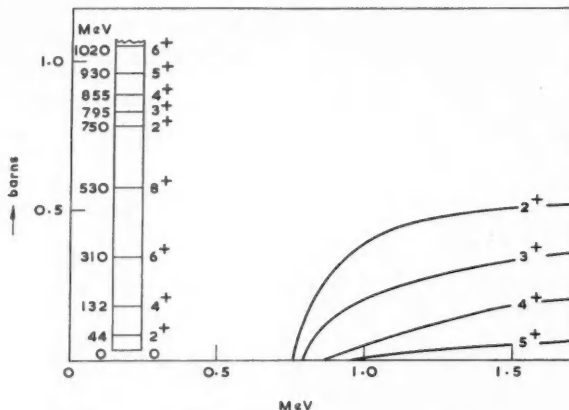


FIG. 5. Cross sections for inelastic scattering (for Th), calculated on the basis of Hauser and Feshbach's theory. Cross sections for the rotational band based on the ground state have been omitted.

scattered into the aperture and scattered again at its walls. An appreciable reduction in this scattering was obtained by lining the channel with graphite. For the monitor counters, the background counting rates then were about 10% of the total, but for the cylindrical counter it was about 30%. These backgrounds set a limit to the useful range of the present instrument; for neutrons with energies above some 3.7 Mev the screening of the counters became rapidly less effective and backgrounds became far too large.

#### 4. RESULTS

We have examined so far only a few elements with this method. The results are reported below. Since quite a large amount of the material to be examined is required, it is clear that, unless the apparatus is made very much more sensitive than it is at present, it is not possible to study separated isotopes.

##### (a) Fe

The peak due to the 845-kev state has already been mentioned. No other peak was found between the position in which this one occurs and that due to the 2.66-Mev level. However, an excited state at 2.085 Mev is well known in the decay of  $Mn^{56}$ , and has been reported by Mazari, Sperduto, and Buechner (1957), who studied the  $Co^{59}(p, \alpha) Fe^{56}$  reaction. If this state is  $4^+$ , as seems very likely (Poppema *et al.* 1955), it could only be very weakly excited by 255-kev neutrons and would not be detected with the present apparatus. The next three states, at 2.66, 2.96, and 3.13 Mev (to quote

Mazari *et al.*) were clearly detected and were used to measure the energies of the states of  $\text{Pb}^{208}$  (see Fig. 8 below). The peaks produced by these states are all of about equal height, which is to be expected if they all have (Poppema *et al.* 1955) spin  $2^+$ . The state at 3.34 Mev was not detected; for the neutrons required to produce this state (about 3.7 Mev) the screening of the counters was ineffective.

(b) *Ni and Zr*

The peaks produced in Ni and Zr (Fig. 6) were compared together in the manner described in Section 2. The energies of the peaks in the Zr curve

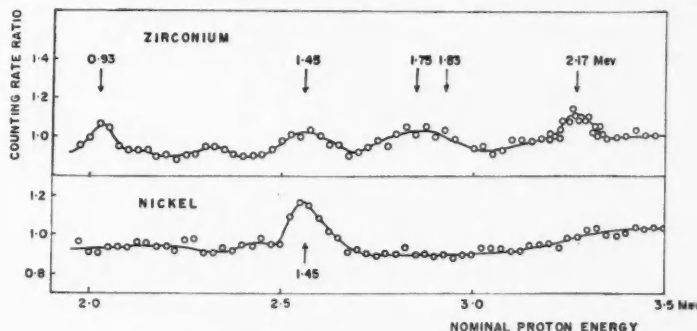


FIG. 6. Counting rate ratio for Zr and Ni, compared together. Neutron source:  $\text{H}^3(p, n)\text{He}^4$ .

were obtained by comparison with the peak produced in the Ni curve, the mid-point of which was assumed to correspond to the 1.45-Mev state (Nuclear Level Schemes 1957) of  $\text{Ni}^{68}$ . Three peaks stand out clearly in the Zr curve: one at 0.93 Mev, corresponding to the first-excited state of  $\text{Zr}^{92}$  (17% abundant), another at 1.45 Mev, and another at 2.19 Mev, corresponding to the first  $2^+$  state of  $\text{Zr}^{90}$  (51% abundant), described recently by Lazar and his associates (1958). A weak peak which might correspond to the 1.22 Mev first-excited state of  $\text{Zr}^{91}$  can be seen in Fig. 6. The peak corresponding to an excitation of 1.45 Mev does not correspond to any known state in the Zr isotopes. If it were due to  $\text{Zr}^{90}$ , its spin would be 0, 1, 2, or 3, and unless of odd parity, which would be unlikely theoretically, should have been observed in the decay of  $\text{Nb}^{90}$ . A weak peak corresponding to the 1.73-Mev  $0^+$  state of  $\text{Zr}^{90}$  can also be seen in Fig. 6; this peak seems to be broadened, probably by the excitation of the 1.83-Mev state of  $\text{Zr}^{92}$ , which has spin 2 or 3 and even parity (Nuclear Level Schemes 1957). Detail of the  $\text{Ni}^{68}$  peak at 1.45 Mev is shown in Fig. 7. A bump on the low-energy side is probably that caused by the 1.33-Mev state of  $\text{Ni}^{60}$ .

(c) *Pb isotopes*

Targets of similar shape of natural Pb and Fe were compared together (Fig. 8); also two targets of Pb were compared against each other (Fig. 9),

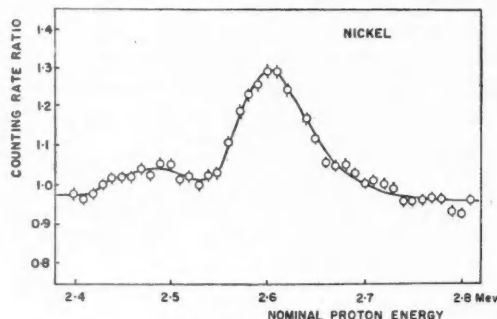


FIG. 7. Detail of Ni peak.

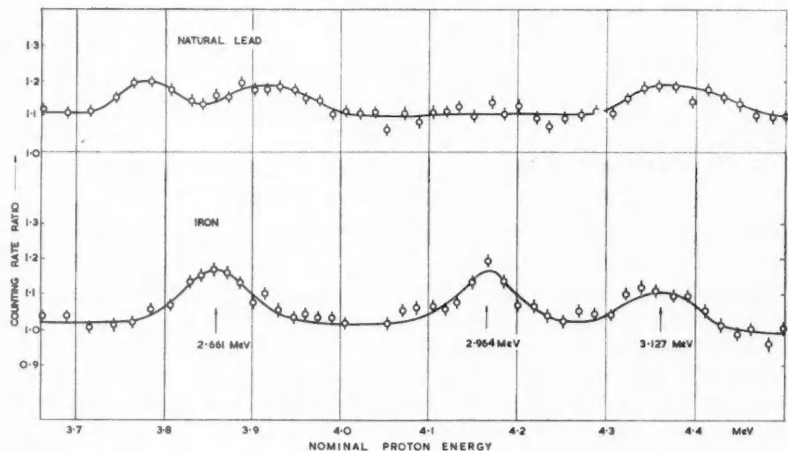
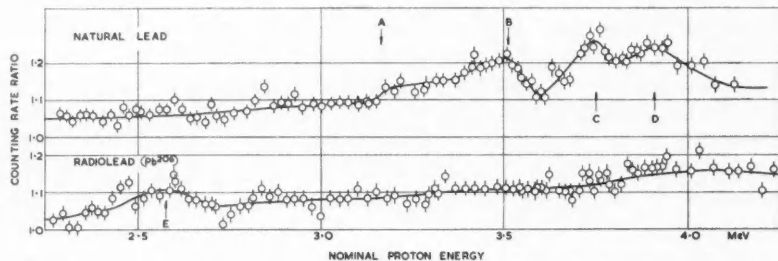


FIG. 8. Counting rate ratio for natural Pb and Fe, compared together.

FIG. 9. Counting rate ratio for natural Pb and radiolead,  $\text{Pb}^{206}$ , compared together.

one of natural Pb, and another containing\* 88% of  $Pb^{206}$ . Both Pb targets produced peaks due to the first-excited state of  $Pb^{206}$  at 803 kev. The height of this peak in the  $Pb^{206}$  target (1.25) was lower than one would expect from the result obtained (1.65) for the first-excited state of  $Fe^{56}$ . Another curious feature was the absence of peaks corresponding to higher states throughout the energy range studied in  $Pb^{206}$ , i.e., for neutrons with energies up to 3.5 Mev. Yet there must surely be many other states with spins in the right range which should be detectable by this method if there were free competition between the inelastically scattered neutrons emitted by the compound state. According to Kearsley (1957) and to True and Ford (1958) there should be at least five additional  $2^+$  states in this energy range. Day (1956) has found that the  $\gamma$ -rays produced by  $Pb^{206}$  excited by scattering of 2.56-Mev neutrons are consistent with the existence of states at 1.46 and 1.73 Mev. It is possible that a slight rise in the counting rate ratio (at E in Fig. 9) may be due to the first of these two states.

From natural Pb a weak peak was barely discernible in the position to be expected of the 0.57-Mev  $p_{5/2}$  state of  $Pb^{207}$  (not shown in Figs. 8 and 9). The peak due to the 0.90-Mev  $p_{1/2}$  state in this nucleus, which should be visible, was not observed. In fact, no further peaks could be found above that due to the 803-kev state in  $Pb^{206}$  until the proton energy was near 3.2 Mev. At this point (A in Fig. 9) the counting rate ratio rose by 10%, stayed at that level until the proton energy was 3.4 Mev, rose again (B in Fig. 9), and then fell to the normal value at 3.6 Mev. Beyond this point there was a low peak (C), which by comparison with the Fe states, was found to correspond to an energy of  $2.626 \pm 0.010$  Mev: it is clearly the well-known 2.62-Mev 3- state of  $Pb^{208}$ . This was followed by another weak peak, 200 kev higher, and finally, by another which appeared at the same proton energy as the 3.127-Mev peak (Mazari *et al.* 1957) of  $Fe^{56}$  (see Fig. 8). It should be noted that these peaks, which are reproducible, have no parallel in the  $Pb^{206}$  curve, which was obtained simultaneously. Therefore, they are not likely to be of instrumental origin; it follows that they must be caused by natural Pb.

The curve obtained with  $Pb^{206}$ , although showing no well-defined peaks, rose slowly by about 7% over a range of about 0.5 Mev centered on a neutron energy of about 3 Mev (corresponding to a proton energy of 4 Mev, see Fig. 9). The same phenomenon seems to occur in natural Pb; it is possible that it may be instrumental in origin for the carbon lining of the entrance channel has a broad resonance in this region.  $Pb^{206}$  is known to have a 3- level (Alburger 1954) at 2.53 Mev, which, to judge from Cohen's experiments (1957), is probably of the same nature as the 3- state at 2.62 Mev in  $Pb^{208}$ . There is no sign of a peak in the  $Pb^{206}$  curve corresponding to this state. This is possibly less surprising than seems at first sight, for if the lower states of  $Pb^{206}$  are excited rather weakly as would appear from the excitation of the 803-kev

\*The authors are indebted to Dr. G. A. Bartholomew of Atomic Energy of Canada, Ltd., for the loan of material for this target. We are indebted also to Mr. D. Dance of Harwell, for an isotopic analysis of this target; he found 88.3% of  $Pb^{206}$ , 8.8% of  $Pb^{207}$ , 2.0% of  $Pb^{208}$ , and 0.08% of  $Pb^{204}$ .

level, the competition from neutrons producing higher states (which are not observed) might reduce the peak to be expected at 2.53 Mev to unobservable proportions.

The peaks in natural Pb below that of the 2.62-Mev peak can only be caused by  $\text{Pb}^{208}$  or by  $\text{Pb}^{207}$ . Since the lower-lying states in the latter nucleus have very little effect on the curve obtained with natural Pb which contains only 22.6% of  $\text{Pb}^{207}$ , it seems rather more likely that they derive from  $\text{Pb}^{208}$ . No states lower than the 2.62-Mev state are known to exist. Cohen (1957) has reported a proton group in the  $(p, p')$  reaction at 23 Mev, corresponding to an excited state at 1.2 Mev. No such peak was found in the present measurements; however, it must be remembered that the low energy (255 kev) of the scattered neutrons in the present measurements puts a severe restriction on the spin of the state to be detected. If the present results are indeed to be interpreted as the excitation of states in  $\text{Pb}^{208}$ , the energy of the lowest is  $2.05 \pm 0.1$  Mev (near A, Fig. 9). This is followed by another 100 kev higher, and a rather more strongly excited level at  $2.37 \pm 0.1$  Mev (B in Fig. 9). As already pointed out, these states, if they exist, must have a spin not exceeding 3 units; if 0 or 1 (of either parity) it is very unlikely that they would have been excited in the decay of  $\text{ThC}''$  ( $\text{Ti}^{208}$ ).

Similar remarks apply to the two peaks above that of the 2.62-Mev state. The energies of the states corresponding to these peaks together with those of the Fe states, from which their energies have been measured, are shown in Table I.

TABLE I  
Energies of Pb states obtained by comparison with the states of  $\text{Fe}^{56}$

Pb states, Mev	$\text{Fe}^{56}$ states used in comparison <sup>(14)</sup> , Mev
$2.626 \pm 0.010$	2.661
$2.770 \pm 0.010$	2.661
$3.185 \pm 0.010$	3.127

The last of these Pb states, 3.185 Mev, has an energy close to the 5<sup>-</sup> state (at 3.198 Mev) excited (Elliott *et al.* 1956) in the decay of  $\text{Ti}^{208}$ . Since the probability of exciting a state with spin 5 is very small when the scattered neutrons are limited to an energy of 255 kev, it is clear that the two states are not identical (see Section 5).

#### (d) $\text{Th}$

The results obtained for  $\text{Th}^{232}$  are shown in Fig. 10. The lower peak is much wider than that to be expected of a single-excited state. The mid-point corresponds to an excitation of  $760 \pm 20$  kev. There is an indication of an excited state about 150 kev higher. The mid-point of the higher peak corresponds to an excitation energy of 1080 kev. It also seems to have associated with it a weak peak some 150 kev higher. No other peaks were found corre-

sponding to excitation energies below 1500 kev, the maximum attained (with Th) in these measurements. None were found below that corresponding to 760 kev with the exception of the 50-kev level already referred to (Fig. 3(a)).

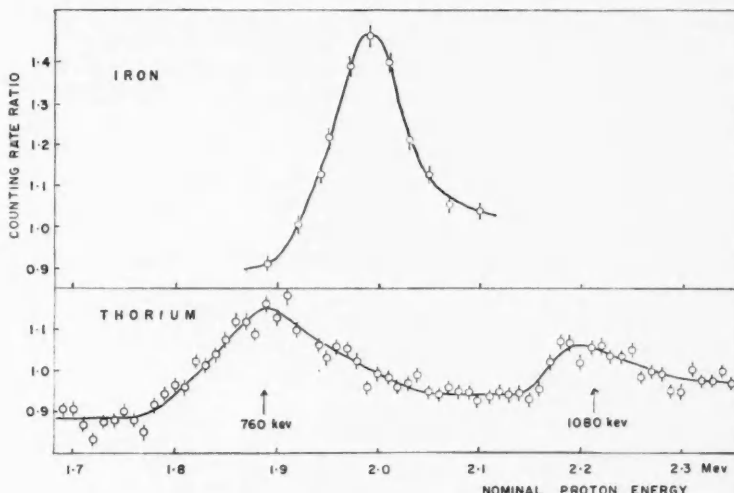


FIG. 10. Counting rate ratio for Th and Fe, compared together.

The energy corresponding to the mid-point of the lower peak (760 kev) is in agreement with the energy of the  $\gamma$ -ray found by Stelson and McGowan (1955) by Coulomb excitation. The shape of this peak, however, indicates that a state is excited both below and above this energy. Class (unpublished) has found internal conversion electrons produced by Coulomb excitation corresponding to a state with an energy of  $725 \pm 3$  kev. This figure is consistent with our result.

#### (e) $U$

The results obtained from  $U^{238}$  are shown in Fig. 11. The lower peak has a mid-point which corresponds to an energy of  $710 \pm 20$  kev. This peak, like that in  $Th^{232}$ , is clearly complex and more than one excited state contributes to it. (It should be noted that the shape is quite different from that for  $Th^{232}$ .) Another state is excited some 200 kev higher; at this point, which corresponds to an excitation energy of about  $940 \pm 20$  kev, the counting rate ratio rises with a step and, up to the maximum energy to which we have carried this investigation (1500 kev in excitation), does not return to its original value.

The positions of the states revealed in the present work agree roughly with those found by Cranberg and Levin (1958) by time-of-flight measurements. They found levels at  $730 \pm 20$  and  $980 \pm 20$  kev. Their resolution, however, was not sufficient to reveal structure of the kind shown in Fig. 11. They also found levels at  $1060 \pm 30$  kev, and another at 1260 kev. In our experiment

the former would not appear resolved from that at 980 kev, but the latter should be well separated. We did not find any such separation.

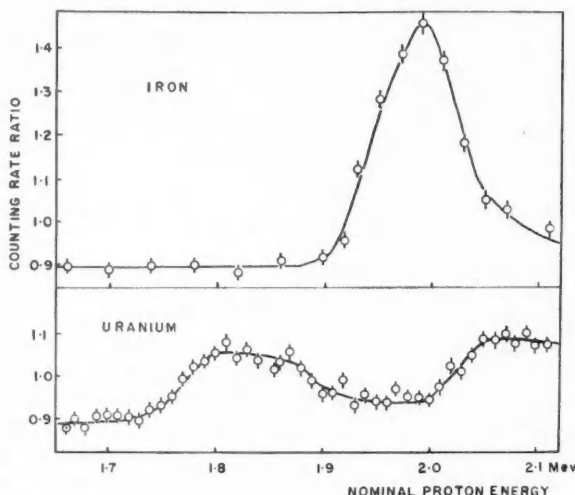


FIG. 11. Counting rate ratio for U and Fe, compared together.

That the counting rate ratio peaks we have found should show structure is to be expected if they represent vibrational states, because each intrinsic state will have a rotational band associated with it. If the head of the band has spin 0 or 2, two states should be visible in each.

##### 5. SEARCH FOR ELECTRIC MONOPOLE TRANSITIONS FROM $\text{Pb}^{208}$

The existence of one or more low-lying  $0^+$  states in  $\text{Pb}^{208}$  is to be expected by analogy with nuclei like  $\text{Ca}^{40}$  and  $\text{Zr}^{90}$ , because these nuclei, like  $\text{Pb}^{208}$ , have closed shells for both neutrons and protons. Electric monopole transitions leading to the ground states in the two latter nuclei have been detected through internal pair production. In  $\text{Zr}^{90}$  the internal photoelectric and pair conversion rates are nearly equal (Greenberg and Deutsch 1956). Provided that an electric monopole transition in  $\text{Pb}^{208}$  does not have to compete unfavorably with the emission of electric quadrupole radiation, one might expect a somewhat smaller, but comparable, yield of pairs. If any of the weak peaks found below that corresponding to 2.62 Mev were of the  $0^+$  type, pair production should be readily detectable. Above that energy, an electric monopole transition from a  $0^+$  state to the ground state should compete favorably with  $E2$  transitions with energies near 1 Mev.

Internal pairs emitted by a level near 3.2 Mev have been observed in the decay of  $\text{ThC}''$  ( $\text{Tl}^{208}$ ) by Alichanow and Dzellepov (1938) and reported by Latyshev (1947). The intensity of these pairs was said to be about 2% of

those produced by the 2.62-Mev level.  $\gamma$ -Rays with an energy of 3.2 Mev do not appear to have been detected. According to Martin and Richardson (1950) their intensity must be less than 0.1% of the 2.62-Mev  $\gamma$ -ray.

Because of the competition provided by the 0.58-Mev  $\gamma$ -ray, we should not expect a direct transition to the ground state from a  $5^-$  level at 3.2 Mev to be detected in the form of  $\gamma$ -rays, still less as internally converted pairs. The evidence just mentioned, therefore, is consistent only with an infrequent excitation of another level near 3.2 Mev, for which the pair internal conversion coefficient is at least 20 times greater than that of the 2.62-Mev transition. Such a conversion coefficient could correspond only to an electric monopole transition. It is possible, therefore, that the peak in the counting rate ratio found at 3.185 Mev corresponds to a  $0^+$  state.

An attempt was made, therefore, to detect annihilation radiation from pairs produced by electric monopole transitions excited by neutron scattering in Pb, using the apparatus shown in Fig. 12. Pairs produced in a conical bundle of flat sheets of Pb bombarded by neutrons were detected by two well-shielded

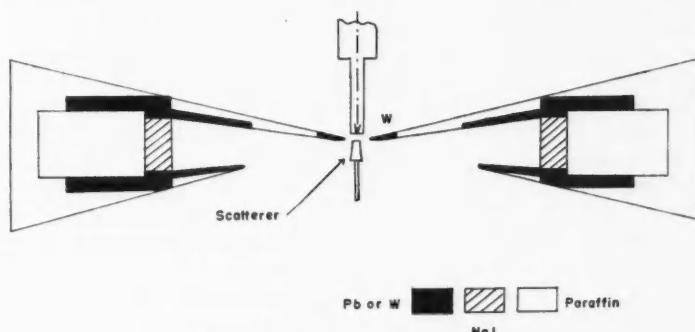


FIG. 12. Apparatus for detection of annihilation radiation.

4-in. diameter NaI crystals viewed by photomultipliers. The crystals were located 14 inches from the scatterer and on opposite sides of it. Fast coincidences between the two crystals (resolution time: 15  $\mu$ seconds) were fed into a slow threefold coincidence mixer (resolution time: 2  $\mu$ seconds), together with slow pulses taken from lower dynodes on the two multipliers. The latter pulses were fed into single-channel pulse height analyzers set to pass only pulses produced by annihilation radiation. The apparatus was adjusted for maximum sensitivity by replacing the scatterer with a source of  $\text{Na}^{22}$ .

The results obtained with natural Pb and with Zr are shown in Figs. 13 and 14 respectively. In each case, the neutron source was the  $\text{H}^3(p, n)\text{He}^3$  reaction. The Zr results show a threshold for protons at 2.6 Mev which corresponds to neutrons incident with an energy of 1.8 Mev. This is in agreement with the position of the  $0^+$  state in  $\text{Zr}^{90}$  (1.73 Mev) (Nuclear Level Schemes 1957); from this we conclude that the Zr results are probably genuine. The

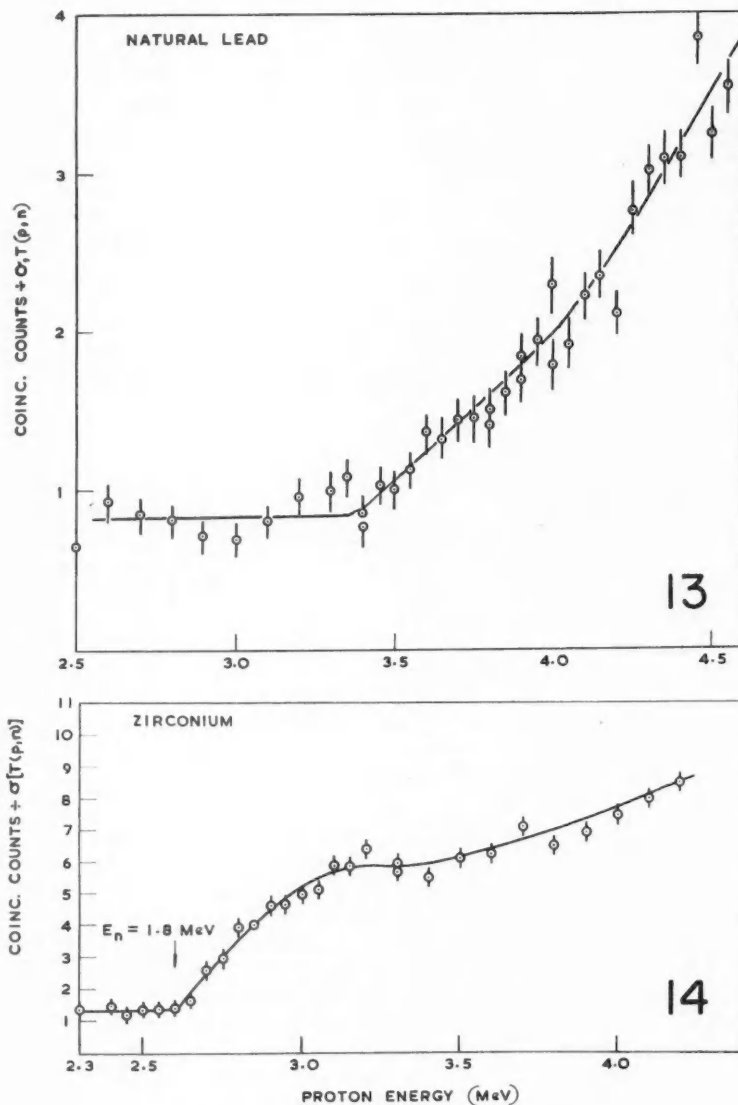


FIG. 13. Coincidence counting rate from Pb.  
 FIG. 14. Coincidence counting rate from Zr.

Pb curve shows a threshold at 3.4-Mev proton energy, corresponding to neutrons incident with 2.6 Mev. However, a very similar effect was found with radiogenic Pb(Pb<sup>206</sup>) and with carbon and bismuth. Nothing whatever is to be expected from carbon; we conclude, therefore, that these thresholds at 2.6 Mev are spurious.

Experiments were made with Zr and Pb to determine the yield of coincidences as a function of the thickness of the scatterer. For Zr, the proton energy in these measurements was 3.0 Mev, corresponding to neutrons of 2.2 Mev; for Pb, the proton energy was 4.0 Mev, corresponding to neutrons of 3.2 Mev. In each case, the coincidence counting rate was found to be proportional to  $xe^{-\mu x}$ , where  $x$  is the thickness and  $\mu$  is the appropriate attenuation coefficient for annihilation radiation in the material. This is the expected form of thickness variation if the coincidences observed were caused by annihilation radiation from internally converted pairs. However, a similar effect would be produced if coincidences were caused by neutrons scattered from the target, or if  $\gamma$ -rays produced outside the target were to be absorbed in it by the pair process. In the present apparatus, it is not clear how either of these two processes could cause the spurious effect observed. However, the spurious effect could not be produced by external production of pairs by  $\gamma$ -rays excited within the material by inelastic neutron scattering, for the yield of such pairs would depend on the thickness approximately as  $x^2 e^{-\mu x}$ . The results obtained showed clearly that the contribution made by the latter effect was less than 10% of the total for thicknesses of material of the order of  $\frac{1}{4}$  inch. The fact that the effect in Pb has a threshold at 2.6 Mev suggests that  $\gamma$ -rays excited in the Pb shields surrounding the crystals might be responsible. It is difficult to understand how this could occur, because the geometry of the apparatus ensures that sources of pairs producing coincidences must lie between the crystals and on a line which passes through both of them.

For 4-Mev protons, the coincidence counting rate from Pb is about one fifth of that produced by an equal volume of Zr at the same position. Above 4 Mev, the coincidence counting rate per unit proton charge corrected for the differential cross section for the neutron production in the forward direction increases linearly without a break. There is, therefore, no evidence that a  $0^+$  state is excited near 3.2 Mev. The spurious effect, however, might well mask a genuine effect with a threshold near this energy. Allowing for the fact that only half of natural Pb consists of Pb<sup>208</sup>, the yield for Pb at 4-Mev proton energy corresponds roughly to half the cross section for pair production in Zr. Thus a real effect of this magnitude might not be detected.

#### REFERENCES

ADAIR, R. K. 1950. Phys. Rev. **79**, 1018.  
 ALBURGER, D. E. and PRYCE, M. H. L. 1954. Phys. Rev. **95**, 1482.  
 ALICHANOV, A. J. and DZELEPOV, D. P. 1938. Compt. rend. acad. sci. U.S.S.R. **20**, 133.  
 BONNER, T. W. and COOK, C. F. 1954. Phys. Rev. **96**, 122.  
 COHEN, B. L. 1957. Phys. Rev. **106**, 995.  
 CLASS, C. M. Unpublished.  
 CRANBERG, L. and LEVIN, J. S. 1958. Phys. Rev. **109**, 2063.  
 DAY, R. B. 1956. Phys. Rev. **102**, 767.  
 ELLIOTT, L. G., GRAHAM, R. L., and WOLFSON, J. L. 1956. Phys. Rev. **93**, 356.

GREENBERG, J. S. and DEUTSCH, M. 1956. *Phys. Rev.* **102**, 415.  
HAUSER, W. and FESHBACH, H. 1952. *Phys. Rev.* **87**, 366.  
KEARSLEY, M. J. 1957. *Nuclear Phys.* **4**, 157.  
LATYSHEV, G. 1947. *Revs. Modern Phys.* **19**, 132.  
LAZAR, N. H., O'KELLEY, G. D., HAMILTON, J. H., LANGER, L. M., and SMITH, W. G. 1958. *Phys. Rev.* **110**, 513.  
MARTIN, D. G. E. and RICHARDSON, H. O. W. 1950. *Proc. Phys. Soc. (London)*, A, **63**, 223.  
MAZARI, M., SPERDUTO, A., and BUECHNER, W. W. 1957. *Phys. Rev.* **107**, 356.  
NUCLEAR LEVEL SCHEMES, A = 40-A = 92. 1957. U.S. Atomic Energy Commission, TID-5300.  
POPPEMA, O. J., SIEKMAN, J. G., and VAN WAGENINGEN, R. 1955. *Physica*, **21**, 223.  
STELSON, P. H. and McGOWAN, F. K. 1955. *Phys. Rev.* **99**, 112.  
STELSON, P. H. and PRESTON, W. M. 1951a. *Phys. Rev.* **83**, 469.  
1951b. *Phys. Rev.* **84**, 162.  
TRUE, W. W. and FORD, K. W. 1958. *Phys. Rev.* **109**, 1675.

## WATER VAPOR PERMEABILITY OF POROUS MEDIA<sup>1</sup>

WILLIAM WOODSIDE

### ABSTRACT

Following the analogy between the laws of heat conduction and vapor diffusion, two theoretical expressions for the thermal conductivity of a composite medium are applied to the water vapor permeability coefficient of certain porous media. It is shown that both expressions reduce to a form very similar to the empirical relationships found by Penman and Edenholm for soils, glass spheres, charcoal, and cellular concrete. The calculation of the variation of water vapor permeability with density for a cellular lightweight concrete is illustrated.

A granular material is made up of one or more types of particles surrounded by a homogeneous medium (usually air). All granular materials have associated with them values of thermal conductivity, electrical conductivity, dielectric constant, magnetic permeability, and other diffusion-type coefficients. In many instances, it would be advantageous to be able to calculate the values of such coefficients from the corresponding values for the various constituents and the volume fractions of the constituents.

Since the mathematical theories of steady-state thermal and electrical conduction, electric and magnetic fields, and diffusion are all similar, a formula derived for the thermal conductivity of a granular material will also be applicable to the calculation of electrical conductivity, dielectric constant, magnetic permeability, and diffusion coefficient (de Vries 1952). Two of these coefficients are of main interest here, namely thermal conductivity and water vapor diffusion coefficient. Several equations have already been applied by the author to the calculation of the thermal conductivity of porous media (Woodside 1958). It is the object of this note to describe the application of similar equations to the calculation of the water vapor diffusion coefficient or water vapor permeability of certain porous media.

The following equation of de Vries (1952) was derived by Maxwell for electrical conductivity and applied by Eucken to the calculation of thermal conductivity.

$$(1) \quad \frac{k}{k_g} = \frac{1+2(1-P) [(1-k_g/k_s)/(1+2k_g/k_s)]}{1-(1-P) [(1-k_g/k_s)/(1+2k_g/k_s)]},$$

where  $P$  is the fractional porosity of the porous medium, and  $k$ ,  $k_g$ , and  $k_s$  are the thermal conductivities of the porous medium, the gas phase (air), and solid respectively. This equation applies to a granular porous material, that is, one in which discrete solid particles are distributed in a continuous gas phase. For a cellular porous material, one in which discrete gas cells are distributed in a continuous solid phase, the equation must be modified by interchanging  $k_g$  and  $k_s$  and by replacing  $P$  by  $(1-P)$ .

<sup>1</sup>Manuscript received November 24, 1958.

Contribution from the Building Services Section, Division of Building Research, National Research Council, Ottawa, Canada.

Issued as N.R.C. No. 5071.

For application of equation (1) to calculation of vapor permeability of porous media, the thermal conductivities  $k$ ,  $k_g$ , and  $k_s$  must be replaced by the corresponding vapor permeabilities  $\mu$ ,  $\mu_g$ , and  $\mu_s$ . Thus the equation for the vapor permeability  $\mu$  of a granular material reads

$$(2) \quad \frac{\mu}{\mu_g} = \frac{1+2(1-P) [(1-\mu_g/\mu_s)/(1+2\mu_g/\mu_s)]}{1-(1-P) [(1-\mu_g/\mu_s)/(1+2\mu_g/\mu_s)]},$$

where  $P$  is again the porosity, and  $\mu_g$  and  $\mu_s$  are the vapor permeabilities of the gas (air) and solid respectively.

For most granular materials, the solid particles are impervious to water vapor, and therefore  $\mu_s = 0$ . Also since air is the gas phase in most granular materials,  $\mu_g = \mu_{\text{air}}$ . Therefore,

$$\frac{1-\mu_g/\mu_s}{1+2\mu_g/\mu_s} = \frac{\mu_s - \mu_g}{\mu_s + 2\mu_g} = -\frac{1}{2}$$

and equation (2) reads

$$(3) \quad \mu = \frac{2P}{3-P} \mu_{\text{air}}.$$

Maxwell's equation (de Vries 1952) was derived for a random distribution of spherical inclusions. Russell (1935) has derived a thermal conductivity equation for a cubic lattice of cubic inclusions. Russell's equation for a granular material is

$$(4) \quad \frac{k}{k_g} = \frac{(1-P)^{2/3} k_s/k_g + 1 - (1-P)^{2/3}}{[(1-P)^{2/3} - 1 + P] k_s/k_g + 2 - (1-P)^{2/3} - P}.$$

Again, replacing  $k$ ,  $k_g$ , and  $k_s$  by the corresponding vapor permeabilities,  $\mu$ ,  $\mu_g$ , and  $\mu_s$ , and also placing  $\mu_s = 0$  and  $\mu_g = \mu_{\text{air}}$ , this becomes

$$\mu/\mu_{\text{air}} = \frac{1 - (1-P)^{2/3}}{2 - (1-P)^{2/3} - P}.$$

By expanding the terms in brackets, this reduces to

$$\mu/\mu_{\text{air}} = \frac{\frac{2}{3}P + \frac{1}{9}P^2 + \frac{4}{81}P^3 + \dots}{1 - \frac{1}{3}P + \frac{1}{9}P^2 + \frac{4}{81}P^3 + \dots}.$$

For small values of the porosity  $P$ , the terms of order two and higher may be neglected, and the equation is

$$\mu/\mu_{\text{air}} = 2P/(3-P).$$

This is identical with equation (3), which was derived from Maxwell's equation.

This simple relationship between the vapor permeability of a granular material and its porosity is very similar to the relationship found experimentally by Penman (1940):

$$(5) \quad \mu = 0.66P\mu_{\text{air}}.$$

Penman observed that the diffusion of several different gases through both

dry and moist soils and other granular materials satisfied this relationship. In the case of moist soils,  $P$  represents the air-filled porosity, that is, the total porosity less the volumetric water content.

The dry-cup method for water vapor permeability determination involves a gravimetric measurement of the steady-state water vapor transmission through a plate of the test material under isothermal conditions (73° F) with a relative humidity of 0% maintained on one side (by means of a desiccant) and a relative humidity of 50% maintained on the other. For most porous media the equilibrium moisture content corresponding to a mean relative humidity of 25% is so low that moisture transmission by mechanisms other than vapor diffusion is relatively small. At higher mean relative humidities, the apparent vapor permeability may be several times larger than the dry-cup value, owing to other mechanisms of moisture transfer such as capillarity. The true vapor permeability must decrease at increasing mean relative humidities because of the decrease in air-filled pore space available for diffusion. Since vapor permeabilities determined by the dry-cup method correspond most closely to true vapor diffusion, only dry-cup values will be compared with calculated vapor permeabilities.

Edenholm (1945) observed experimentally that the 'dry-cup' water vapor permeability  $\mu$  is given by

$$(6) \quad \mu = k_r \times P \times \mu_{air},$$

where  $k_r$  is a constant for any given material (named reduction factor by Edenholm) and  $P$  is the coarse-capillary porosity of the material. Edenholm found a value of 0.65 for  $k_r$  for materials such as sand, glass spheres, charcoal, and a cellular concrete. The value of  $\mu_{air}$ , the water vapor permeability of air, at room temperature is 120 perm. in., the perm. in. being the presently accepted unit for vapor permeability, which is grains in./hr ft<sup>2</sup> (in. Hg). In Edenholm's units,  $\mu_{air} = 0.069$  kg/m atm hr.

The analysis given above results in a porosity-dependent reduction factor, since from equation (3)

$$k_r = 2/(3-P),$$

whereas both Penman and Edenholm found  $k_r$  to be constant. However, the reasonable agreement between the theoretical and measured values of vapor permeability is illustrated by the following calculation. Edenholm measured vapor permeabilities ranging between 0.018 and 0.022 kg/m atm hr for a bed of glass spheres of porosity 0.395. Substituting  $P = 0.395$  and  $\mu_{air} = 0.069$  into equation (3), gives a value for  $\mu = 0.0209$  kg/m atm hr, which is between the two measured values.

A further application of the theory to the calculation of the variation of vapor permeability with density for a cellular concrete is now described. Since a cellular material is essentially a continuous solid with distributed air cells, the equation to be used is the converse of equation (2):

$$(7) \quad \frac{\mu}{\mu_s} = \frac{1+2P[(1-\mu_s/\mu_g)/(1+2\mu_s/\mu_g)]}{1-P[(1-\mu_s/\mu_g)/(1+2\mu_s/\mu_g)]}.$$

Hallen (6) reports a value of 5.6 perm. in. at a density of 80 lb/ft<sup>3</sup> for the particular cellular concrete being considered. It is assumed that at this high density there are no 'large' air cells in the material (Edenholm's coarse capillary porosity equal to zero). Thus  $\mu_s = 5.6$ . The vapor permeability of the cellular concrete at 32 lb/ft<sup>3</sup> density will now be calculated. At this density the 'coarse' porosity,  $P$ , is

$$P = 1 - (32/80) = 0.60.$$

Taking  $\mu_{air} = 120$  perm. in. as the value for  $\mu_g$ , equation (7) results in a value for  $\mu$  of 24.0 perm. in. This compares favorably with laboratory 'dry-cup' test results for material of density 32 lb/ft<sup>3</sup> which show a value of 22.3 perm. in.

The application of a thermal conductivity equation for porous media to the calculation of water vapor permeability of certain porous materials seems warranted by the agreement with the empirical equations of Penman and Edenholm and by the agreement of predicted and experimental values.

It would appear that, because of the analogy between Darcy's law for fluid flow in porous media and the heat conduction equation, the same technique as described above could be applied to the calculation of the saturated permeability (of porous media) for liquid water. The difficulty in this application would appear to be the assignment of a value for  $k_g$  ( $k_s$  in most cases would be zero), since the value of  $k_g$  must obviously depend upon the mean pore size and hence upon the pore size distribution.

This is a contribution from the Division of Building Research, National Research Council of Canada, and is published with the approval of the Director of the Division.

#### REFERENCES

EDENHOLM, H. 1945. *Medd. Statens Forskningskommitte Lantmannabyggnader*, **5**, 53.  
HALLEN, W. 1957. Private communication, December 11.  
PENMAN, H. L. 1940. *J. Agr. Sci.* **30**, 438, 570.  
RUSSELL, H. W. 1935. *J. Am. Ceram. Soc.* **18**, 1.  
DE VRIES, D. A. 1952. *Mededel. Landbouwhogeschool Wageningen*, **52**, 1.  
WOODSIDE, W. 1958. *Can. J. Phys.* **36**, 815.

# THE THERMAL EXPANSION OF CUBIC BARIUM TITANATE (BaTiO<sub>3</sub>) FROM 350° C TO 1050° C<sup>1</sup>

J. A. BLAND<sup>2</sup>

## ABSTRACT

The lattice spacing of cubic barium titanate (BaTiO<sub>3</sub>) has been measured as a function of temperature by means of a Unicam X-ray camera. The relation between  $a_0$  (in Å) and  $t$  between 350° C and 1050° C is:

$$a_0 = 4.0062 + 3.00 \times 10^{-5} t + 1.95 \times 10^{-8} t^2.$$

The maximum systematic error in  $a_0$  is 0.0005 Å. The linear expansion coefficient varies in an approximately linear fashion between  $10.8 \times 10^{-6}$  per °C at 350° C to  $17.5 \times 10^{-6}$  per °C at 1050° C.

## 1. INTRODUCTION

The thermal expansion of barium titanate has been measured by Megaw (1947) between 20° C and 200° C using the X-ray powder technique, by Kay and Voussen (1949) and Rhodes (1951) between -160° C and 120° C using single crystal methods. These measurements were restricted to the temperature range -160° C to 200° C because several ferroelectric phase changes occur in this region. The present paper describes results obtained with a powder camera in the range 350° C to 1050° C throughout which barium titanate remains cubic.

## 2. APPARATUS AND SPECIMENS

The high temperature camera is of the type supplied by Unicam Limited. It has a spherical furnace wound with platinum wire and can be evacuated to a pressure of  $10^{-6}$  mm of mercury. Some modifications were made to the vacuum seals on the moving parts, the rotating specimen holder, and the sliding pillar which supports the thermocouple. The bead thermocouple was replaced by a thin platinum vs. platinum-rhodium thermocouple of the ring type described by Hume-Rothery and Reynolds (1938) which was then calibrated at 470° C by measuring the unit cell of pure silver and comparing it with the published value. Calibrations were also made at 660° C and 960° C, the melting points of aluminum and silver respectively, and these were observed through a lucite window placed in the X-ray port. The temperature distribution over the specimen was measured at five different temperatures between 400° C and 1000° C and found to be uniform to within  $\pm 5$ ° C. The furnace current was kept steady by means of hand regulation and it is believed that with the exception of the exposure in the region of 380° C, the recorded temperatures were accurate to within  $\pm 10$ ° C. No correction for

<sup>1</sup>Manuscript received October 24, 1958.

Contribution from the Mines Branch, Department of Mines and Technical Surveys, Ottawa, Canada. Published by permission of the Director, Mines Branch, Department of Mines and Technical Surveys, Ottawa, Canada.

<sup>2</sup>Physical Metallurgy Division, Mines Branch, Department of Mines and Technical Surveys, Ottawa, Canada.

emissivity of the kind suggested by Berry, Henry, and Raynor (1951) was made in the present work.

The powdered  $\text{BaTiO}_3$  used for preparing the specimens was stated to be 99.04% pure, the major impurities being 0.10% of  $\text{CaO}$ , 0.10% of  $\text{SrO}$ , 0.01% of  $\text{Fe}_2\text{O}_3$ , and 0.01% of  $\text{MgO}$ ; it was supplied by the National Lead Co., Niagara Falls, New York. After packing in a thin quartz capillary, the powder was heated, and sealed under a vacuum of  $10^{-4}$  mm of mercury. The specimen was then aligned on a specially built jig and cemented on a ceramic pillar, which was transferred to the camera and carefully centered.

### 3. FILM MEASUREMENTS

The photographic film was mounted in two sections in the cassette and the positions of the powder lines were measured with respect to the shadows of two knife-edges on each film using a travelling microscope. These positions were consistent to within 0.03 mm for the high  $\theta$ -angle reflections. The constants of the camera, determined by direct measurement are:

Diameter of the cassette	$19.010 \pm 0.004$ cm
Angle between back knife-edges	$19.964 \pm 0.005^\circ$
Angle between front knife-edges	$19.940 \pm 0.005^\circ$
Angles between knife-edges on each side are both equal to	$160.05 \pm 0.02^\circ$

The lattice parameter was computed from high angle reflections ( $\theta > 65^\circ$ ) obtained with copper radiation. At each temperature a good straight line extrapolation to  $\theta = 90^\circ$  was obtained when the apparent parameter was plotted against the function of  $\theta$  given by Nelson and Riley (1945). The 511 reflection was particularly favorable for extrapolation because its  $\theta$  value was greater than  $80^\circ$  for all temperatures. When all the systematic errors are taken into account, it is estimated that the final parameter is accurate to  $\pm 0.0005$  Å.

### 4. TEMPERATURE VARIATION OF LATTICE PARAMETER

The experimental values of  $a_0$  are given in Table I, and indicated by crosses

TABLE I  
Variation of the lattice parameter of cubic barium titanate ( $\text{BaTiO}_3$ )

Temp., °C	$a_0$ obs., Å	$a_0$ calc., Å	Diff.
380	4.0222	4.0204	-0.0018
485	4.0258	4.0254	-0.0004
674	4.0360	4.0353	-0.0007
965	4.0528	4.0533	+0.0005
1055	4.0599	4.0596	-0.0003

on Fig. 1. A parabolic curve, described by equation (i) and shown by the full line in Fig. 1, was found by trial and error to fit the observations satisfactorily:

$$(i) \quad a_0 = 4.0062 + 3.00 \times 10^{-5} t + 1.95 \times 10^{-8} t^2.$$

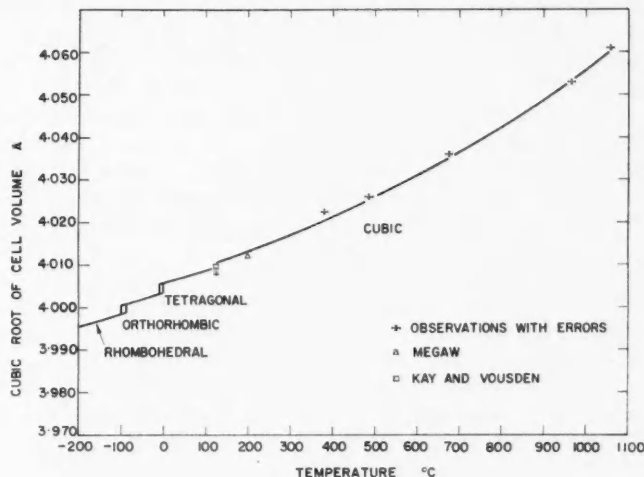


FIG. 1.

The observation at  $380^{\circ}\text{C}$  was given less weight in making this fit, because of the difficulty of controlling the temperature of the furnace accurately by hand below  $400^{\circ}\text{C}$ . Values of  $a_0$  calculated from the equation at the temperatures of the experiment are shown in Table I for comparison with the observed values. The differences are considered to be within the limits of experimental error.

Results obtained by other workers are also shown in Fig. 1. The spacing calculated from equation (i) at  $120^{\circ}\text{C}$ , below which barium titanate becomes ferroelectric, is  $4.0101\text{ \AA}$ , which should be compared with  $4.008\text{ \AA}$  obtained by Megaw (1947) and  $4.010\text{ \AA}$  obtained by Kay and Voussen (1949). The spacing at  $200^{\circ}\text{C}$  is calculated to be  $4.0130\text{ \AA}$  which is in fair agreement with  $4.0120\text{ \AA}$  obtained by Megaw (1947). For completeness the observations of Kay and Voussen (1949) in the region  $-150^{\circ}\text{C}$  to  $+120^{\circ}\text{C}$  are included in Fig. 1. In this range the cube root of the unit cell volume is represented.

The expansion coefficient, obtained directly from equation (i), is given by

$$(ii) \quad \alpha = (1/a_0) \times (\partial a_0 / \partial t)$$

where

$$(iii) \quad \partial a_0 / \partial t = 0.0030 \times 10^{-2} + 0.000390 \times 10^{-4} \times t.$$

The results are recorded in Table II and plotted in Fig. 2; it is estimated that the error is about 5%.

### 5. DISCUSSION

The volume expansion coefficients of the three low temperature phases of barium titanate were obtained by Rhodes (1951) and the corresponding mean values of the linear expansion coefficient are given in Table III together with

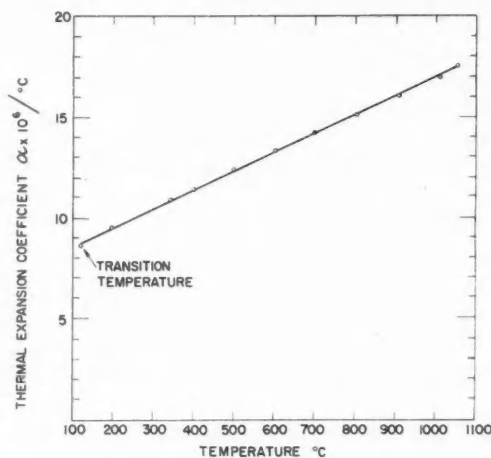


FIG. 2.

TABLE II  
Thermal expansion coefficient of cubic barium titanate ( $\text{BaTiO}_3$ )

Temp., °C	$a_0$ calc.	$(\partial a_0 / \partial t) 10^6$	$\alpha \times 10^6$ per °C
120	4.0101	34.7	8.6
200	4.0130	37.8	9.4
350	4.0191	43.4	10.8
400	4.0213	45.6	11.3
500	4.0261	49.5	12.3
600	4.0312	53.4	13.2
700	4.0367	57.3	14.2
800	4.0427	61.2	15.1
900	4.0490	65.1	16.1
1000	4.0557	69.0	17.0
1050	4.0596	71.0	17.5

TABLE III

Compound	Temp. range, °C	Linear exp. coeff. $\times 10^{10}$ per °C	Reference
$\text{BaTiO}_3$	Tetragonal, +20 to +4	11.4	Rhodes (1951)
	Orthorhombic, +4 to -99	11.4	Rhodes (1951)
	Rhombohedral, -99 to -160	8.8	Rhodes (1951)
	Cubic, +200 to +120	$10 \pm 3$	Megaw (1947)
	Tetragonal, +120 to +20	$3.5 \pm 1.5$	Megaw (1947)
$\text{PbZrO}_3$	Cubic, above +230	11.0	Shirane and Hoshino (1954)
			Shirane, Hoshino, and Suzuki (1950)
$\text{PbTiO}_3$	Cubic, above +490	8.3	

results obtained by Megaw (1947) for the tetragonal and cubic forms. The value of the coefficient given by Rhodes for the tetragonal form is larger than that obtained by Megaw, but the latter determination is probably more reliable because extrapolation methods were used to obtain the lattice parameter from powder data. Comparing Tables II and III it can be seen that for the cubic region, the value of the linear expansion coefficient deduced from the present work is within the range suggested by Megaw. If Megaw's value for the tetragonal range is accepted it would indicate that there is a large increase in the expansion coefficient of barium titanate as it changes from the tetragonal to the cubic form.

The linear expansion coefficient of cubic barium titanate may be compared with observations of the thermal expansion of other cubic perovskite structures at higher temperatures. Data have been published for lead zirconate (Shirane and Hoshino 1954) and lead titanate (Shirane, Hoshino, and Suzuki 1950) which, like barium titanate, are tetragonal at room temperature and become cubic at higher temperatures. The linear expansion coefficients of these substances above their respective transition points are given in Table III. It appears that the expansion coefficient of lead zirconate above 230° C is of the same order as that of barium titanate in this region while that of lead titanate above 490° C is significantly lower than the corresponding value for barium titanate.

#### ACKNOWLEDGMENTS

My thanks are due to Dr. C. M. Mitchell for his interest and encouragement; I am grateful to Dr. Z. S. Bazinski of the National Research Council of Canada for useful suggestions and for fitting the ring thermocouple. I am indebted to Mr. B. C. Hansen for modifying and operating the apparatus and to Mr. Bernard Renaud for his help with the specimen preparation.

#### REFERENCES

BERRY, R. L., HENRY, W. G., and RAYNOR, G. V. 1951. *J. Inst. Metals*, **78**, 643.  
HUME-ROTHERY, W. and REYNOLDS, P. W. 1938. *Proc. Roy. Soc. (London)*, A, **167**, 25.  
KAY, H. F. and VOUSDEN, P. 1949. *Phil. Mag.* **40**, 1019.  
MEGAW, H. D. 1947. *Proc. Roy. Soc. (London)*, A, **189**, 261.  
NELSON, J. B. and RILEY, D. P. 1945. *Proc. Phys. Soc. (London)*, **57**, 160.  
RHODES, R. G. 1951. *Acta Cryst.* **4**, 105.  
SHIRANE, G. and HOSHINO, S. 1954. *Acta Cryst.* **7**, 203.  
SHIRANE, G., HOSHINO, S., and SUZUKI, K. 1950. *Phys. Rev.* **80**, 1105.  
WILSON, A. J. C. 1941. *Proc. Phys. Soc. (London)*, **53**, 235.

# INTERCOMPARISON OF 11 RESISTANCE THERMOMETERS AT THE ICE, STEAM, TIN, CADMIUM, AND ZINC POINTS<sup>1</sup>

E. H. McLAREN

## ABSTRACT

Eleven standard platinum resistance thermometers, including thermometers having three different types of construction, have been intercompared at the triple point of water, boiling point of water, and the liquidus points of high purity tin, cadmium, and zinc. Temperature coefficients determined from measurements at the triple and boiling points of water and the zinc point were used to calibrate the thermometers for the temperature calculations on measurements at the tin and cadmium points. The results show that, although the measurements were made at a precision of about 0.0002°C at each fixed point, distinctive deviations from quadratic resistance-temperature relations were not found for the 11 thermometers. This verification of the quadratic form for the resistance-temperature relationship realized with these thermometers gives strong support for the use of the liquidus point of high purity indium, tin, or cadmium as a precision alternative to the steam point on the International Temperature Scale.

## INTRODUCTION

The establishment of a series of five precision fixed temperature points (triple and boiling points of water and the liquidus points of high purity samples of Sn, Cd, and Zn\*) has provided a means of detecting differences in temperatures determined by means of 11 standard thermometers that arise from other than random deviations from quadratics in their resistance-temperature relations. This is done by calibrating the thermometers from measurements at any three of these fixed points and then determining the temperatures at the other two points. For this paper results are reported for temperature calculations on measurements at the Sn and Cd points determined with temperature coefficients based on measurements at the triple and boiling points of water and the zinc point.

## EXPERIMENTAL

### *Resistance Thermometers*

The 11 thermometers included 9 made by C. H. Meyers† (1943 design), 1 modified‡ Barber-type, E.1, made by Tinsley (England), and 1 of earlier Meyers' design§ (1932), A.1, constructed by Leeds and Northrup Co. (United States). Eight of the thermometers that were made by Mr. Meyers had pyrex sheaths and  $R_0$  values of 25.5 ohms while the ninth thermometer, S261, was constructed with a fused silica sheath and an  $R_0$  value of 12.78 ohms.

<sup>1</sup>Manuscript received December 24, 1958.

Contribution from the Division of Applied Physics, National Research Council, Ottawa, Canada.

Issued as N.R.C. No. 5096.

\*Details on these fixed points are given by Berry (1958) and McLaren (1957a, b; 1958a, b).

†C. H. Meyers, 6316 Brookside Dr., Alexandria, Va., U.S.A.; a description of these thermometers is given by Stimson (1955).

‡0.2-mm diameter gold leads in place of the conventional 0.5-mm diameter; Barber (1950, 1955) and Hall (1955) describe the construction and characteristics of similar thermometers.

§See Meyers (1932).

Before using thermometers A.1 and E.1 it was necessary to investigate their immersion-temperature relations: a Meyers' thermometer, S155, was included in this study for comparative purposes. For these investigations the pure metal melts were used with atmospheric air pressure. Figures 1 and 2 show how the resistances at the liquidus points of Sn and Zn varied with immersion depths for the three thermometers (100 micro-ohms  $\cong 0.001^\circ\text{C}$ ). Each plotted point is the average of a measuring sequence of NNRRRRNN\* at 1 ma current: a scaling uncertainty of about 1 cm may exist in the abscissa of these plots. The solid lines in the figures represent the theoretical variations in freezing temperatures with hydrostatic pressure that were deduced from the Clausius-Clapeyron relation using the information given in Table II. Table I summarizes some of the physical specifications of these thermometers

TABLE I

Thermometer	$R_0$ , ohms	Pyrex sheath diam., mm	Gold leads diam., mm	Working length, $\dagger$ cm	Required mid-point immersion	
					Sn, cm	Zn, cm
S155	25.48	7.4	0.2	44	12	14
E.1*	24.98	8.	0.2	44	21	26
A.1	25.52	7.	0.32	44	23	>29

\*E.1—Johnson, Matthey & Co., platinum; S155, A.1—Sigmund Cohn Corp., platinum.

$\dagger$ Working length of a thermometer means the length of the stem from the mid-point of the sensing coil to the base of the head.

and gives the minimum mid-point immersions that are required for precision work when they are used in the experimental arrangement favored by this laboratory.

#### Intercomparisons

Prior to the intercomparisons all thermometers were annealed at about  $450^\circ\text{C}$  to stabilize the resistivities and temperature coefficients of resistivity of the platinum. During the work at the metal freezing points thermometers A.1 and E.1 were used at mid-point immersions of about 30 and 27 cm respectively, and the Meyers' thermometers were used at immersions of 15 cm. For this part of the investigation dry nitrogen atmospheres were used over the melts and the temperatures are corrected to correspond to liquidus points under a total pressure of 1 atmosphere. Table II gives the densities

TABLE II

Metal	$\Delta T$ for 1 atm, $^\circ\text{C}$	Liquid density at liquidus pt., g/cc	Immersion press. correction $\Delta T/\text{cm. } ^\circ\text{C}$
Zn	+0.0043	6.55	-0.0000274
Cd	+0.0062	8.02	-0.0000483
Sn	+0.0033	7.00	-0.0000224
In	+0.0049	7.03	-0.0000334

\*N and R refer to resistance balances with the thermometer connected in the Normal and Reversed positions respectively on the Mueller Wheatstone Bridge.

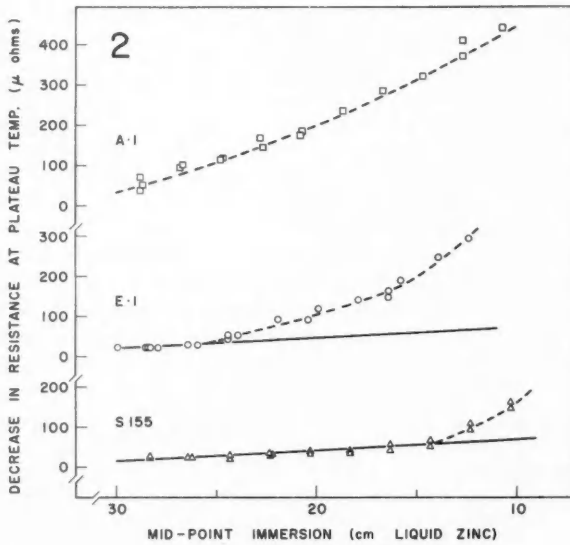
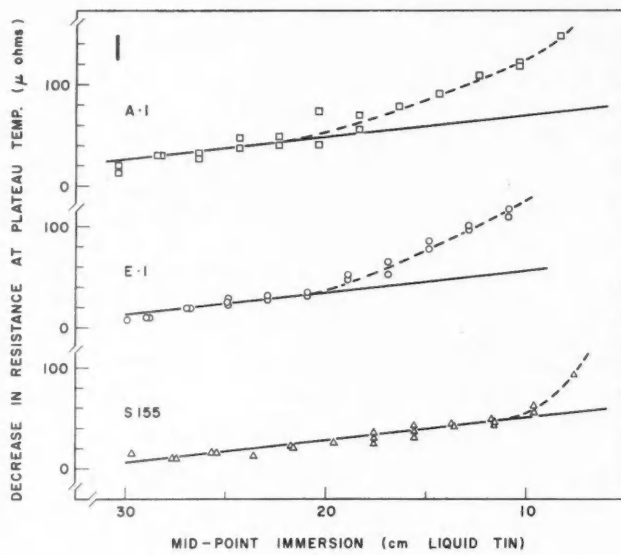


FIG. 1. Immersion-temperature effects for the three types of thermometers at the tin point (100 micro-ohms  $\cong 0.001^\circ \text{C}$ ).

FIG. 2. Immersion-temperature effects at the zinc point (100 micro-ohms  $\cong 0.001^\circ \text{C}$ ).

and the pressure-temperature dependencies that are used for these corrections in this laboratory: values for indium are also included.

Two freezes were made with each thermometer in Zn, Cd, and Sn, in that order, and measurements at the steam point\* completed the series. The liquidus point determinations were made on New Jersey Super Pure (99.999+%) Zinc and Cadmium and Vulcan Detinning Extra Pure (99.99+%) Tin. There is now a large amount of evidence to show that the liquidus points of this zinc and cadmium must be less than 0.001°C from that of the pure elements having natural isotopic contents. The tin point is not yet in this satisfactory state and more work is required on 99.999+% tin before it will be certain that samples are available that have liquidus points within 0.001°C of that of the pure natural element.†

Early measurements (1956) on the nine Meyers thermometers extended over a period of about 3 months while measurements on thermometers E.1, A.1, S156, and S155 were carried out at a later period (1958) during a 3-week interval. Measurements at the triple point of water (triple cell 29) were made before and after each measurement at the other test points and the average  $R_{TP}$  was used to determine  $R_i/R_0$  ratios. Resistances, estimated to the nearest micro-ohm and extrapolated to zero measuring currents, were used throughout these intercomparisons. Table III gives the average resistance ratios,  $R_i/R_0$ , that were determined for the 11 thermometers at the test points and also lists the quadratic temperature coefficients  $A$  and  $B$  that were calculated from the measurements at the ice, steam, and zinc points.

TABLE III

Thermometer	Fully corrected zero current resistance ratios: steam realization temperature 99.86763°C; metal points normalized to a total pressure of 1 atm				Quadratic temperature coefficients based on ice, steam, zinc	
	$R_{st}/R_0$	$R_{Bn}/R_0$	$R_{Cd}/R_0$	$R_{Zn}/R_0$	$A \times 10^3$	$B \times 10^7$
<b>1956</b>						
S214	1.39212035	1.89264541	2.21892282	2.56861904	3.9848856	-5.856222
S155	1.39210041	1.89260079	2.21886043	2.56853886	3.9846832	-5.855955
S163	1.39193349	1.89221177	2.21832214	2.56783756	3.9830120	-5.855965
S165	1.39192918	1.89219941	2.21830378	2.56781355	3.9829731	-5.856406
S178	1.39191626	1.89217315	2.21827005	2.56777075	3.9828353	-5.855550
S261	1.39197963	1.89232307	2.21847404	2.56802259	3.9834805	-5.856620
S175	1.39195885	1.89226756	2.21840045	2.56793935	3.9832694	-5.856317
S156	1.39200769	1.89238655	2.21856696	2.56815750	3.9837488	-5.855349
S144	1.39196268	1.89228053	2.21841816	2.56796355	3.9833017	-5.855713
<b>1958</b>						
E.1	1.39156404	1.89135708	2.21714556	2.56631067	3.9792940	-5.854101
A.1	1.39211242	1.89262628	2.21889296	2.56857252	3.9848161	-5.857208
S156	1.39200865	1.89239057	2.21857004	2.56816222	3.9837580	-5.855300
S155	1.39209953	1.89260170	2.21886236	2.56854143	3.9846699	-5.855490

\*R. J. Berry and D. R. Lovejoy tended the closed hygrometer during the 1956 steam point (realization temperature 99.86763°C) measurements and R. J. Berry and H. Scardina determined the  $\alpha$  values on the four thermometers in 1958.

†This research has now been completed and a detailed account of the investigation will be published shortly: samples of nominal 99.9999% purity Sn have been found that have such narrow alloy melting ranges that any ambiguity, arising from unknown impurity concentrations, in specifying the liquidus point of pure tin is well inside 0.001°C.

Table IV gives the average calculated temperatures for the two freezes made with each thermometer at the tin and cadmium points derived from quadratics

TABLE IV

Thermometer	Vertex* temp. of $R-T$ parabola ( $-A/2B$ ), °C	Calculated temperatures			From cubic equations based on ice, steam, Cd, Zn
		$t_{\text{Sn}}$ , °C	$t_{\text{Cd}}$ , °C	$t_{\text{Cd}} - t_{\text{Sn}}$ , °C	
<b>1956</b>					
S214	3402.3	231.91179	321.03260	89.12081	231.91172
S155	3402.2	204	256	052	200
S163	3400.8	166	208	042	199
S165	3400.5	140	172	032	202
S178	3400.9	169	219	050	194
S261	3400.8	332	437	105	183
S175	3400.8	112	189	077	160
S156	3401.8	182	262	080	172
S144	3401.2	172	220	048	195
<b>1958</b>					
E.1	3398.7	100	148	048	181
A.1	3401.6	242	332	090	176
S156	3401.8	225	252	027	224
S155	3402.5	244	294	050	208
Average		231.91190	321.03250	89.12060	231.91190
Std. deviation		±0.00062	±0.00075	±0.00024	±0.00018
Spread		0.00232	0.00289	0.00078	0.00064
Average ex S261		231.91178	321.03234	89.12056	
Std. deviation		±0.00046	±0.00052	±0.00020	
Spread		0.00144	0.00184	0.00063	
N.R.C. temp.		231.9119	321.0325	89.1206	231.9119

\*See Stimson (1953).

fixed at the ice, steam, and zinc points and tin temperatures obtained from cubic equations fixed at the ice, steam, cadmium, and zinc points. A value of 419.5050° C\* was used for the liquidus point of New Jersey S.P. zinc under a total pressure of 1 atmosphere in these calculations and a value of 321.03250° C was used for the liquidus point of New Jersey S.P. cadmium under 1 atmosphere in the cubic calculations. These results show that only one thermometer, S261, gave calculated temperatures for the Sn and Cd points that deviated by more than 0.001° C from the average obtained for the 11 thermometers. It is therefore difficult to prove that a statistically significant deviation from a true quadratic was found for any thermometer.

Further information on eight of the Meyers thermometers is given in Table V, which shows temperatures that were calculated on four fixed points using thermometer temperature coefficients  $A$  and  $B$  that were determined at the National Bureau of Standards (Washington) during the interval 1951-55 inclusive. This group of thermometers had been both transported and variously

\*At the June 20-21, 1958, meeting of the Comité Consultatif de Thermométrie of the Bureau International des Poids et Mesures, a value of 419.505° C (Int. 1948) was adopted for the liquidus point of pure zinc (see C.I.P.M. (1958)).

subjected to high and low temperature environments following the N.B.S. calibrations. It is interesting, therefore, to observe that the average values of the four fixed points using the N.B.S. calibrations are within about  $0.001^{\circ}\text{C}$  of the current N.R.C. values on the same points.

TABLE V

Calculated temperatures at four fixed points determined with eight Meyers thermometers using N.B.S. calibration constants: N.R.C. steam realization temperature  $99.86763^{\circ}\text{C}$

Thermometer	$t_{\text{steam}}$	$t_{\text{Sn}}$	$t_{\text{Cd}} - t_{\text{Sn}}$	$t_{\text{Cd}}$	$t_{\text{Zn}}$
1956					
S214	99.8684	231.9100	89.1192	321.0292	419.5008
S155	77	02	1196	.0298	03
S163	92	26	1198	.0324	28
S165	83	17	1204	21	51
S178	87	19	1199	18	49
S261	84	30	1199	29	19
S175	84	09	1208	17	46
S156	97	35	1217	52	88
Average	99.8686	231.9117	89.1202	321.0319	419.5036
N.B.S. temp.	99.8686	231.912	89.1202	321.032	419.504

## DISCUSSION

Following the general treatments of the effects of calibration errors on subsequent temperature measurements given by Hoge and Brickwedde (1942) and the Mendeleev Institute of Metrology (1955) estimates have been made of the standard deviations that would be expected for measurements at the Sn and Cd points with thermometers that are calibrated at the steam and zinc points.

In general, the resistance-temperature quadratic at any temperature,  $t$ , has the form

$$(1) \quad \begin{aligned} a &= At + Bt^2 & \text{where } a &= [(R_t/R_0) - 1] \\ a_1 &= At_1 + Bt_1^2 & a_1 &= [(R_1/R_0) - 1] \\ a_2 &= At_2 + Bt_2^2 & a_2 &= [(R_2/R_0) - 1] \\ A &= \frac{a_2 t_2^2 - a_1 t_1^2}{t_1 t_2 (t_2 - t_1)}; & B &= \frac{a_2 t_1 - a_1 t_2}{t_1 t_2 (t_2 - t_1)} \end{aligned}$$

and  $R_t$ ,  $R_0$ ,  $R_1$ ,  $R_2$  are the fully corrected resistances of the platinum thermometers at the test point, ice point, steam point, and zinc point respectively; here  $t_1 = t_{\text{steam}}$  and  $t_2 = t_{\text{zinc}}$ . The temperature coefficients of resistivity  $A$  and  $B$  are regarded as calibration 'constants' of a platinum thermometer.

The total differential of  $t$  may be written as

$$(2) \quad dt = \frac{\partial t}{\partial t_1} dt_1 + \frac{\partial t}{\partial t_2} dt_2 + \frac{\partial t}{\partial a_1} da_1 + \frac{\partial t}{\partial a_2} da_2 + \frac{\partial t}{\partial a} da$$

and the square standard deviation in  $t$  as

$$(3) \quad S^2 = \left( \frac{\partial t}{\partial t_1} \right)^2 s_1^2 + \left( \frac{\partial t}{\partial t_2} \right)^2 s_2^2 + \left( \frac{\partial t}{\partial a_1} \right)^2 s_3^2 + \left( \frac{\partial t}{\partial a_2} \right)^2 s_4^2 + \left( \frac{\partial t}{\partial a} \right)^2 s_5^2$$

where  $s_t$  are the standard deviations in the quantities  $t_1$ ,  $t_2$ ,  $a_1$ ,  $a_2$ , and  $a$  respectively;  $s_1$  and  $s_2$  represent errors in the 'realization temperatures' at the steam and zinc points and  $s_3$ ,  $s_4$ , and  $s_5$  represent uncertainties caused by errors in resistance measurements and resistance calibrations. These latter terms also reflect the errors caused by variations in the water triple-cell temperature and by the non-statistical increase in  $R_0$  caused by accidental cold-working of the thermometer during a series of measurements:  $s_6$  includes the realization error at the test point.

The differential coefficients (see Appendix) in equation (3) were evaluated for  $t = t_{\text{Sn}}$  and  $t = t_{\text{Cd}}$  when  $t_1 = 100^\circ \text{C}$  and  $t_2 = 419.5^\circ \text{C}$ . By assuming

$$s_1 = s_2 = \pm 0.0002^\circ \text{C}$$

and

$$s_3 = s_4 = s_5 = \pm 1 \times 10^{-6}$$

the expected total standard deviations,  $S_{\text{Sn}}$  and  $S_{\text{Cd}}$  for a series of measurements at  $t_{\text{Sn}}$  and  $t_{\text{Cd}}$  were calculated: the results are given in Table VI.

TABLE VI  
Evaluation of  $S_{\text{Sn}}$  and  $S_{\text{Cd}}$ :  
 $t_1 = 100^\circ \text{C}$ ;  $t_2 = 419.5^\circ \text{C}$ ;  $a_1 = 0.3925$ ;  $a_2 = 1.5682$

	Tin	Cadmium
$\partial t / \partial t_1$	1.42	1.06
$\partial t / \partial t_2$	0.215	0.514
$\partial t / \partial a_1$	-367 deg.	-274 deg.
$\partial t / \partial a_2$	-61.5 deg.	-147 deg.
$\partial t / \partial a$	-269 deg.	-280 deg.
$S$ (calc.)	$\pm 0.00054$ deg.	$\pm 0.00048$ deg.
$S$ (obs.)	$\pm 0.00062$ deg.	$\pm 0.00075$ deg.
$S$ (obs. ex S261)	$\pm 0.00046$ deg.	$\pm 0.00052$ deg.

Since (see Table VI) the observed  $S_{\text{Sn}}$  and  $S_{\text{Cd}}$  agree very closely with the values of these quantities that were calculated using reasonably stringent criteria\* for the precision attainable in thermometry, it is concluded that distinctive deviations from quadratic relations were not found for the 11 thermometers. Two additional observations follow from this conclusion: the use of cubic resistance-temperature relations is not required for these 11 thermometers and the verification of the close agreement among the thermometers indirectly attests to the high reproducibility of the liquidus points of high purity Sn and Cd as secondary fixed points.

\*It should be remembered that these precision criteria are applicable to the experimental conditions of this intercomparison; measurements were made with each thermometer on only two independent freezes at each metal freezing point and one determination at the steam point, with resistances at the triple point of water being determined before and after each measurement at the other fixed points. It would be possible to increase the precision slightly by using average temperatures from larger series of measurements at each fixed point but the time and effort required for such measurements is hardly justified in view of the high precision that is readily realizable with fewer measurements.

The close quadratic agreement of the resistance-temperatures found for the 11 thermometers together with the simplicity of the realizations and the high reproducibilities of the liquidus points of high purity indium, tin, and cadmium provide a serious challenge to the continued use of a precision steam point as a primary fixed point on the International Temperature Scale. It appears entirely possible that values for the liquidus points of high purity samples of these metals could be assigned with as high a precision as that given any point on the International Temperature Scale.

Further if one considers the temperature range 0° to 420° C and fixes the quadratic of equation (1) at the ice and zinc points, it is possible to show that a preferred location for the third fixed point,  $t_1$ , occurs at a value of  $t_1 \cong t_2/2$  for which the effects of the temperature and measurement realization errors  $s_1$  and  $s_3$  respectively in  $t_1$  are minimized in subsequent temperature interpolations anywhere in this range.

We may write

$$(4) \quad S_{t_1}^2 = \left( \frac{\partial t}{\partial t_1} \right)^2 s_1^2 + \left( \frac{\partial t}{\partial a_1} \right)^2 s_3^2$$

where  $S_{t_1}$  is the resultant standard deviation in temperature at temperature  $t$  arising from the standard deviation errors  $s_1$  and  $s_3$  in the realization of  $t_1$ . By inspection, regardless of the location of  $t_1$ , the numerators of the differential coefficients  $\partial t/\partial t_1$  and  $\partial t/\partial a_1$  (see Appendix) have maxima for  $t = t_2/2$  and since the denominators of these coefficients are nearly constant over the range 0° to  $t_2$ , it follows that  $S_{t_1}$  has maximum values at  $t \cong t_2/2$ . Therefore in order to minimize the error in interpolated temperatures arising from these realization errors in  $t_1$ , the third fixed point, other considerations being equal, should have the value  $t_1 \cong t_2/2$ . Table VII gives evaluations of  $S_{t_1}$  for a typical thermometer at various values of  $t$  for five locations of  $t_1$  when  $s_1 = \pm 0.0002^\circ \text{C}$  and  $s_3 = \pm 1 \times 10^{-6}$ .

TABLE VII  
 $S_{t_1}(10^{-4}^\circ \text{C})$  when  $s_1 = \pm 0.0002^\circ \text{C}$ ,  $s_3 = \pm 1 \times 10^{-6}$

$t$ , °C	$t_1$ , °C				
	$t_{\text{steam}}$ 100	$t_{\text{In}}$ 157	210	$t_{\text{Sn}}$ 232	$t_{\text{Cd}}$ 321
20	0.8	0.6	0.6	0.6	0.8
100	3.3	2.5	2.3	2.4	3.3
210	4.7	3.6	3.3	3.4	4.6
300	3.9	3.0	2.8	2.8	3.8
400	0.9	0.7	0.6	0.6	0.8

An additional function

$$(5) \quad [g(\epsilon)]_{t_2/2} = [S_{t_1}/S_{t_1=t_2/2}]_{t_2/2}$$

has been evaluated for  $t_1 = 100, 157, 210, 232$ , and  $321^\circ \text{C}$  with corresponding

values of  $a_1 = 0.3925, 0.6095, 0.8108, 0.8924$ , and  $1.2186$  when  $t = t_2/2 = 210^\circ\text{C}$ ;  $t_2 = 420^\circ\text{C}$  and  $a_2 = 1.5700$ , by assuming  $s_1 = \pm 0.0002^\circ\text{C}$  and  $s_3 = \pm 1 \times 10^{-6}$  (i.e. it is assumed that the 'realization errors' in the third fixed point are the same for the steam, indium, tin, and cadmium points). Table VIII lists these results from which it is concluded that the tin and indium ( $156.611^\circ\text{C}$  (Int.)) points have algebraic advantages over the steam point as the third fixed point for thermometer calibrations.

TABLE VIII

Relative maximum error introduced into temperature determinations in the range  $0^\circ$  to  $420^\circ\text{C}$  caused by the same 'realization errors' at the third fixed point,  $t_1$ , in the thermometer calibration: evaluated for  $t_2 = 420$ , when  $t = t_2/2 = 210$  for various values of  $t_1$

$t_1, ^\circ\text{C}$	$(\partial t / \partial t_1)_{t_2/2}$	$(\partial t / \partial a_1)_{t_2/2}$ , deg.	$[S_{t_1}]_{t_2/2}, ^\circ\text{C}$	$g(\epsilon)_{t_2/2}$
210	1.000	-268	$\pm 0.000334$	1.00
100	1.426	-369	$\pm 0.000466$	1.40
157	1.085	-286	$\pm 0.000359$	1.07
232	1.004	-271	$\pm 0.000337$	1.01
321	1.339	-371	$\pm 0.000458$	1.37

For these reasons, it is hoped that in the next few years other national laboratories will carry out investigations on these secondary fixed points to test their usefulness as aids in the establishment and realization of the International Temperature Scale.

## CONCLUSION

The intercomparison of the 11 standard thermometers has demonstrated the usefulness of the liquidus points of high purity metals as precision thermometric fixed points in the establishment and the examination of the temperature scale in the range  $0^\circ$  to  $420^\circ\text{C}$  (Int.). The experimental verification of the high precision to which the quadratic approximation may be used to relate the resistances of the platinum thermometers to their temperatures in this range opens the way to the utilization of the liquidus points of high purity indium, tin, and cadmium as precision alternatives to the steam point on the International Temperature Scale.

## ACKNOWLEDGMENTS

The author is grateful to Mr. E. G. Murdock for his capable assistance in carrying out these measurements and calculations and to Dr. W. R. Dixon for some useful discussions.

## APPENDIX

The following algebraic expressions were used in the thermometer calibrations, in the temperature calculations at the Sn and Cd points, and in the estimates of the effects of calibration and measuring errors on subsequent temperature determinations.

## 1. Quadratic

$$[(R_t/R_0) - 1] = a = At + Bt^2$$

$$a_1 = At_1 + Bt_1^2; \quad a_2 = At_2 + Bt_2^2$$

$$A = \frac{a_1 t_2^2 - a_2 t_1^2}{t_1 t_2 (t_2 - t_1)}; \quad B = \frac{a_2 t_1 - a_1 t_2}{t_1 t_2 (t_2 - t_1)}$$

$$\frac{\partial t}{\partial t_1} = \frac{t(t_2 - t)[a_1 t_2 (t_2 - 2t_1) + a_2 t_1^2]}{t_1 (t_2 - t_1)[a_1 t_2 (t_2 - 2t) - a_2 t_1 (t_1 - 2t)]}$$

$$\frac{\partial t}{\partial t_2} = \frac{t(t_1 - t)[a_2 t_1 (t_1 - 2t_2) + a_1 t_2^2]}{t_2 (t_2 - t_1)[a_1 t_2 (t_2 - 2t) - a_2 t_1 (t_1 - 2t)]}$$

$$\frac{\partial t}{\partial a_1} = \left[ \frac{t_2(t_2 - t)}{a_1 t_2 (2t - t_2) - a_2 t_1 (2t - t_1)} \right]$$

$$\frac{\partial t}{\partial a_2} = \left[ \frac{t_1(t_1 - t)}{a_2 t_1 (2t - t_1) - a_1 t_2 (2t - t_2)} \right]$$

$$\frac{\partial t}{\partial a} = \left[ \frac{t_1 t_2 (t_2 - t_1)}{a_2 t_1 (2t - t_1) - a_1 t_2 (2t - t_2)} \right].$$

Temperatures are calculated (see Schwab and Wickers (1945)) using two successive solutions of the relation

$$t = \frac{[(R_t/R_0) - 1] + Bt_e^2}{A + 2Bt_e}$$

where  $t_e$  is a first estimate.

## 2. Cubic

$$[(R_t/R_0) - 1] = a = At + Bt^2 + Dt^3$$

$$a_1 = At_1 + Bt_1^2 + Dt_1^3$$

$$a_2 = At_2 + Bt_2^2 + Dt_2^3$$

$$a_3 = At_3 + Bt_3^2 + Dt_3^3$$

$$A = \left\{ \frac{a_1 t_2^2 t_3^2 (t_3 - t_2) + a_2 t_3^2 t_1^2 (t_1 - t_3) + a_3 t_1^2 t_2^2 (t_2 - t_1)}{t_1 t_2 t_3 [t_1 (t_2^2 - t_3^2) + t_2 (t_3^2 - t_1^2) + t_3 (t_1^2 - t_2^2)]} \right\}$$

$$B = \left\{ \frac{a_1 t_2 t_3 (t_2^2 - t_3^2) + a_2 t_3 t_1 (t_3^2 - t_1^2) + a_3 t_1 t_2 (t_1^2 - t_2^2)}{t_1 t_2 t_3 [t_1 (t_2^2 - t_3^2) + t_2 (t_3^2 - t_1^2) + t_3 (t_1^2 - t_2^2)]} \right\}$$

$$D = \left\{ \frac{a_1 t_2 t_3 (t_3 - t_2) + a_2 t_3 t_1 (t_1 - t_3) + a_3 t_1 t_2 (t_2 - t_1)}{t_1 t_2 t_3 [t_1 (t_2^2 - t_3^2) + t_2 (t_3^2 - t_1^2) + t_3 (t_1^2 - t_2^2)]} \right\}.$$

Temperatures are calculated using two successive solutions of the relation

$$t = \frac{[(R_t/R_0) - 1] + Bt_e^2 + 2Dt_e^3}{A + 2Bt_e + 3Dt_e^2}$$

where  $t_e$  is a first estimate.

## REFERENCES

BARBER, C. R. 1950. *J. Sci. Instr.* **27**, 47.  
— 1955. Comité International des Poids et Mesures, Procès-Verbaux des Séances de 1954, **24**, T116, T167.  
BERRY, R. J. 1958. *Can. J. Phys.* **36**, 740.  
COMITÉ INTERNATIONAL DES POIDS ET MESURES. 1958. Comité Consultatif de Thermométrie, Procès-Verbaux des Séances de 1958, t.26.  
HALL, J. A. 1955. Temperature, its measurement and control in science and industry, Vol. 2 (Reinhold Publishing Corp., New York), p. 132.  
HOGE, H. J. and BRICKWEDDE, F. G. 1942. *J. Research NBS*, **28**, 217.  
MCCLAREN, E. H. 1957a. *Can. J. Phys.* **35**, 78.  
— 1957b. *Can. J. Phys.* **35**, 1086.  
— 1958a. *Can. J. Phys.* **36**, 585.  
— 1958b. *Can. J. Phys.* **36**, 1131.  
MENDELEEV INSTITUTE OF METROLOGY, LENINGRAD, U.S.S.R. 1955. Comité International des Poids et Mesures, Procès-Verbaux des Séances de 1954, **24**, T122.  
MEYERS, C. H. 1932. *J. Research NBS*, **9**, 807.  
SCHWAB, F. W. and WICHERS, E. 1945. *J. Research NBS*, **34**, 333.  
STIMSON, H. F. 1953. Comité International des Poids et Mesures, Procès-Verbaux des Séances de 1952, **23B**, T104.  
— 1955. Temperature, its measurement and control in science and industry, Vol. 2 (Reinhold Publishing Corp., New York), p. 149.

# SOLUTION OF THE HUND GRAVITATIONAL EQUATIONS<sup>1</sup>

LL. G. CHAMBERS

## ABSTRACT

Solutions are indicated for the Maxwell type gravitational field equations developed by Hund in the realization of Mach's program. These solutions are of interest in connection with recent work by Kaempfier.

## 1. INTRODUCTION

Hund (1948) has suggested that gravitational fields may be expressed in terms of a polar vector  $\mathbf{f}$  and an axial vector  $\mathbf{g}$  which act upon any gravitational mass  $m$  with the force

$$(1) \quad \mathbf{F} = m\{\mathbf{f} + \mathbf{v} \times \mathbf{g}\},$$

$\mathbf{v}$  being the velocity of the mass. The fields  $\mathbf{f}$  and  $\mathbf{g}$  satisfy the following differential equations.

$$(2) \quad \nabla \cdot \mathbf{g} = 0,$$

$$(3) \quad \nabla \times \mathbf{f} = -\frac{1}{c} \frac{\partial \mathbf{g}}{\partial t},$$

$$(4) \quad \nabla \cdot \mathbf{f} = -4\pi\gamma\rho + (|f|^2 + |g|^2)/(2c^2),$$

$$(5) \quad \nabla \times \mathbf{g} = \frac{1}{c} \frac{\partial \mathbf{f}}{\partial t} - \frac{4\pi\gamma}{c} \rho \mathbf{v} + \frac{1}{c^2} (\mathbf{f} \times \mathbf{g}).$$

Kaempfier (1958) has indicated a method which uses successive approximations to evaluate the field vectors  $\mathbf{f}$  and  $\mathbf{g}$ . Solutions of Hund's equations are of interest in connection with Kaempfier's work and may help in going beyond the solutions considered by Kaempfier.

## 2. SOLUTION FOR $\mathbf{f}$

Hund showed that

$$(6) \quad \mathbf{f} \cdot \rho \mathbf{v} = c^2 \left\{ \nabla \cdot (\rho \mathbf{v}) + \frac{\partial \rho}{\partial t} \right\}.$$

The solution of this is clearly

$$(7) \quad \mathbf{f} = \frac{\mathbf{v} c^2}{v^2 \rho} \left\{ \nabla \cdot (\rho \mathbf{v}) + \frac{\partial \rho}{\partial t} \right\} + \mathbf{P} \times \mathbf{v}$$

where  $\mathbf{P}$  is an arbitrary vector.

<sup>1</sup>Manuscript received November 28, 1958.

Contribution from the Department of Mathematics, University College of North Wales, Bangor, Caernarvonshire, Wales.

An alternate form for this is

$$(8) \quad \mathbf{f} = \frac{\mathbf{v}c^2}{v^2} \left\{ \nabla \cdot \mathbf{v} + \frac{d}{dt} (\log \rho) \right\} + \mathbf{P} \times \mathbf{v}$$

$$(9) \quad = \mathbf{f}_0 + \mathbf{P} \times \mathbf{v} \text{ say.}$$

Now the set of fields defined by

$$(10) \quad \mathbf{f} = \mathbf{f}_0 + \mathbf{P} \times \mathbf{v}, \quad \mathbf{g} = \mathbf{g}_0 - c\mathbf{P}$$

will give rise to the same force on a test particle as will  $\mathbf{f}_0, \mathbf{g}_0$ . It follows therefore that it will be convenient and possible to make  $\mathbf{P}$  zero, thus making  $\mathbf{f}$  parallel to  $\mathbf{v}$ .

Thus

$$(11) \quad \mathbf{f} = \frac{\mathbf{v}c^2}{v^2} \left\{ \nabla \cdot \mathbf{v} + \frac{d}{dt} (\log \rho) \right\}$$

and if there is no creation of matter, the second term vanishes leaving only one term and

$$(12) \quad \mathbf{f} = \frac{\mathbf{v}c^2}{v^2} \nabla \cdot \mathbf{v}.$$

Thus  $\mathbf{f}$  does not depend explicitly upon the density distribution.

### 3. SOLUTION OF $\mathbf{g}$

It is first necessary to point out that the derivation of  $\mathbf{g}$  differs according as to whether certain conditions are satisfied or not.

#### (a) $\partial \mathbf{g} / \partial t$ nonzero

Applying the divergence operator to equation (5) and rearranging

$$(13) \quad \mathbf{g} \cdot (\nabla \times \mathbf{f}) = \mathbf{f} \cdot (\nabla \times \mathbf{g}) + 4\pi\gamma c \nabla \cdot (\rho \mathbf{v}) - c \frac{\partial}{\partial t} (\nabla \cdot \mathbf{f}).$$

Using equation (5) it can easily be shown that equation (13) assumes the form

$$(14) \quad \mathbf{g} \cdot \boldsymbol{\alpha} = A$$

where

$$(15) \quad \boldsymbol{\alpha} = \nabla \times \mathbf{f} = -\frac{1}{c} \frac{\partial \mathbf{g}}{\partial t}$$

and

$$(16) \quad A = \frac{\partial}{\partial t} \left\{ f^2 / (2c) + c \nabla \cdot \mathbf{f} \right\} + 4\pi\gamma \left\{ c \nabla \cdot (\rho \mathbf{v}) - \frac{1}{c} \rho \mathbf{f} \cdot \mathbf{v} \right\}.$$

(The second term in curly brackets reduces to  $-(1/c)(\partial \rho / \partial t)$ .)

The solution of equation (14) is

$$(17) \quad \mathbf{g} = \mathbf{g}_1 + \mathbf{Q}$$

where

$$(18) \quad \mathbf{g}_1 = A\mathbf{a}/\alpha^2$$

and  $\mathbf{Q}$  is an arbitrary vector perpendicular to  $\mathbf{a}$ .

Now in this solution for  $\mathbf{g}$ , it will be noted that equations (3) and (5) have been used and (2) and (4) have not, and accordingly it is necessary to adjust the arbitrary vector  $\mathbf{Q}$  so that the equations (1) and (3) are satisfied.

This is done as follows:

If  $\mathbf{g}$  is not solenoidal, suppose that  $\mathbf{g}_1'$  is a vector perpendicular to  $\mathbf{a}$ , such that the vector  $\mathbf{g}_1 + \mathbf{g}_1'$  is solenoidal. Then if  $\mathbf{Q}'$  is an arbitrary vector such that

$$(19) \quad \mathbf{a} \cdot (\nabla \times \mathbf{Q}') = 0$$

the vector

$$(20) \quad \mathbf{g} = \mathbf{g}_1 + \mathbf{g}_1' + \nabla \times \mathbf{Q}'$$

satisfies equations (2), (3), and (5), and  $\mathbf{Q}'$  must be adjusted so that (4) is satisfied.

Any vector parallel to  $\mathbf{v}$  may be added to  $\mathbf{g}_1'$  and  $\nabla \times \mathbf{Q}'$ . This is because  $\mathbf{g}$  is only meaningful in the combination  $\nabla \times \mathbf{g}$ .

$$(b) \quad \partial \mathbf{g} / \partial t = 0, \quad \partial f / \partial t \neq 0$$

Differentiating equation (5) with respect to time

$$(21) \quad \nabla \times \frac{\partial \mathbf{g}}{\partial t} = \frac{1}{c} \frac{\partial^2 \mathbf{f}}{\partial t^2} - \frac{4\pi\gamma}{c} \frac{\partial}{\partial t} (\rho \mathbf{v}) + \frac{1}{c^2} \left( \mathbf{f} \times \frac{\partial \mathbf{g}}{\partial t} \right) + \frac{1}{c^2} \left( \frac{\partial \mathbf{f}}{\partial t} \times \mathbf{g} \right).$$

That is

$$(22) \quad 0 = \frac{1}{c} \frac{\partial^2 \mathbf{f}}{\partial t^2} - \frac{4\pi\gamma}{c} \frac{\partial}{\partial t} (\rho \mathbf{v}) + \frac{1}{c^2} \left( \frac{\partial \mathbf{f}}{\partial t} \times \mathbf{g} \right).$$

This is of the form

$$(23) \quad \mathbf{g} \times \beta = \mathbf{B}$$

where

$$(24) \quad \beta = \partial \mathbf{f} / \partial t$$

$$(25) \quad \mathbf{B} = c \frac{\partial^2 \mathbf{f}}{\partial t^2} - 4\pi\gamma c \frac{\partial}{\partial t} (\rho \mathbf{v}).$$

The solution of equation (23) is

$$(26) \quad \mathbf{g} = \mathbf{g}_2 + \lambda \beta$$

where

$$(27) \quad \mathbf{g}_2 = \frac{\beta \times \mathbf{B}}{|\beta|^2}$$

and  $\lambda$  is arbitrary.

This solution is permissible provided that  $\mathbf{g}$  is nonzero and orthogonal to  $\mathbf{B}$ . The latter is easily proved, for

$$\frac{\partial \mathbf{f}}{\partial t} \cdot \left\{ \frac{\partial^2 \mathbf{f}}{\partial t^2} - 4\pi\gamma \frac{\partial}{\partial t} (\rho \mathbf{v}) \right\} = \frac{\partial \mathbf{f}}{\partial t} \cdot \left\{ c \left( \nabla \times \frac{\partial \mathbf{g}}{\partial t} \right) + \frac{1}{c} \left( \mathbf{f} \times \frac{\partial \mathbf{g}}{\partial t} \right) + \frac{1}{c} \left( \frac{\partial \mathbf{f}}{\partial t} \times \mathbf{g} \right) \right\}$$

(on differentiating equation (5) with respect to time)

$$= \frac{\partial \mathbf{f}}{\partial t} \cdot \left\{ \frac{1}{c} \frac{\partial \mathbf{f}}{\partial t} \times \mathbf{g} \right\} = 0.$$

It will be observed that equations (2) and (4) have not been used. In order that they be satisfied, it is necessary that operations similar to those for the case of  $\partial \mathbf{g} / \partial t$  nonzero be carried out. Presumably, for an actual distribution of  $\rho$  and  $\mathbf{v}$  such operations could be done numerically, or by inspection in certain cases.

#### 4. STEADY UNIVERSE

Suppose now that  $\partial \mathbf{f} / \partial t$  and  $\partial \mathbf{g} / \partial t$  vanish. From equation (22), it follows that

$$(28) \quad (\partial / \partial t)(\rho \mathbf{v}) = 0$$

and differentiating equation (4) with respect to time, it is easy to see that

$$(29) \quad \partial \rho / \partial t = 0.$$

It follows from equation (28) that either  $\rho$  or  $\partial \mathbf{v} / \partial t$  vanishes. Should this latter be the case, everything is independent of time and the universe may be said to be steady.

In this case equations (2) and (4) remain in their original forms, but equations (3) and (5) become

$$(3)^1 \quad \nabla \times \mathbf{f} = 0,$$

$$(5)^1 \quad \nabla \times \mathbf{g} = -\frac{4\pi\gamma}{c} \rho \mathbf{v} + \frac{1}{c^2} (\mathbf{f} \times \mathbf{g}).$$

It does not seem possible to obtain general solutions to the system of equations (2), (3)<sup>1</sup>, (4), (5)<sup>1</sup>. However, a particular solution might be obtained as follows. Assume  $\mathbf{f}$  to vanish, that is  $\mathbf{v}$  is solenoidal. Then  $\partial \mathbf{f} / \partial t$  is zero,  $\partial \mathbf{g} / \partial t$  vanishes by virtue of equation (3), and (3)<sup>1</sup> is trivially satisfied. Equation (4) becomes

$$(30) \quad g^2 = 8\pi\gamma\rho c^2$$

and (5)<sup>1</sup> becomes

$$(31) \quad \nabla \times \mathbf{g} = -\frac{4\pi\gamma}{c} \rho \mathbf{v}.$$

This last equation may be rewritten as

$$-\nabla \times (\nabla \times \mathbf{g}) = \frac{4\pi\gamma}{c} \nabla \times (\rho \mathbf{v})$$

and using equation (2)

$$(32) \quad \nabla^2 \mathbf{g} = \frac{4\pi\gamma}{c} \nabla \times (\rho \mathbf{v})$$

the solution of which is

$$(33) \quad \mathbf{g}(\mathbf{r}) = -\frac{\gamma}{c} \int \frac{\nabla' \times \{\rho(\mathbf{r}') \mathbf{v}(\mathbf{r}')\} d\mathbf{r}'}{|\mathbf{r} - \mathbf{r}'|}$$

to which, however, may be added any solution of  $\nabla^2 \mathbf{g} = 0$  which also satisfies  $\nabla \cdot \mathbf{g} = 0$  (e.g.  $\mathbf{g} = \nabla u$  where  $\nabla^2 u = 0$ ). This complementary function must be such that the whole solution satisfies equation (30).

### 5. UNIVERSE DEVOID OF MATTER (GEONS)

If  $\rho$  is identically zero, equations (2) to (5) become

$$(2) \quad \nabla \cdot \mathbf{g} = 0$$

$$(3) \quad \nabla \times \mathbf{f} = -\frac{1}{c} \frac{\partial \mathbf{g}}{\partial t}$$

$$(4)'' \quad \nabla \cdot \mathbf{f} = (\mathbf{f}^2 + \mathbf{g}^2)/(2c^2)$$

$$(5)'' \quad \nabla \times \mathbf{g} = (\mathbf{f} \times \mathbf{g})/c^2 + \frac{1}{c} \frac{\partial \mathbf{f}}{\partial t}.$$

By virtue of the nonlinearity of the equations, nonzero solutions are possible, e.g. in spherical co-ordinates  $\mathbf{f} = 2c^2 \hat{\mathbf{r}}/r$ ,  $\mathbf{g} = 0$ . Such solutions correspond to the geons of general relativity investigated in great detail by Wheeler (1955). In these cases, the universe is full of gravitational field energy, giving an effective mass density and there is a self-maintained gravitational field concentration which is, so to speak, held together by its own weight.\* The discussion of such fields will be reserved for further consideration.

### REFERENCES

HUND, F. 1948. Z. Physik, **124**, 742.  
 KAEMPFER, F. A. 1958. Can. J. Phys. **36**, 151.  
 WHEELER, J. A. 1955. Phys. Rev. **97**, 511.

\*I owe this interpretation to the referee.

# THE CHANGE OF RESISTANCE OF HYDROPHILIC FILMS SUBJECTED TO CONSTANT VOLTAGE<sup>1</sup>

C. D. NIVEN

## ABSTRACT

Graphs illustrate changes in resistance of gelatin and cellophane films when voltage is applied to them over a period of time and the polarity is then reversed. The similarity in these graphs, as well as other evidence, suggests that the mechanism of conduction for gelatin applies also to cellophane. Riehl's theory is very slightly modified and used to explain the results.

## INTRODUCTION

Recent work on hydrophilic substances has led to the rejection of the old impurity-ion conception of conduction and has suggested instead the proton migration theory (Hearle 1953; Pollock and Ubbelohde 1956). Riehl (1956) has proposed a mechanism for proton migration which takes into account the Wien-Poole effect (rise of conductivity with rise of voltage) but does not consider the strange behavior of a gelatin film when voltage is applied to it over a period of time and if the polarity is then reversed: this effect was mentioned by the writer (Niven 1958) in another communication dealing with change of resistance with humidity in connection with the use of gelatin films as detectors of heat radiation. Since cellophane had also been used as a detector of thermal radiation it was desirable to ascertain if cellophane behaved in a similar manner. The investigation is described below.

## METHODS AND RESULTS

The gelatin film was prepared by dissolving 0.1 g of gelatin in 25 cc of boiling water and pouring the solution out on a surface of clean distilled mercury in a petri dish. The cellophane film was a piece of commercial cellophane which had been washed in water. The samples were coated with conducting rubber paint on either side so that the effective area of film through which voltage was applied was about 1/8 inch square. The applied voltage was 127 volts and the thickness of the film was about .001 inch so that the field was of the order of  $5 \times 10^4$  volts per cm, which is comparable with the fields which Riehl (1957) used. The resistance was measured on an ohmmeter. The samples were situated inside a humidity cabinet controlled by a sensing element and thermostat.

After the voltage had been left on the sample for some days the resistance-time relation had curved off showing that farther increase of resistance with time was negligible, provided the humidity and temperature remained constant. When the polarity of the applied voltage was reversed the resistance

<sup>1</sup>Manuscript received January 9, 1959.

Contribution from Division of Applied Physics, National Research Council, Ottawa, Canada.

Issued as N.R.C. No. 5109.

fell sharply from its steady value to a minimum and then rose—at first quite sharply and later more slowly—to a new steady value. Figure 1 illustrates this behavior for gelatin at 52% R.H. and 28° C in much greater detail than the graph already published (Niven 1958), because it demonstrates the effect of reversing the polarity three times and eventually cutting off the applied voltage altogether.

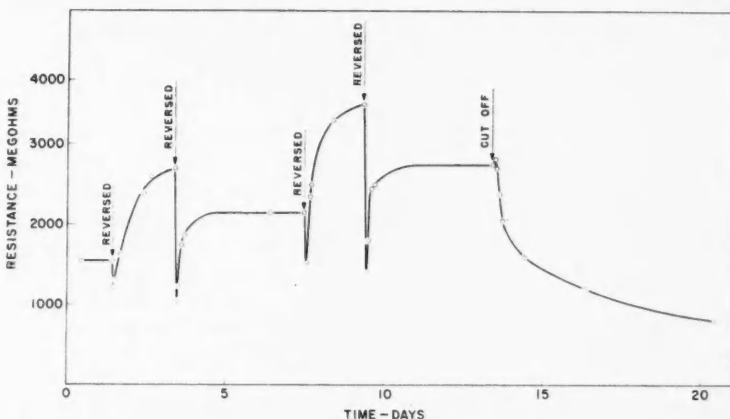


FIG. 1. Resistance vs. time curve for gelatin film. Field:  $5 \times 10^4$  volts/cm. Humidity: 52% R.H. Temperature: 28° C.

However, the important question to answer was whether or not cellophane would do the same sort of thing when the polarity was reversed. Measurements on cellophane first at a humidity of 52% and then of 73% yielded inconclusive results because the resistance kept rising linearly and showed no signs of curving off to a constant value at a few thousand megohms. Only when the humidity was raised to 80% were comparable results obtained. These are shown in Fig. 2. The two separate curves refer to two different pieces of cellophane cut from the sample of material and measured at the same time under similar humidity and temperature conditions, 80% R.H. and 28° C. Comparing Figs. 1 and 2 one sees a close resemblance in the behavior of gelatin and cellophane, which implies that any theory on the electrical conduction of hydrophilic films must take into consideration the very marked effect that turns up when polarity is reversed.

The higher humidity requirement of the cellophane can be appreciated by referring to some work of Bull (1944) on gelatin and some work of Filby and Maass (1935) on cellulose in connection with water absorption. According to Bull's data 100 g of dry gelatin will contain about 16.6 g of water when held in an atmosphere of 52% R.H. and 25° C—small changes of temperature are not important. According to data of Filby and Maass 100 g of dry cellulose will contain about 11.3 g of water when held in an atmosphere of 80% R.H. and 20° C—they only give results at 20° C. Altogether one gets the impression

that cellophane at 80% is really "drier" than gelatin at 52%—about two molecules of moisture in cellophane corresponding to three in gelatin.

The resistance values in the graphs are the actual measured values—not specific resistances.

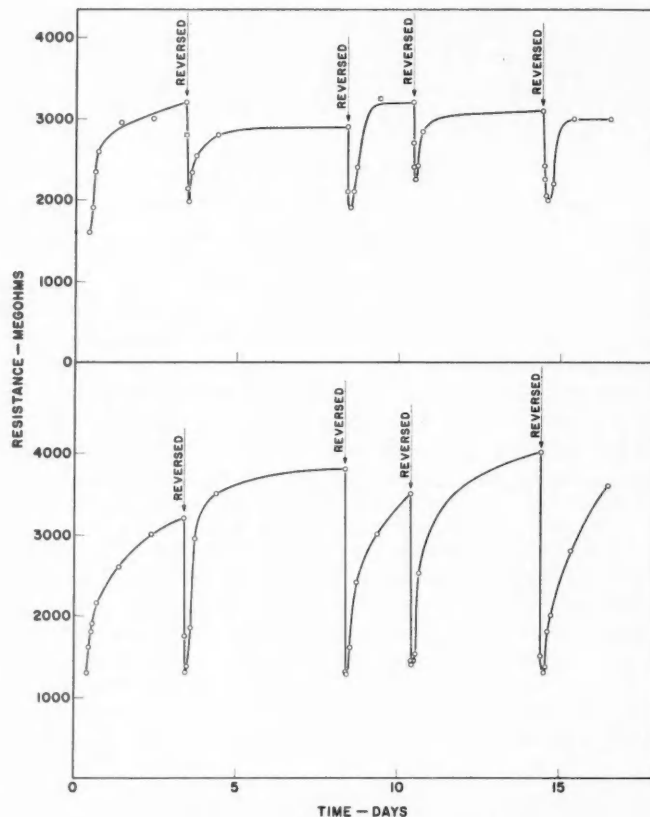


FIG. 2. Resistance vs. time curve for two cellophane films. Field:  $5 \times 10^4$  volts/cm. Humidity: 80% R.H. Temperature: 28°C.

#### DISCUSSION OF RESULTS

Riehl has assumed that the conduction mechanism in gelatin is similar to that in ice because the water structurally bound to the protein is immobilized. Since water keeps the tetrahedral molecular structure of ice after melting, chains of immobilized water molecules would appear to be essentially similar to chains of molecules in ice. In confirmation of this idea Riehl has shown that  $R$  in the conductivity-temperature relation  $K = K_0 e^{-R/RT}$  has the same

value for gelatin as for ice. The similarity between Figs. 1 and 2, coupled with the fact that cellophane and gelatin both respond to thermal radiation, suggested to the writer that if gelatin and ice have the same value of  $R$ —namely 21 kcal/mole—cellophane must have that value too. Fortunately it was not necessary to carry out the experimental work to determine this because Muss (1953) gives a value of  $21.3 \pm 0.7$  for the enthalpy of activity of d-c. conductivity of cellophane with a moisture regain of 0.3 to 0.4, and a value of  $21.7 \pm 1.6$  with a moisture regain of 2.4 to 2.8. The agreement with the figure 21 for ice and gelatin is excellent and this confirms the correctness of Riehl's assumption. Conduction in hydrophilic organic films appear to be independent of the chemical structure of the substance—at any rate to a first approximation—and depends on chains of water molecules reaching completely from one face to the other. This conclusion that chains of water molecules extend from face to face of the film throws some light on the diffusion process when water diffuses through a hydrophilic material, because it suggests that the movement is not to be regarded as the passage of a free molecule of water vapor through tiny pores but rather as a pushing of molecules in at one end of a chain and a pushing of molecules out at the other end.

Figures 1 and 2 suggest that some sort of change has taken place in the film when a charge passes down one of the chains of oriented molecules described by Riehl. Cutting off the voltage does not permit this change, whatever it is, to disappear instantaneously—in fact the return to the normal condition, although reasonably fast at first, is a gradual process which may last over days. On the other hand, reversal of the polarity speeds up the process and a period of only 1 or 2 hours is required to bring the resistance to a minimum from which it can start to rise again. To explain these results one might be tempted to suggest that the chains visualized by Riehl do not break up completely and that more and more molecules get into false orientation the longer the voltage is applied: however, this is too superficial an explanation and in any case would not meet with Riehl's requirement of disintegration (*Zerfall*) of the chains after passage of a proton.

By stressing the importance of the Pauling statistical model for ice (Owston 1958) rather than the Bernal-Fowler model one can assume a continual but irregular jumping of each proton between its two sites. The formation of a chain of oriented molecules simply implies that two or more jumps were sufficiently in phase to permit a proton to be passed along with the assistance of the field. However, as the jumps are random, they should immediately get out of phase again and a proton would be trapped at the end of the chain until another chain happened to form beyond that point, thus permitting the further passage of a proton toward the negative pole. This process would of course lead to an accumulation of protons on the side of the film near the negative pole—ready to be released and work back in the other direction as soon as the polarity was reversed or the voltage cut off—and it seems to fit experimental results. The fact that resistance remains finite after voltage has been applied for a long period of time suggests that some protons are supplied at the positive pole and removed at the negative pole.

## REFERENCES

BULL, H. B. 1944. *J. Am. Chem. Soc.* **66**, 1499.  
FILBY, E. and MAASS, O. 1935. *Can. J. Research, B*, **13**, 1.  
HEARLE, J. W. S. 1953. *J. Textile Inst.*, **44**, T177.  
NIVEN, C. D. 1958. *Trans. Faraday Soc.* **54**, 441.  
OWSTON, P. G. 1958. *Advances in Physics*, **7**, 171.  
POLLOCK, J. McC. and UBBELORDE, A. R. 1956. *Trans. Faraday Soc.* **52**, 1112.  
RIEHL, N. 1956. *Naturwissenschaften*, **43**, 145.  
——— 1957. *Kolloid-Z.* **151**, 66.

## SOME PHYSICAL PROPERTIES OF SEA ICE. I<sup>1</sup>

E. R. POUNDER AND E. M. LITTLE<sup>2</sup>

### ABSTRACT

This preliminary study is based mostly on work done at a shore station in Shippagan, N.B., during the winter of 1956-57, with some data from an ice-breaker expedition in the summer of 1956. The Shippagan site had unrafted ice, tides of 5 feet or less, and negligible fresh-water runoff. The thickness of the ice was about proportional to the square root of the freezing exposure. Tritium dating of sea ice is an unsatisfactory method because of variable tritium concentration in Arctic waters. The jaggedness of ice crystals is suggested as a measure combining effects of age and thermal regime. Measurements of specific gravity, salinity, electrical resistivity, and permeability profiles all show progressive changes in annual sea ice throughout the winter. The tensile strength of sea ice at -20°C was around 200 to 500 p.s.i., at various angles to the grain. For fresh-water ice, with stress parallel to the grain, it was in the range 500 to 1000 p.s.i. Shear strengths, with the shear plane parallel to the grain, were 80 to 160 p.s.i. for sea ice at -20°C and 160 to 280 p.s.i. for pond ice, also at -20°C.

### 1. INTRODUCTION

A project for the study of the physical properties of ice was set up at McGill University in 1955 under the sponsorship of the Defence Research Board of Canada. An important objective of this project is the study of sea ice, and to help initiate this phase of the work the U.S. Navy Electronics Laboratory sent the second author on loan to McGill for the period May 1956 to May 1957. During July to September he was one of nine scientists aboard H.M.C.S. *Labrador* on a cruise from Halifax to the eastern Canadian Arctic, being the only one of this party working on ice. In the fall of 1956 a survey was made of possible sites in eastern Canada for a shore station where sea ice could be studied, the factors of ice conditions, tides, precipitation, temperature regime, and logistics all being considered. A very suitable site was found near Shippagan, N.B., at 47°44' N., 64°45' W. The federal Department of Fisheries maintains a biological station at this point, in connection with the oyster trade, and kindly offered not only the use of the building during the winter months but also the assistance of the officer-in-charge of the station. This station has been used for ice research during the winters of 1956-57 and 1957-58. The present report deals with the results obtained during the winter of 1956-57 and on the cruise of the *Labrador* the previous summer. It must be emphasized that it represents a preliminary study only, more of a survey of work to be done than an attempt to establish definitive values of the various physical constants of sea ice.

Sea ice is a most inhomogeneous material, containing varying quantities of a number of salts—some in solution and some in solid form—and a considerable amount of entrapped air. Its structure, composition, and physical properties

<sup>1</sup>Manuscript received September 4, 1958.

Contribution from the Ice Research Project, Department of Physics, McGill University, Montreal, Que., and the U.S. Navy Electronics Laboratory, San Diego, California, U.S.A.

<sup>2</sup>Present address: U.S. Navy Electronics Laboratory, San Diego, California.

are dependent on its thermal history and vary widely between the limiting cases of new sea ice a few months old and Arctic pack ice of several years of age. Furthermore, the lack of homogeneity is sufficiently great that in small sample testing, results measured for a given parameter, such as tensile strength, show a considerable scatter even though the samples are cut from nearby locations in the ice sheet at nearly the same time. Thus a large number of measurements must be made if results are to be significant.

These factors favor a shore-based station over an icebreaker expedition as a source of data. Icebreakers inevitably have many varied duties and cannot remain long in one location. A shore station permits detailed study of the same ice sheet throughout the winter. The Shippagan station offers a situation for the study of annual unrafted sea ice under conditions about as simple as can be found. It is beside a small, enclosed bay connected to the Baie des Chaleurs and hence to the Gulf of St. Lawrence. Tides are small (about 5 feet on the average), and there is practically no fresh-water runoff from land to reduce the salinity of the sea water, as the bay is essentially on the end of a peninsula with drainage going elsewhere. Much of the shore line consists of a peat bog which absorbs rainfall and also reduces runoff into the bay. There is a fresh-water pond nearby, which made possible an interesting comparison of fresh-water ice and sea ice having the same climatic history.

Sea water normally has a salinity in the range 34-35‰ (parts per thousand) and freezes at about  $-1.9^{\circ}\text{C}$ . Water with a salinity of over 24.7‰ has its maximum density at the freezing point, so that in shallow water the whole mass cools to the freezing point before any ice forms on the top surface. Fresh water, in contrast, has its maximum density at  $4^{\circ}\text{C}$  and this inversion effect results in an ice cover forming soon after the water in a lake has cooled to this temperature. Ice is a relatively good heat insulator so that in all but very shallow lakes the bulk of the water remains at  $4^{\circ}\text{C}$  throughout the winter.

Salt and air do not fit into an ice crystal. Hence, when salt water freezes the salt is rejected, some of it being trapped as brine between ice crystals. This brine forms layers between plates of pure ice and as freezing progresses the layers of brine break up into brine cells or pockets. Similarly, when the water freezes the dissolved air comes out of solution forming bubbles in the ice. It appears that the physical properties of sea ice are largely determined by the amount of entrapped brine and air. The salinity of sea ice depends on the rate of freezing, being initially about 5 to 10‰ in the surface layer and decreasing with depth, because the slower rate of freezing gives the brine more opportunity of escaping from between the forming crystals. The brine pockets are rarely in stable equilibrium with the surrounding ice. For equilibrium to exist the freezing point of the brine must be exactly equal to the temperature of the ice. If the ice cools some water freezes out of the brine, decreasing the size of the cell and increasing its concentration up to the equilibrium value. If the ice warms the brine will dissolve some ice. This increases the volume of the cell and also often leads to brine cells becoming interconnected along vertical lines. The brine being saltier and heavier than sea water tends to drain downwards through the ice. In the spring sea ice thus becomes less saline and more permeable.

Even in the absence of any temperature change in the ice as a whole, there is a tendency for brine cells to migrate downward because of the temperature gradient in the ice sheet. Consider a brine cell in the form of a vertical cylinder. The concentration may be correct for perfect equilibrium with the average temperature of the ice walls, but at the bottom of the cell it is slightly warmer and the brine will dissolve some of the ice whereas at the top the ice is colder and water will freeze out of the brine, the net effect being a slow downward movement of the cell with little net change in volume. An interesting experiment of Whitman (1926) illustrates this effect. He froze water containing 33% sodium chloride at an ambient temperature of  $-80^{\circ}\text{C}$ , and showed that with this rapid freezing the salinity of the ice is uniform and equal to that of the original solution. Next he took a cylinder of this ice a few inches long, lagged the sides of it, and mounted it vertically with its lower end immersed in a freezing mixture at  $-20^{\circ}\text{C}$ . The top end of the bar was held at about  $-2^{\circ}\text{C}$ . In 6 hours the salinity profile had changed to about 30% higher salinity at the warmer end of the cylinder than at the colder end, showing that the brine cells will migrate along the temperature gradient even against the attraction of gravity. Whitman found also, as expected, that no migration occurs, for any gradient, if the warmest part of the ice is below the eutectic temperature of the mixture.

## 2. ENVIRONMENT DURING TESTS

### (a) Oceanography

In front of the Shippegan field station the bay is approximately  $\frac{1}{2}$  mile wide. The bottom shelves off very gradually from the shore line to a channel about midway across, the channel being approximately 100 yards wide and 11 feet deep at low tide. The ice studied was cut from this channel. Tidal currents under the channel ice were measured and sometimes reached 3 knots. The flushing action of this current prevents fresh water from accumulating on the underside of the ice. The salinity and temperature of the water in the channel are given in Table I. The salinity was measured with a hydrometer.

TABLE I  
Salinity and temperature of Shippegan sea water

Time	Near bottom		Just under ice	
	<i>S, %</i>	<i>T, <math>^{\circ}\text{C}</math></i>	<i>S, %</i>	<i>T, <math>^{\circ}\text{C}</math></i>
Dec. 11, 1956	—	—	35.5	—
1100 Feb. 23, 1957 (High tide at 1122)	33.4	—	34.0	-1.7
1600 Mar. 18, 1957 (High tide at 1744)	30.0	—	31.2	-1.7
1620 Apr. 13, 1957 (High tide at 1506)	30.1	-0.9	30.4	-0.8

The slightly lower values recorded towards spring were probably caused by melting of the ice. The times quoted for high tides refer to Shippegan Harbour—the tidal crest reaches the field station somewhat later.

The raising and lowering of the ice cover with the tides (4-ft neap tides and 6-ft springs) causes tide cracks. In February 1957, there were eight of these cracks, running parallel to shore and about equally spaced over the first 150 feet from the shore line.

(b) *Meteorology and Ice Thickness*

In January 1957 a gas thermometer was installed in a Stevenson screen outside the station, and connected to a recorder inside the building. As this continuous record of air temperature is only available from Jan. 18 on, temperature and other meteorological data for the entire winter were obtained from the Department of Transport Meteorological officer at the R.C.A.F. station at Chatham, N.B. Chatham is 57 miles southwest of Shippagan. The weather data for Chatham are shown in Fig. 1. A comparison was made of the 0130 and 1330 Chatham temperatures with those recorded at Shippagan at the same times, and it was found that the average Chatham temperature was 1.9 centigrade degrees warmer.

In a simple case, the thickness of the ice cover should be proportional to the square root of the exposure to freezing temperature, neglecting radiation effects. The exposure is usually measured in degree-days or degree-months, referred to the freezing point of the sea water ( $28.7^{\circ}\text{F}$  or  $-1.9^{\circ}\text{C}$ ). On the average, the upward heat flux per unit area through the ice is

$$k \frac{\theta}{h} dt$$

where  $k$  is the thermal conductivity,  $\theta$  is the temperature difference between the top and bottom of the ice,  $h$  is the ice thickness, and  $t$  is the time. The albedo of snow-covered ice is sufficiently high that radiation effects are small and can be ignored in this calculation. Hence, the heat flux can be equated to the release of latent heat  $L$  in forming ice. That is,

$$k \frac{\theta}{h} dt = L d dh$$

where  $d$  is the density. Integrating this equation gives

$$(1) \quad h^2 = \frac{2k}{Ld} \int \theta dt,$$

which proves the result stated above, since the integral on the right of the equation is the exposure. The derivation is oversimplified since  $k$  is treated as a constant whereas it actually varies considerably with depth in an ice sheet, because of changing crystal size and brine content. Also the insulating effect of the snow cover is ignored. Nevertheless, this equation applied surprisingly well to our data, as is illustrated in Fig. 2. In this figure the exposure is calculated from the Chatham air temperatures, ignoring the small temperature differential between Chatham and Shippagan, and also assuming that the average wind speed of some 10 miles per hour would mix the air thoroughly enough that the surface temperature of the ice would equal the air temperature. It is interesting that the thickness and the square root of

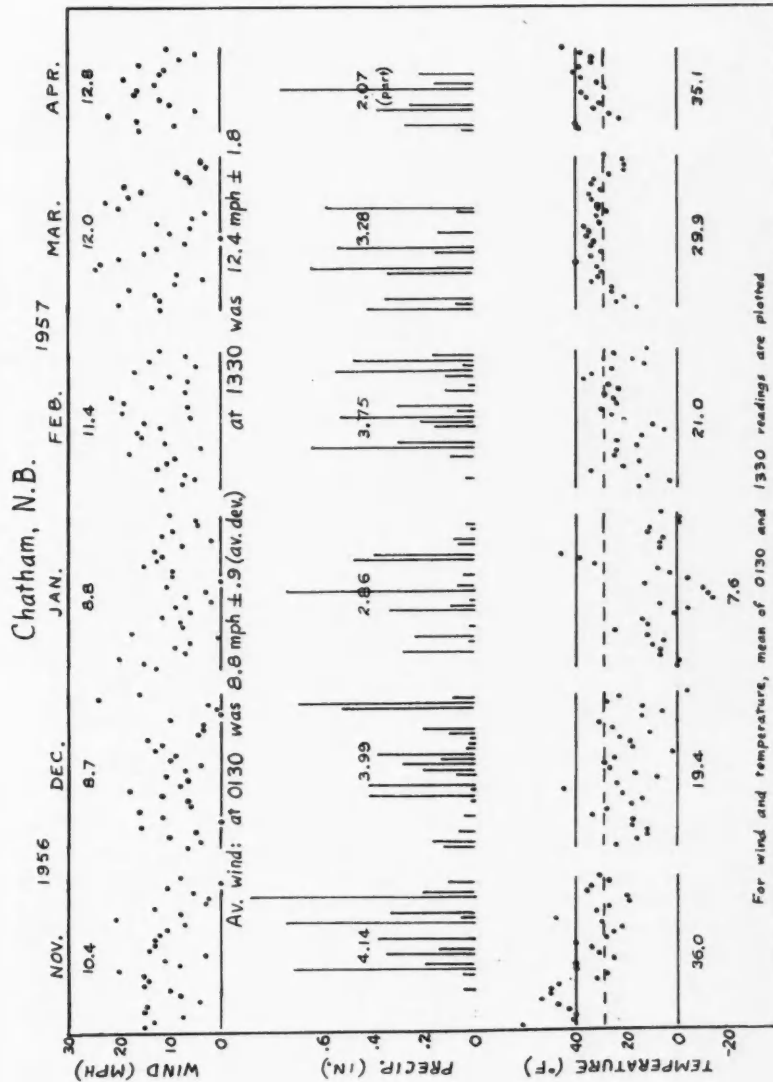


FIG. 1. Weather at R.C.A.F. Station Chatham, N.B., Winter of 1956-57.

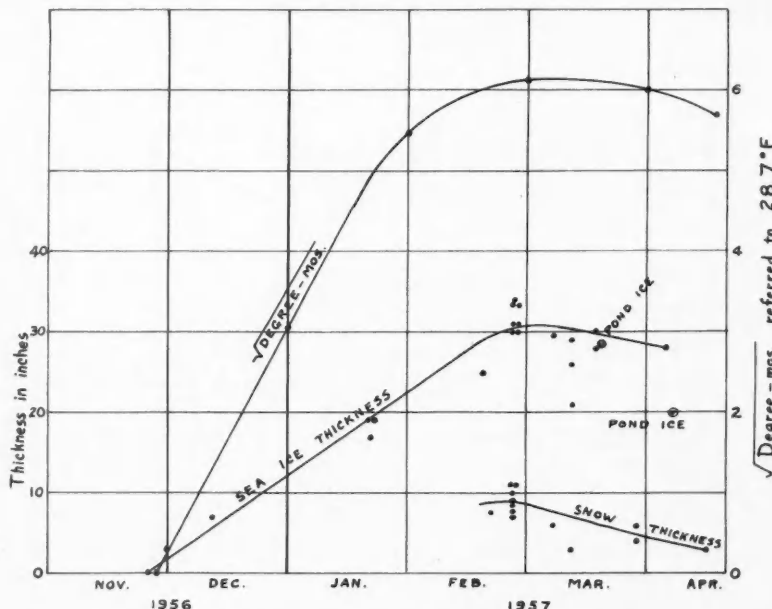


FIG. 2. Ice and snow thickness at Shippegan, N.B., and degree-months at Chatham, N.B.

the exposure both happen to be approximately linear with time. It is evidently an experimental error that the freeze-up is shown as beginning before the freezing exposure started to accumulate—the date of freeze-up was provided from memory by the officer-in-charge of the biological station.

Using the data of about Jan. 20, equation (1) can be solved for  $k$ , as follows:

$$k = (19 \times 2.54)^2 \times 80 \times 0.9 / \{2 \times (5/9) \times 25 \times 30 \times 24 \times 60 \times 60\} \\ = 0.0024 \text{ c.g.s. units.}$$

This result is an average conductivity of the ice and its snow cover, but may be compared with the results found by Malmgren (1927) on the "Maud" expedition in 1922-25 of 0.0015 near the surface, 0.004 at a depth of 0.5 meter, and 0.005 below 1 meter (all in c.g.s. units).

Assur (1956) gives empirical formulae for the growth and decay of ice, as follows:

$$(2) \quad h \text{ (in inches)} = 1.06 \alpha \sqrt{S}$$

$$(3) \quad \Delta h \text{ (in inches)} = S_{10} / 30$$

where  $h$  is the thickness of the ice,  $\Delta h$  is the reduction in thickness,  $S$  is the freezing exposure in Fahrenheit degree-days below  $32^{\circ}\text{F}$ ,  $\alpha$  is an empirical coefficient dependent on snow cover, and  $S_{10}$  is the "warming" exposure in degree-days above  $10^{\circ}\text{F}$ . Applying (2) to the present case of ice growth

from Nov. 28 to Jan. 20 (54 days),  $S = 25$  degree-months (referred to  $28.7^\circ$  F) or, correcting  $S$  to  $32^\circ$  F,  $S = 25 \times 30 + 54 \times 3.3 = 928$  degree-days. For  $\alpha$ , Assur quotes values of 0.70 to 0.75 for Arctic sea ice. Therefore, from (2)

$$h = 1.06 \times 0.72 \times \sqrt{928} = 23.3 \text{ in.}$$

compared with the 19 in. actually observed. The difference presumably results from the much heavier snowfall at Shippegan (see Figs. 1, 2, and 3) than in the Arctic.



FIG. 3. Deep snow along the road to the Shippegan field station in April. Snow fall is much greater than in the Arctic.

Equation (3) is based on Assur's observation that, in the Arctic at least, as soon as the mean daily temperature exceeded  $10^\circ$  F the ice started to decrease in thickness and strength. This observation is certainly not valid in the present case. Only in January was the monthly mean temperature below  $10^\circ$  F. The mean in February was  $21^\circ$  F yet the ice did not start to decrease in thickness until about the beginning of March, at which time the mean daily temperature had reached about  $27^\circ$  F, virtually the freezing point of sea water.

Both the top and bottom surfaces of an ice cover are usually irregular so that the thickness varies from point to point. A survey was made on Feb. 25 by drilling eight holes with a core drill at points on a rectangular grid with a spacing of 3 feet. Results are plotted in perspective in Fig. 4, showing snow depth, ice thickness, and elevation of the ice surface with respect to sea

level. The average ice thickness was  $32.9 \pm 1.9$  in. (average deviation) and the average snow thickness was  $9.1 \pm 1.3$  in. The average height of the boundary between the ice and snow was  $0.28 \pm 0.93$  in. above sea level.

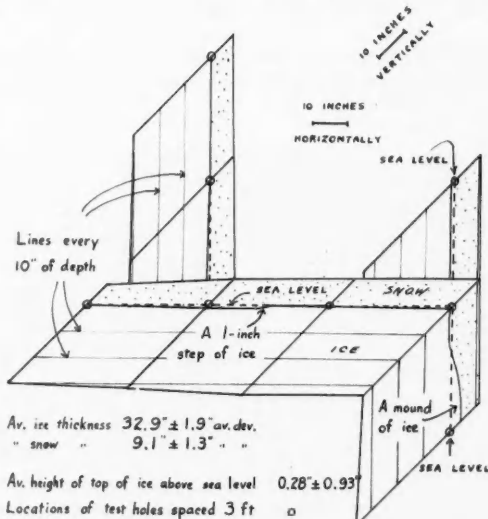


FIG. 4. Perspective sketch of spatial variation of ice and snow thickness on Feb. 25.

New sea ice was found from sample blocks to be very smooth on the underside in early winter, with a slight fine-grained roughness superimposed on

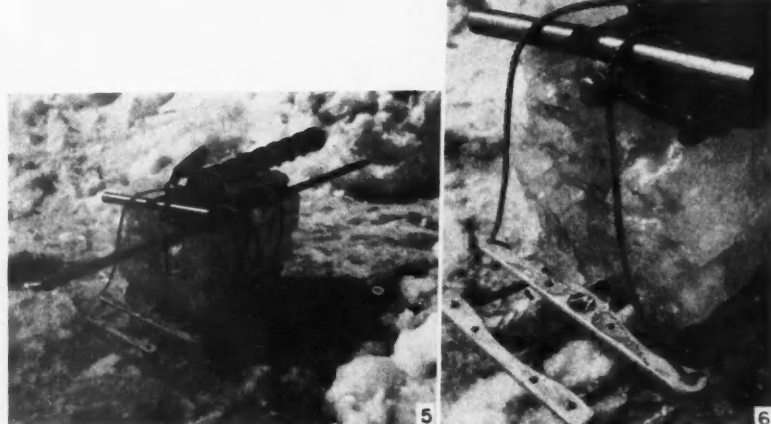


FIG. 5. Sea ice block A 1511. Note strongly convoluted bottom caused by melting by sea water.

FIG. 6. Close-up of block A 1511.

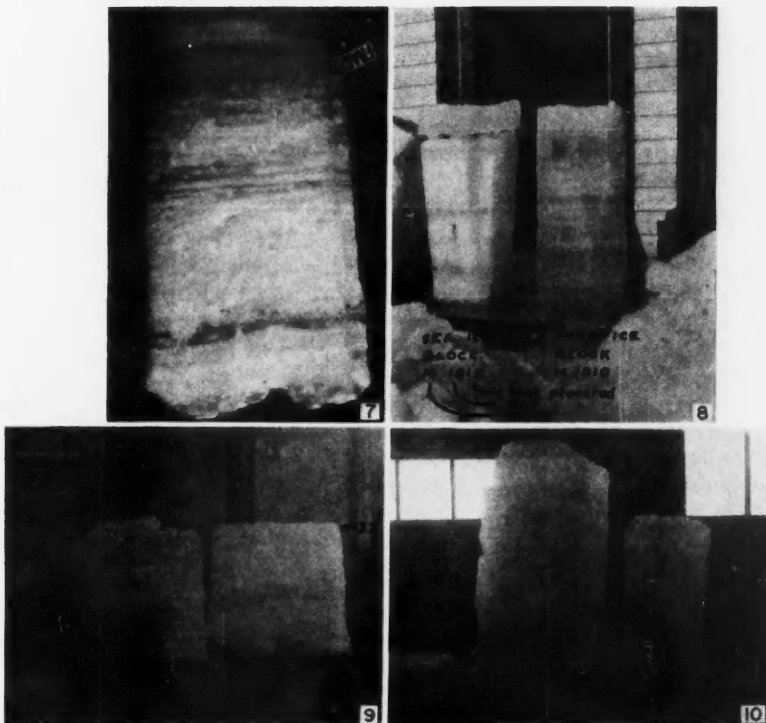


FIG. 7. A vertical section of block A 1511. There is 28 in. of ice plus 2 or 3 in. of corn snow on top.

FIG. 8. Sea ice is milkier than fresh-water ice. The top 6 in. of the sea-ice block is probably refrozen snow. Block M 1815 is 30 in. high including the 6 in. of snow ice.

FIG. 9. The block of Fig. 7 cut in half.

FIG. 10. In April, the pond ice had melted to three-quarters of the thickness of the sea ice.

long-wave gentle undulations. In spring, the fine-grained roughness disappeared and the long-wave undulations increased in amplitude and decreased in wavelength. The convoluted bottom of the block of sea ice cut in April is shown in Figs. 5, 6, 7, and 9, and the smooth bottom of a block cut at about the same date from a fresh-water pond is shown in Fig. 8. Approximate values of the irregularities in the bottoms of various sea-ice blocks are shown in Table II. In this table and elsewhere, the blocks are described by a code showing the time the block was cut from the ice cover. The letter gives the month, the first two figures the date, and the second two the hour of the day. Thus block A 1511 was cut on Apr. 15 at 1100 hours.

Fresh-water blocks cut in March and April differed greatly in appearance from the sea-ice blocks. Not only were the surfaces flat and glassy, but the pond ice was clear and transparent except for occasional horizontal planes and vertical lines of air bubbles. The sea ice was almost always quite milky,

TABLE II  
Bottom roughness of the sea ice

Block	Fine-grain undulations		Coarse undulations	
	Amplitude, cm	Wavelength, cm	Amplitude, cm	Wavelength, cm
F 2311	0.02	0.3	0.6	30
M 1815	Negligible	Negligible	0.8	20
A 1511	Negligible	Negligible	4	15

except for an occasional clear layer. Both pond and sea ice show definite layering in this typically land climate with its large fluctuations in temperature.

Figure 8 shows the sea- and pond-ice samples for Mar. 18 and 19; both are of about the same thickness and the extra clarity of the pond ice is evident. The mitten gives a scale indication. The top 4- or 5-in. section of each block is composed of snow ice, that is, melted and refrozen snow or, in the case of sea ice, snow which has been flooded with sea water and frozen. Figure 10 shows the sea-ice and pond-ice samples cut in April. The pond ice has shrunk to less than three-quarters of the sea-ice thickness, possibly because of the greater heat storage in fresh water which results from the inversion temperature effect discussed in the Introduction.

(c) *Micrometeorology*

In order to get a preliminary idea of the stability of the air and of the convective heat flux, the wind profile up to head height was taken on Feb. 26 and Mar. 18 with a hand-held, eight-blade anemometer (4-in. Biram). In addition, on Mar. 18, the relative temperature profile was taken with a Beckman differential thermometer shielded from direct sunlight. Both wind-speed profiles were definitely logarithmic rather than linear, indicating turbulence. The data of Feb. 26 is plotted in Fig. 11 on semilogarithmic paper, with a line of best fit assuming a law of the form  $v = a(\log h - \log h_0)$ , where  $v$  is the wind speed and  $h$  the height. The height for zero speed  $h_0$  is seen to be about 0.1 cm. This height  $h_0$  is a measure of surface roughness, and according to Byers (1937) is usually about 1/30 of the average height of the roughness elements. As the wind had come across snow-covered sea ice with undulations of vertical height of about 5 cm, the value of  $h_0$  is of the right order of magnitude. The scatter of the wind-speed data taken on Mar. 18 was even greater than that shown in Fig. 11.

It had been hoped to use the wind and temperature profile measurements of Mar. 18 to calculate the Richardson number  $R_i$ , and the convective heat flux using the equation of Thornthwaite, Halstead *et al.* (1954). Haurwitz (1941) states that the air is unstable when  $R_i$  is less than 1/3. Unfortunately the scatter of the wind-speed measurements made the calculations pointless. Analysis of the temperature changes with time at various heights is of some interest. The temperature was observed over a period of about 10 minutes each at heights of 5, 10, 20, 50, and 175 cm above the snow surface. At each height, it fluctuated with time, and the maximum and minimum values and

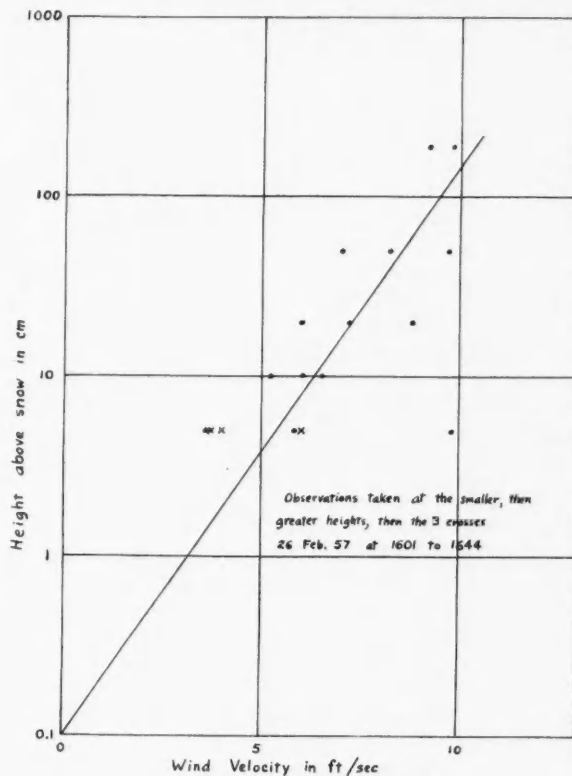


FIG. 11. Wind profile on Feb. 26.

the times of these values were recorded. The results are shown on the left-hand side of Fig. 12. Note that the eddies are slower and involve a greater change of temperature at 20 cm than at other heights. This is brought out more clearly on the right-hand side of the figure, where the average absolute value of the temperature changes and the average time interval between maximum and minimum temperatures are plotted as functions of height. General weather conditions are noted on the figure.

These results suggest that the 20-cm level is possibly about the center of the mixing region between the relatively stagnant (streamline flow) air immediately above the snow and the upper air. However, the period of the temperature oscillation (of the order of 15 minutes at the 20-cm level) when combined with the wind speed of 10 m.p.h. gives a distance of perhaps 2 or 3 miles between eddy centers. On this scale, a maximum mixing zone only 20 cm above the surface seems improbable. Furthermore, DeLand and Panofsky (1957) found that low-frequency turbulence keeps increasing with height even up to 91 meters.

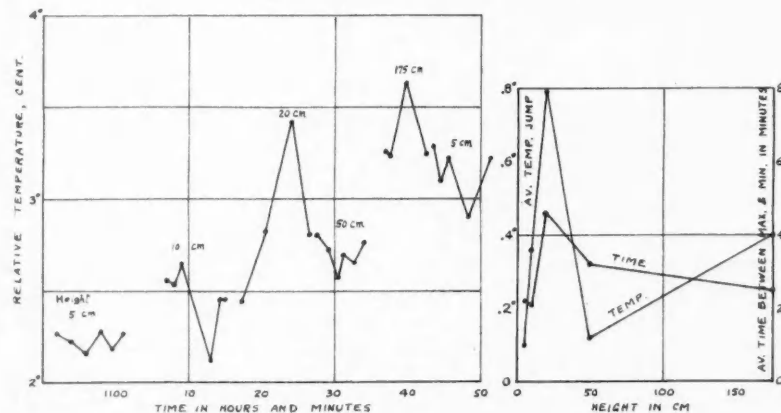


FIG. 12. Temperature profile in air vs. time. Temperature profile by Beckman differential thermometer showing turbulence over snow at ice station on Mar. 18, 1957, at 1050 to 1150; temperature about  $+1^{\circ}\text{C}$ ; 3/4 cloudy; wind about 10 W at head height.

(d) *Radiant Flux*

The solar constant is the total radiation from the sun incident normally on the top of the atmosphere. Its value is  $1.92 \text{ cal cm}^{-2} \text{ min}^{-1}$ . All radiation flux values will be quoted in these units. The flux at the Shippagan field station is, of course, less than the solar constant because of atmospheric absorption and inclined incidence. No systematic radiation observations were made, but a few spot checks were taken with a Gier and Dunkle (1951) radiometer made by Beckman and Whitley (model No. H188). This instrument measures the total radiation incident from a complete hemisphere. In its normal attitude, with the sensing element pointing upward, it reads the incoming flux, but by inverting the instrument the outward flux from the earth can be measured and the net flux can be found from the difference. The results are given in Table III. One other observation is that at noon on Mar. 16

TABLE III  
Radiation flux values

Date	Time	Air temp., $^{\circ}\text{C}$	Radiation flux ( $\text{cal cm}^{-2} \text{ min}^{-1}$ )			Weather
			Incoming	Outgoing	Net	
Jan. 22	1650	3.3	0.52	—	—	Cloudy, slight rain
Mar. 16	1130	0	1.05	—	—	Slight haze
	1200	0	1.31	1.10	0.21	Clear
	1800	1	0.43	0.46	-0.03	Very thin stratus over sun
Mar. 20	1115	2	1.07	0.83	0.24	10/10 stratus
	1320	3	1.18	1.01	0.17	Clear but hazy
	1720	0	0.48	0.45	0.03	Very thin stratus over sun
Apr. 13	1420	5	1.06	0.80	0.26	Light haze, 3/10 cloud
	1725	3	0.59	0.55	0.04	Hazy, 5/10 cloud
Apr. 16	1125	-3	1.41	1.03	0.38	Clear
	1750	+2	0.55	0.52	0.03	Light haze, 2/10 cloud

the incoming flux was 1.31 as shown; when the radiometer was shielded from direct sunlight the reading dropped to 0.65, that is, about half the radiation was coming from the sky.

(e) *Conductive Heat Flux*

The relative thermal conductivities of the snow cover and of the sea ice were measured roughly by inserting toluol thermometers horizontally at the snow-ice boundary (position A), and 1 inch under the snow surface (position B). The snow cover was 12.2 in. thick, giving the distance AB as 11.2 inches. Ice thickness was 33 in. and the temperature of the lower surface of the ice can be taken to be the same as that of the water immediately below the ice, namely  $-1.7^{\circ}\text{C}$  from Table I. Results are shown in Table IV. The ratio of the thermal conductivity of the ice to that of the snow is shown as  $R$ , and is calculated assuming that upward heat fluxes through the ice and snow are equal and that the radiation incident on the thermometers has a negligible effect. The average value of  $R$  is seen to be  $6.0 \pm 1.4$  (average deviation). The snow cover was too thin later in the spring to make useful measurements of this type as the increased solar radiation melted the snow around the thermometers.

TABLE IV  
Temperature profile in snow and ice, and relative thermal conductivities

Time	Feb. 25, 1520	Feb. 25, 1805	Feb. 26, 1150
Air temperature $\theta$ , $0^{\circ}\text{C}$	-10.0	-10.5	-7.5
$\Delta\theta/\Delta t$	Dropping	Dropping	Rising
Weather	Cloudy	Cloudy, snowing	Cloudy, snowing
Wind velocity, m.p.h.	—	E 15	E 10
Temperature at A, $^{\circ}\text{C}$	-4.3	-4.1	-4.0
Temperature at B, $^{\circ}\text{C}$	-8.9	-10.6	-7.7
$R$	5.2	8.0	4.7

The values of  $R$  agree with the range of 4.7 to 6.1 given by Assur (1956) for "hard-packed snowdrifts in the Arctic", but this snow is more reasonably classed as "old snow" or "normal snow cover" for which he quotes values, respectively, of 8.3 to 12.0 and 12 to 19. The snow measured appears to have a greater thermal conductivity than Arctic snow, possibly because of the frequent thawing periods resulting in a greater ice content in the snow in New Brunswick.

A direct measurement of the heat flux in the ice is difficult because of the variability of its thermal conductivity. It had been planned to bury in the ice a horizontal slab of slate (painted white to minimize absorption of radiation), with thermistors on opposite faces of the slab. The thermal conductivity of the slate could be measured accurately and is sufficiently close to that of sea ice so as not to disturb the heat flow appreciably. An asbestos shingle was actually used instead of the slate, and no results were obtained because of failure of the insulation on the thermistor leads. As a makeshift a 1-in. wood board was placed against the ice and under the snow, with thermometers above and below the board. The thermal conductivity of the wood was

assumed to be  $3.6 \times 10^{-4}$  c.g.s. units (handbook figure for Virginia pine). The measurements certainly give only the order of magnitude of the flux. Using units of calories  $\text{cm}^{-2} \text{min}^{-1}$ , on Feb. 26 at 1500 and 1700 hours the flux was 0.03 upward. It was cloudy, with an air temperature of  $-6$  to  $-7^\circ \text{C}$ . During the period Apr. 13 to 16, values from 0.01 upward to 0.06 downward were observed, depending on the time of day. These days were clear, with temperatures of  $+2$  to  $+4^\circ \text{C}$  and light winds. The results are not inconsistent with those obtained by Malmgren (1927).

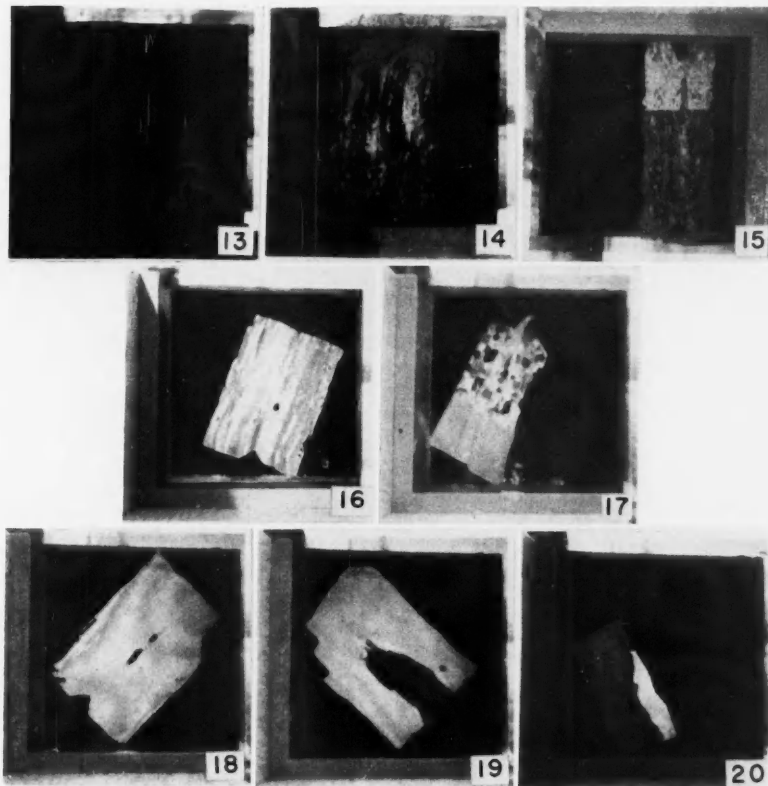
### 3. PHYSICAL PROPERTIES

#### (a) *Crystal Structure*

The crystal structure of the sea ice was investigated by cutting sections about  $\frac{1}{4}$  in. thick from the big blocks, using a pruning saw. These sections were melted down to about  $\frac{1}{16}$  in. thickness on a metal plate in a heated room. The thin sections were observed in a cold, 6-in. by 6-in., simple polariscope. In general, the upper portion of the ice sheet showed little structure, consisting of small, irregular crystals approximately equidimensional and not more than  $\frac{1}{2}$  in. across. At some (variable) depth, there was a very sharp transition to long, vertical crystals 4 to 16 in. long and about  $\frac{1}{4}$  to  $\frac{1}{2}$  in. across. This transition was 20 inches below the snow-ice interface in the Feb. 23 block (total ice thickness of 29 in.), at a depth of 10.5 in. in the Mar. 18 block (24 in. thick), and at 20.5 in. in the Apr. 15 block (28 in. thick). The variation in depth of the transition layer is puzzling. The sequence of the three observations suggests that recrystallization is an improbable explanation. The blocks were cut from locations up to 50 feet from each other, so that local variations in ice thickness and variations in the thickness of snow cover and in the thickness of the snow ice may have had something to do with the time at which the transition layer froze. The second author observed similar transition layer phenomena when working on ice in the Bering Sea in 1954-55. Additional work is certainly needed on the crystal structure of sea ice.

Figure 13 shows vertical and horizontal sections in the February block, at 25 to 29 inches below the surface and, therefore, below the transition layer. The vertical section shows the long crystals. The Polaroid plates are 6×6 in. Figure 14 shows the transition to long crystals at a depth of 20 in.; this and the following photographs of crystals are of vertical sections. Figure 15 shows the transition layer at 10.5 in. in the March block. Figure 16 is of another section at a depth of 25 to 29 in. in the February block; by way of contrast Fig. 22 (taken at 8 to 13 in. in the April block) shows the small, roughly equidimensional crystals.

For the pond ice, Fig. 17 shows what are probably crystals of snow ice in the first 3 inches below the ice surface, with the long vertical crystals of fresh-water ice below. In the pond ice, these seemed to have lengths of many inches, possibly even of feet. Figures 18 to 20 show parts of sometimes one and sometimes two crystals at other depths of this pond ice. Note the interference fringes in Fig. 18 caused by slight variations in the thickness of the



FIGS. 13-20. Vertical (in general) sections of ice 1/32 in. to 1/16 in. thick, cut from various sample blocks and placed in a 6 in.  $\times$  6 in. polariscope for crystal examination. The shade of gray (of color, originally) is determined by the direction of the optic axis. The light source was a 60-watt bulb behind a diffusing screen. Exposures were usually 1 second at f/5.6 with Panatomic X film.

FIG. 13. Sections at depths of 25 to 29 in. in sea-ice block F 2311. Vertical section (left) and horizontal section (right). Note long, vertical crystals.

FIG. 14. Section at 18 to 25 in. in block F 2311. Note sharp transition from small, equidimensional crystals to long, vertical ones at 20 in.

FIG. 15. Section at 8.5 to 14.5 in. in block M 1815. Transition is at 10.5 in. here.

FIG. 16. Section at 25 to 29 in. in block F 2311. Long crystals evident.

FIG. 17. Section at 0 to 5 in. in fresh-water block M 1910. Upper 3 in. is probably snow ice. Below this, note the long, vertical crystals typical of lake ice; actually lower part here is a single crystal.

FIG. 18. Section at 5 to 10 in. in block M 1910. The single crystal shows interference fringes owing to slight variations in the thickness of the section.

FIG. 19. Section at 15 to 20 in. in block M 1910. Parts of two crystals.

FIG. 20. Section at 20 to 24 in. in block M 1910. Parts of two crystals.

PLATE II



FIG. 21. Iceberg crystals measured for  $P^2/A$  ratio.  
FIG. 22. Sea-ice crystals measured for  $P^2/A$  ratio.

section. Visually, or in color photographs, each crystal has its own color which depends on the thickness of the section and the direction of the optic axis of the crystal.

(b) *Crystal Shape and the Age of Ice*

The problem of the determination of the age of ice, in the polar regions and in ice fields and glaciers, is yet to be solved. As the properties of an ice sheet change with age it is of more than theoretical interest to develop a reasonably precise method of dating ice. The best present estimate of the average age of the Arctic pack ice is 9 years, but this is only an estimate and the range of age involved must be great. A method which seemed to the authors to show great promise was tritium dating. Tritium is formed by cosmic ray interactions with constituents of the upper atmosphere and falls to the surface in the form of heavy water containing one or more tritium atoms. Since the source is in the upper air, the tritium content in a piece of ice should decay with the half-life of tritium, 12.4 years. Thus, if the tritium content of the water from which the ice was formed were known, a determination of the tritium level would serve to measure the age of the ice. Tritium determinations are difficult since the normal hydrogen-tritium ratio in water is of the order of  $10^{17}$ , but Brown and Grummit (1956) describe a technique developed at Atomic Energy of Canada, Ltd., for measurements using 1 liter of water or less.

Unfortunately, the level of tritium in the atmosphere has fluctuated considerably in recent years because of the hydrogen bomb tests, which release considerable amounts of this isotope. The process of transfer of the tritium from the atmosphere to the seas is complex and leads to different tritium concentrations in different parts of the world. A number of measurements have been made in temperate latitudes by the Lamont Geological Laboratory of Columbia University but little was known about Arctic waters. With a view to establishing a baseline, the authors suggested to the Atlantic Oceanographic Group, St. Andrews, N.B., that samples be collected at a variety of locations and depths on the 1957 Arctic cruise of H.M.C.S. *Labrador*. These samples were collected by Dr. N. J. Campbell and have been analyzed by Brown and Grummit (1958). Details will be published by the latter, but from the results it is apparent that tritium dating is of little use in finding the age of ice at present. Concentrations found varied so much from point to point in the Arctic, and also with depth, that an average value to serve as a baseline would be meaningless. The method should be borne in mind, however, for the future, if weapons testing ceases and the tritium levels in the atmosphere and oceans become stabilized.

Another age-dependent factor is the shape of ice crystals. It is well known that recrystallization takes place in ice, with larger crystals growing at the expense of smaller ones. The rate of this process is strongly influenced by temperature, recrystallization being much more rapid near the freezing point. The crystals in sea ice are usually elongated vertically. If a (preferably) horizontal section is taken, older crystals appear to be more rounded than

the crystals in new ice. A convenient dimensionless ratio to measure this effect is the ratio of perimeter squared to area ( $P^2/A$ ). This might be called jaggedness. Its numerical value should decrease with age, tending to the limit  $4\pi$  for crystals of circular cross section. Since this parameter integrates the effect of both time and temperature regime, its reciprocal might well be defined as the thermal age of the ice in question.

A few measurements were made on ice crystals of varying origin. The perimeter was measured with a string and the area calculated from the measured sides of a rectangle estimated to be of equal area. In 1956, a sample was obtained from an iceberg in Hudson Strait. Its age is unknown but obviously the ice was very much older than sea ice. For six crystals,  $P^2/A$  was  $21 \pm 18\%$  (average deviation) (see Fig. 21). The same summer, a sample of annual sea ice taken off East Baffin Island gave a result of  $46 \pm 6\%$ . This figure is probably too large, as a *vertical* section was used and horizontal sections would be more representative, as discussed above. Figure 22 shows a section obtained at Shippegan in April 1957. Again it is a vertical section but this does not matter here as measurements were made in the upper part of the ice sheet when the crystals were approximately equidimensional. Measurements of three crystals gave  $P^2/A = 28 \pm 7\%$ . These values are not numerous enough to be statistically significant, but they do seem to indicate a correlation.

### (c) Specific Gravity

The specific gravities of ice samples were measured by weighing pieces of about 200 to 300 g in air on a precision spring balance (to  $\pm 1$  g), and then finding the loss of weight in fresh water (at  $0^\circ\text{C}$  to  $10^\circ\text{C}$  where the density of the water differs little from its maximum density). Results are shown in Fig. 23. Note that the specific gravity decreased in general with depth (except for the break in the curve for the April block at a depth of 11 in. where there was a very bubbly layer). Also the specific gravity appeared to increase towards spring. The pond ice in March had a higher specific gravity than all the sea-ice samples except one. All values measured, for both pond ice and sea ice, were below that of pure ice, namely 0.917. The values obtained can only be considered as relative, since the blocks had all drained on their sides for at least 1 day, in an unheated shed at temperatures between  $-6^\circ\text{C}$  in February and  $+6^\circ\text{C}$  in April, before the measurements were made. This storage period is a grave disadvantage of attempting to perform a number of tests on a single large block. A technique based on obtaining small samples quickly (with a core drill designed at S.I.P.R.E.—the Snow, Ice, and Permafrost Research Establishment, U.S. Army Corps of Engineers, Wilmette, Ill.) and making measurements immediately should give better results in future.

Because of this drainage, the values are much less than those obtained by Malmgren, namely 0.914 to 0.924 for new ice, unexposed to the sun and undrained, 0.857 for the top of ice which had lasted through a summer (the measurement was made the following winter at a temperature of  $-27^\circ\text{C}$ ), and 0.885 to 0.893 at  $-6.2^\circ\text{C}$  for old ice. Weeks (1957) at Hopedale, Labrador,

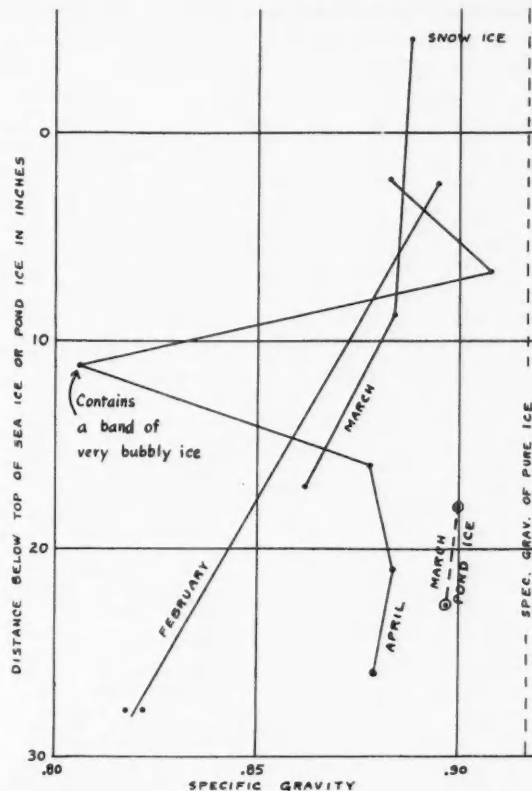


FIG. 23. Specific gravity profiles, after draining blocks on their sides for 1 day in an unheated shed.

obtained about 0.92 in February 1956 decreasing linearly to 0.88 in April then increasing to 0.90 in May, all values being for undrained ice and with a standard deviation of around 0.02.

On the 1956 icebreaker trip, the specific gravity of sea ice off Brevoort Island was 0.85 at 50 inches below the ice surface. In Foxe Channel, comparable figures were 0.88 at 50 inches and 0.85 at 5 inches. A sample of ice from an iceberg had a specific gravity of 0.88.

#### (d) Salinity

Salinities were found by melting ice samples and measuring the melt water at a known temperature with a hydrometer calibrated in salinity rather than specific gravity. Results are shown in Fig. 24. The shapes of the salinity profiles are probably reasonably accurate but the values are 1 to 2% low because of drainage. The effect of drainage is indicated by the dashed curves

which were measured on the underside of the block, into which brine was seeping from the upper layers. Kusonoki and Tabata (1954) have carried out measurements on the speed of draining of brine in sea ice which gave comparable results.

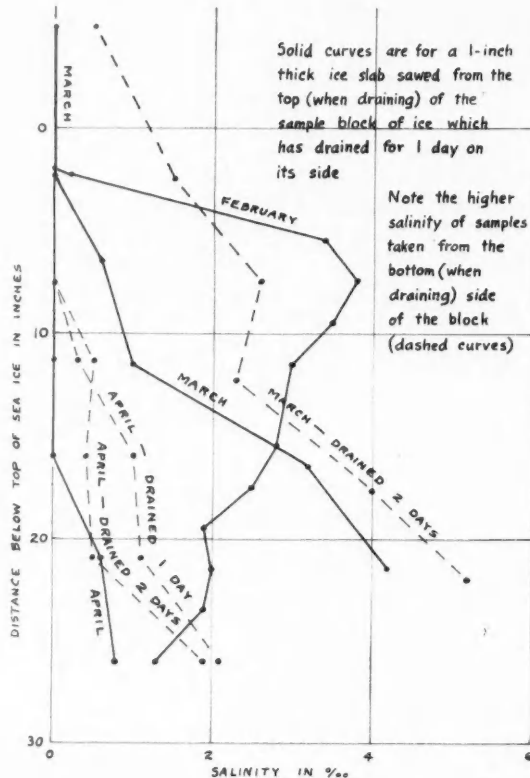


FIG. 24. Salinity profiles, after blocks were drained on their sides for 1 day in an unheated shed.

On the summer icebreaker trip salinities of annual sea-ice samples in the lower Arctic were measured. In three tests, made after draining the samples for 1 day in a freezer at  $0^{\circ}$  F, values of 0.6, 0.4, and  $0.1\%$  were found.

Malmgren obtained values of about 4 to  $8\%$  for new sea ice (undrained) with maxima near the top of the ice and also at the bottom. Weeks found salinities in the range 4 to  $20\%$  with similar maxima. He also found that salinities were lower in spring than in midwinter.

#### (e) Electrical Resistivity

For these tests a row of four, equally spaced, 12-in. nails were driven a

few inches into the ice. The distance between adjacent nails was varied from 10 centimeters up to 150 or 200 centimeters. The outer nails were used as current electrodes and the inner ones as potential terminals. The resistance was measured either by the voltmeter-ammeter method or using a low-resistance Megger with two ranges: inner scale 0-40 ohms, outer scale 0-200 ohms. The resistivity  $\rho$  for a half-infinite medium with point electrodes on the surface is  $2\pi lV/I$  or  $2\pi lR$ , where  $l$  is the spacing, and  $V$ ,  $I$ , and  $R$  are the voltage, current, and resistance, as usual. Use of this equation would be expected to give considerable variation in resistivity with spacing, since conduction is mainly through ice for small spacing and partly through the salt water under the ice for large spacing.

The results are shown in Fig. 25. The scatter is considerable but the resistivity increased as spring approached, as would be expected from the decreasing salinity of the ice. Also, in most cases the resistivity reached a maximum for a

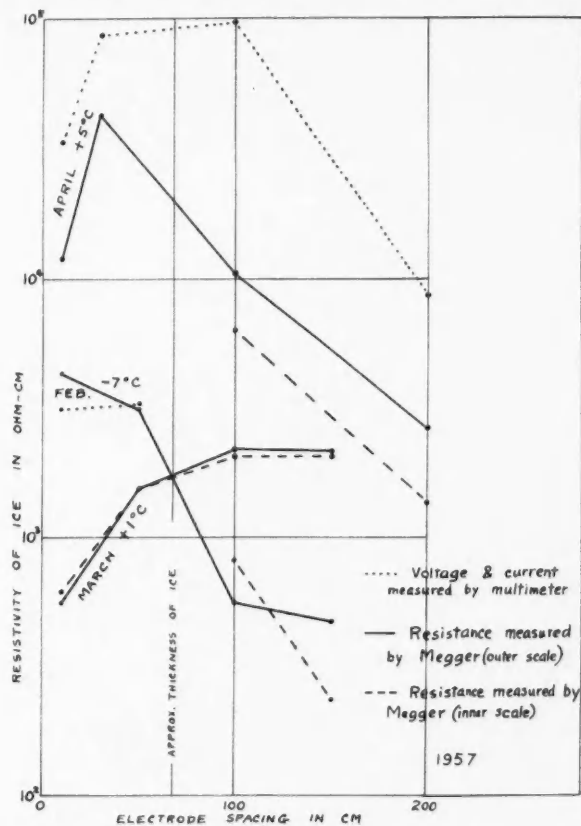


FIG. 25. Resistivity of annual sea ice in winter by the four-electrode method.

spacing of the order of magnitude of the ice thickness, then dropped off. For very large spacing it would be expected to approach the resistivity of sea water at the freezing point, about 40 ohm-cm. Between March and April the peak moved towards smaller spacing, indicating more resistive layers near the surface because of brine drainage downward. However, between February and March the opposite took place, which is hard to explain.

In summer, the resistivity of ice is very high because of the low salinity. For a 10-cm spacing it was measured as 0.4 megohm-cm near Baffin Island on July 16, 1956, and 3.0 megohm-cm in Foxe Channel on July 28. In both cases the daily range of temperatures was about  $+1^{\circ}$  to  $+5^{\circ}$  C. This high resistivity produces strong attenuation of radio signals and propagation is much poorer over sea ice than open water.

In late March 1955, Edward E. Howick of the U.S. Navy Electronics Laboratory obtained the variation of apparent resistivity with electrode spacing shown in Fig. 26 for an icefloe 1.2 miles across, 50 miles southwest of Nome, Alaska. This was annual ice which had not yet started to deteriorate. Note that the maximum apparent resistivity is for an electrode spacing of about half the ice thickness. The results for February and April on Fig. 25 are consistent with this result, although there are not enough points to warrant a general conclusion.

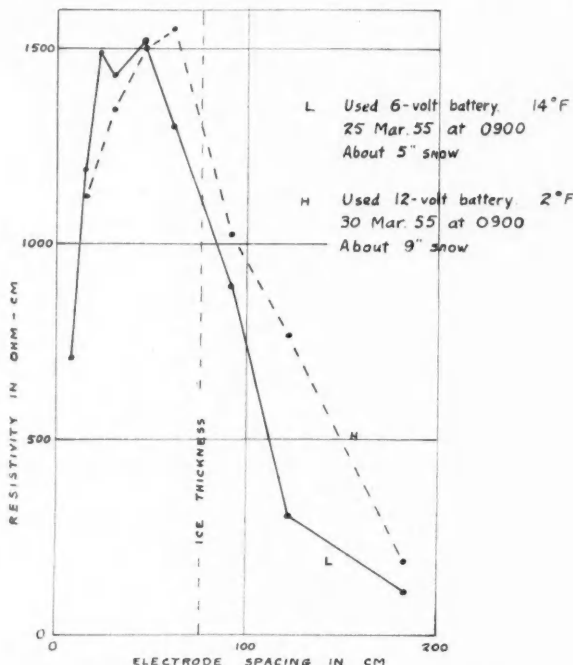


FIG. 26. Resistivity of annual ice in the Bering Sea in winter of 1955.

Dichtel and Lundquist (1949) found at Barrow, Alaska, in winter that the resistances of their  $2 \times 2 \times 8$ -in. samples were practically independent of the distance below the surface, in contrast with the above results. The temperatures were in the range  $-7^\circ \text{C}$  to  $-27^\circ \text{C}$ . At around  $-15^\circ \text{C}$ , the resistivity for horizontal samples was about 10 times that for vertical samples, and at  $-25^\circ$  this ratio dropped to 3. This is consistent with the fact that the brine pockets in sea ice, which supply most of the conductivity, are elongated vertically. These authors also found the resistivity of sea ice to be strongly temperature dependent. The variation is not exactly logarithmic, but their data can be represented roughly by equations of the form  $\rho = a \exp(-\theta/b)$ , where  $\rho$  is the resistivity, in ohm-cm,  $\theta$  is the temperature in  $^\circ \text{C}$ , and  $a$  and  $b$  are empirical coefficients. Approximate values are  $a = 5.9 \times 10^4$ ,  $b = 5.6$  for horizontal samples and  $a = 3.6 \times 10^2$ ,  $b = 3.9$  for vertical samples. At best, these equations would only apply to annual winter ice since the real independent variable is salinity, not temperature, and the salinity depends on the thermal history as well as the current temperature.

(f) *Permeability*

The permeability of ice  $C$  may be defined as the mass transport coefficient, that is the mass of fluid moving per unit time per unit area, divided by the pressure gradient. In symbols,

$$(4) \quad M = Vd = CA(dp/dh)t$$

where  $M$  is the mass of fluid of density  $d$  and volume  $V$  transported in time  $t$  through an area  $A$  by a pressure gradient  $dp/dh$  acting in the direction of the co-ordinate  $h$ , which is frequently the height. Permeability is considered by the authors to be an important parameter of ice since it is a measure both of the volume occupied by brine cells and air pockets and the degree of connection between these holes in the ice sheet.

The permeability can be calculated readily for two simple models which are of some interest. Consider a slab of ice of thickness  $h$  with a pressure difference  $p$  across it. Assume the slab to have  $n$  cylindrical holes, each of radius  $r$ , per unit area with their axes parallel to the pressure gradient. Then, from Poiseuille's equation for laminar flow in a tube,

$$(5) \quad V = \frac{\pi n p r^4 t A}{8 h \eta}$$

where  $\eta$  is the viscosity of the fluid. Comparing this equation with (4),

$$(6) \quad C = \frac{\pi n r^4 d}{8 \eta}.$$

For a second model, consider a slab of ice with a series of  $N$  slots, each of width  $2L$ , per unit length. The slots are taken parallel to the pressure gradient. The directions of the slots in the surface of the slab are accurately parallel in a single ice crystal, but the angles between the slot axes are random in adjacent crystals. Consider laminar flow through a slot. Take the  $X$ -axis perpendicular to the faces of the slot with the origin at the center. Then if

the fluid velocity is  $u$ ,  $u(x)$  is an even function of  $x$ ,  $u(L) = 0$ , and  $u(0) = v$ , say, the maximum velocity. Consider the forces acting on the fluid film bounded by the planes  $\pm x$ . The viscous drag per unit area is  $\eta(du/dx)$ , and if we take unit slot length in the surface, the total retarding force for both sides of the film is  $2\eta h(du/dx)$  and this must equal the force caused by the pressure gradient. That is,

$$-2\eta h \frac{du}{dx} = p \times 2x \times 1$$

$$px \, dx = -\eta h \, du.$$

Integrating,  $p x^2/2 = -\eta h u + \text{a constant of integration}$ . Since  $u(L) = 0$ ,  $u = (p/2\eta h)(L^2 - x^2)$ . The total flow through the slot is

$$\frac{V}{t} = 2 \int_0^L u \, dx = \frac{2p}{2\eta h} \int_0^L (L^2 - x^2) \, dx = \frac{2}{3} \frac{pL^3}{\eta h}.$$

From (4),

$$(7) \quad C = 2NL^3d/3\eta.$$

From this discussion, it is clear that if the ice structure bears any resemblance to either model, there will be distinctly different permeabilities along and across the "grain" of the ice. Permeability to brine  $C_B$  is the parameter of main interest but it may be simpler experimentally to measure permeability to air  $C_A$ . From (6) and (7), these will bear the relation

$$(8) \quad \frac{C_B}{C_A} = \frac{d_B}{d_A} \times \frac{\eta_A}{\eta_B} \simeq \frac{1}{6}$$

using values of the densities and viscosities at  $0^\circ \text{C}$ .

A meter for testing the air permeability of slabs cut from an ice sheet was designed and built on the icebreaker in late summer, 1956. It was also used at Shippagan. It was found that  $C_A$  varies by a factor of about  $10^6$  between fresh-water ice and the lower layers of annual sea ice. The meter did not have this range and attempts to improvise methods of extending the range led to such a scatter of results that they will not be quoted. The instrument was redesigned by Dr. M. P. Langleben at McGill and a report on the instrument and permeability data obtained with it will be published later.

A method of testing permeability *in situ* was also used. Holes of 4.5-in. diameter were drilled with a S.I.P.R.E. corer to depths of 4, 8, 12, 16, 20, and 25 inches on Feb. 26. The air temperature was  $-6$  to  $-7^\circ \text{C}$ . The rate of brine seepage into the holes was measured, and when there was enough brine its salinity and temperature were measured also. The results are shown in Fig. 27A. Calculation of permeabilities from this data requires assumptions about the ice structure and the flow mechanism. It was noted in Section 3 (a) that the block of ice studied on Feb. 23 showed a transition layer at a depth of 20 in., from small, roughly equidimensional crystals to long, vertical ones. Above this layer, horizontal and vertical permeabilities should have been about equal and below it the vertical permeability should have increased

greatly. The sharp difference in the accumulation rates for the 20- and 25-in. holes bears this out. Assuming equal vertical and horizontal permeabilities, the area of the vertical surfaces of the holes was so much greater than that

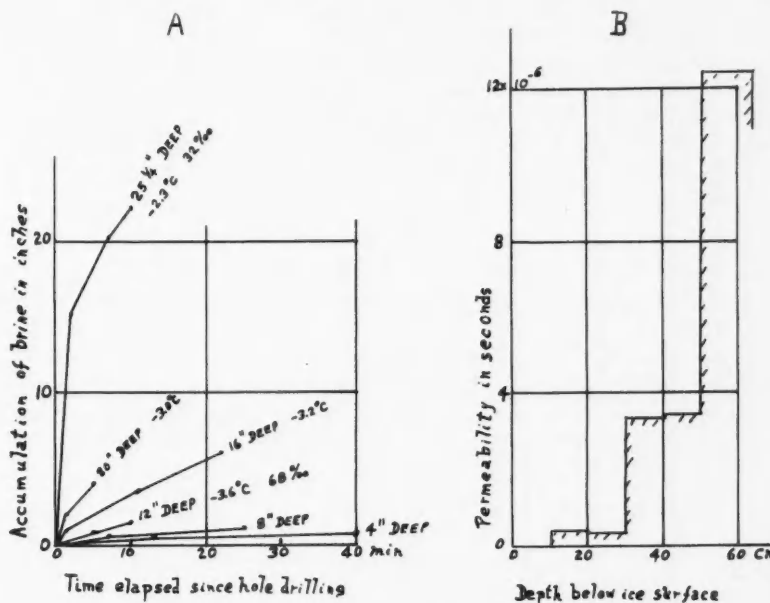


FIG. 27. Permeability by brine seepage *in situ*. Shippagan, N.B., Feb. 26, 1957.

of the horizontal ends that flow upward through the bottom can be neglected. Comparison of accumulation rates for holes of successive depths can be used to find the volume transport rate per unit area. Let  $D$  be the difference (in cm/sec) in the rate at which the brine level rises in the two holes. The excess rate of volume accumulation is  $D\pi R^2$  where  $R$  is the radius of the hole (5.7 cm). Let  $H$  be the extra depth (10 cm) of the second hole. Consider the flow through the wall of a cylinder of radius  $r$  and height  $H$ . If  $v$  is the radial velocity at  $r$ ,

$$\frac{\Delta V}{t} = 2\pi r H v \text{ and } \frac{\Delta V}{t} \text{ also} = \pi R^2 D.$$

The differential form of (4) is

$$C = \frac{d\Delta V}{t\Delta A} \Big/ \frac{dp}{dr} = dv \Big/ \frac{dp}{dr} = \frac{\pi R^2 D d}{2\pi r H} \Big/ \frac{dp}{dr}$$

$$\frac{dp}{dr} = \frac{R^2 D d}{2r H C}.$$

Integrating,

$$(9) \quad p - p_0 = (\ln r - \ln r_0) \frac{R^2 D d}{2 H C}.$$

If  $r_0$  is set equal to  $R$ ,  $p_0 = 0$ . At some distance from the hole, the average pressure at this depth tends to  $hdg$ , where  $h$  is the distance from the middle of the bottom 4-in. section of the deeper hole to the top surface of the ice (more accurately, to the sea level). It is hard to estimate the radius  $r$  at which the pressure field is effectively undisturbed by the presence of the hole. To permit calculation, let us assume that for  $r = h+R$  the pressure  $p = hdg$ , recognizing that this may be underestimating the proper value of  $r$  by a factor of up to 5 or 6. Then

$$(10) \quad C \simeq \left[ \ln \left( \frac{h+R}{R} \right) \right] \frac{R^2 D}{2 H d g}.$$

Values of  $C$  calculated from (10) are given in Table V and plotted in Fig. 27B. The  $D$  values are taken from the *initial* slopes of the accumulation curves. It is evident that salt water could move fairly easily through this ice when any pressure gradient was established. It is doubtful if sea ice is ever really impervious to sea water. Similar experiments have been done by the second author on several occasions in midwinter and brine drainage was always observed.

TABLE V  
Permeability of sea ice

$h$ = depth		$D$		$C \times 10^6$ , sec
in.	cm	in./min	cm/sec	
6	15.2	.0714—.0125	= 0.00249	0.35
10	25.4	.150—.0714	0.00333	0.32
14	35.6	1.00—0.150	0.0360	3.3
18	45.8	2.00—1.00	0.0423	3.4
23	58.3	7.60—2.00	0.238	12.4

(g) *Strength Tests*

The compression strength of ice is important practically, but measurements of it tend to be very inconsistent. Small beams under a compression load usually break diagonally by shearing or by the buckling and bending of filaments of ice. For this reason, strength tests were limited to breaking beams in tension and shear and to measuring impact hardness. The methods used avoided clamping of the specimens.

(i) *Tensile Strength*

Beams were tested by bending in a wooden frame shown in Fig. 28. The winter results are shown in Fig. 29 with the code symbols explained in Fig. 30. A much larger number of tests is needed but the following conclusions seem to be true. The tensile strength: (1) decreases with increasing temperature,

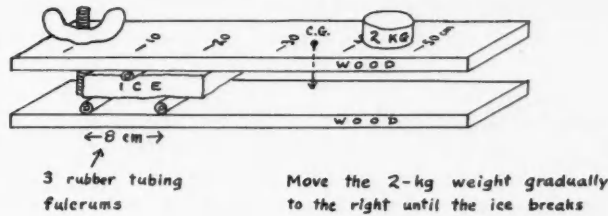


FIG. 28. Test frame for measuring tensile strength by bending. The top board weighs 530 g and its C.G. is 33.4 cm from the pivot bolt.

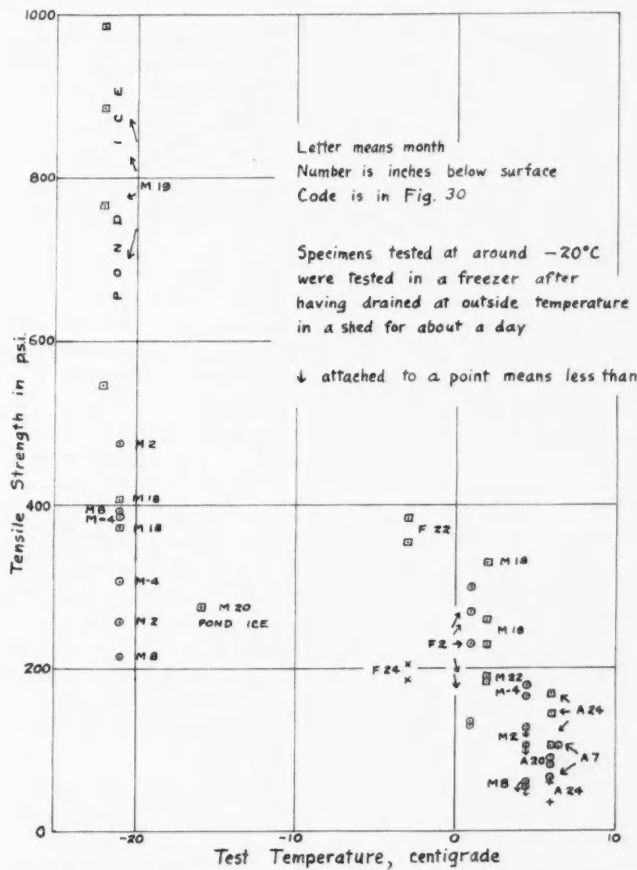


FIG. 29. Tensile strength vs. temperature, with date and depth of sample.

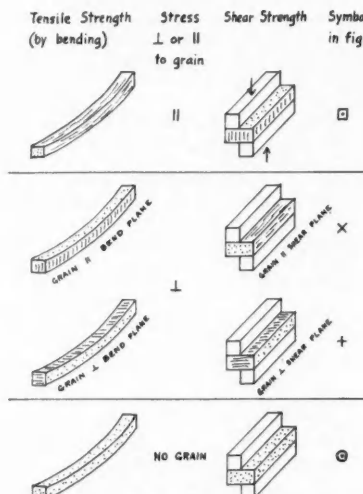


FIG. 30. Code for strength graphs. "Grain" is in direction of longest dimension of crystals, not necessarily in direction of main crystal axis.

(2) is greater with the stress parallel to the grain, (3) is greater for pond ice than for sea ice. The test frame gave consistent results on any one set of specimens, with an average deviation of around 14%. On the icebreaker cruise, tensile strengths of sea-ice specimens varied from about 220 to 460 p.s.i. with a mean of about 325 p.s.i. These were tested in a freezer at  $-16^{\circ}\text{C}$ . There was no appreciable "grain" in this summer ice.

Butkovich (1956) made tensile tests on small hollow cylinders of sea ice at Hopedale, Labrador, in March 1956. His results are from about 110 p.s.i. at  $-4^{\circ}\text{C}$  to 170 p.s.i. at  $-18^{\circ}\text{C}$ , with the salinity of the ice being about 6‰. Our strength values are about double these figures, but we had lower salinities of 0 to 4‰ and his method applied the stress across the grain, the weakest case. He and others have found a "skeleton layer" at the bottom of the ice. This was not observed at Shippegan, possibly because of the flushing action of the tidal currents.

Butkovich did bending tests with small beams cut horizontally from the ice, with stress again across the grain, and obtained about the same tensile strengths as with the ring tests. However, in-place, large-beam tests gave less than half the strength of the other tests, around 40 to 50 p.s.i. when the top of the ice was about  $-6^{\circ}\text{C}$ .

For pond ice at  $-22^{\circ}\text{C}$ , we found the strength to be 500 to 1000 p.s.i. parallel to the grain. Butkovich (1954) reports values of the tensile strength of lake ice and commercial ice varying from 100 to 200 p.s.i. at  $0^{\circ}\text{C}$  to 180 to 240 p.s.i. at  $-20^{\circ}\text{C}$ , either by flexural tests or by direct tension. However, in none of these tests was the tension parallel to the grain. Mantis (1951) quotes similar results to those of Butkovich but specifies neither temperature

nor grain direction. Both give empirical formulae for the variation of tensile strength with temperature. The formulae give results agreeing within a factor of two.

(ii) *Shear Strength*

The shear strength was measured by placing a beam between metal plates on a hydraulic press as shown in Fig. 31. The plates were machined with sharp

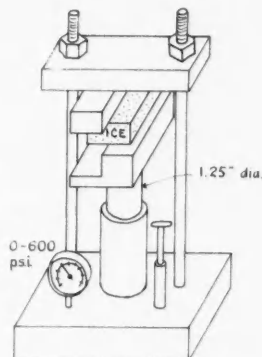


FIG. 31. Hydraulic press with face plates for single-shear tests. Specimen is usually about 1 in.  $\times$  1.5 in.  $\times$  4 in.

right-angled corners. In this single-shear method the samples always tilted slightly before breaking because the center of pressure of each plate was at a little distance from the edge. To allow for this, the actual cross-sectional area of the break was always measured. Specimens were usually about 1 in. thick by 1.5 in. wide by 4 in. long. The winter results are shown in Fig. 32. More data are needed but it seems clear that the shear strength: (1) is greatest in the case where the grain is perpendicular to the stress and to the shear plane, (2) is greater at lower temperatures, (3) is larger for pond ice than sea ice.

The consistency of the method for a set of similar specimens was about the same as in the tensile tests. The shear strength of the summer ice in the Arctic averaged around 110 p.s.i., varying from 95 to 125 p.s.i., for specimens stored for some time at  $-16^{\circ}$  C. It was found that when specimens stored at  $-16^{\circ}$  C were "annealed" for 1 hour at  $+14^{\circ}$  C, the shear strength dropped by 50% and the tensile strength by about 20%, giving about equal shear and tensile values under these conditions.

Initially, an unclamped, double-shear method was tried, but it was unsatisfactory because the tilting observed with the single-shear method resulted in this case in bending of the sample, which always broke halfway between the shear planes because of bending stress rather than pure shear stress.

Butkovich (1956) found the shear strength of young sea ice, by double shear of a clamped 3-in. diameter cylinder, to be about 230 p.s.i. at  $-6.4^{\circ}$  C and 340 p.s.i. at  $-11.8^{\circ}$  C. In these tests the shear stress was perpendicular

to the grain. These values are about three times as great as ours, but in most of our tests the shear plane was parallel to the grain.

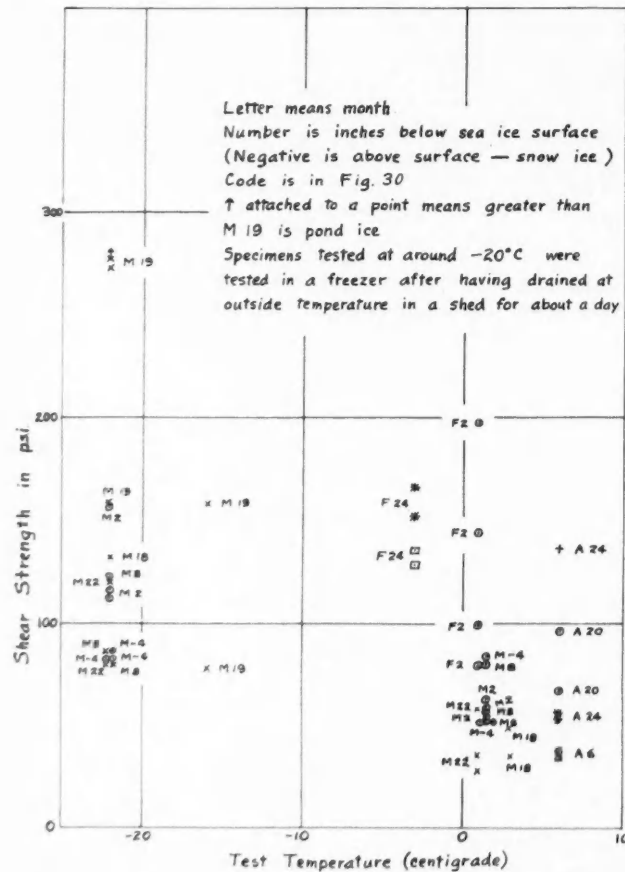


FIG. 32. Shear strength vs. temperature, with date and depth of sample.

The shear strength of pond ice was measured as 160 to 270 p.s.i. at  $-20^{\circ}\text{C}$ , with the shear plane parallel to the grain. Butkovich (1954) and Mantis (1951) have also reported values for the shear strength of fresh-water ice. Agreement between the three sets of values is as close as can be expected in view of the differences in techniques of measurement.

(iii) *Impact Hardness*

The hardness of ice was tested by dropping a 16-lb shot from head height and from knee height, and measuring the diameter of the indentation. This test resembles the Brinell hardness test but the latter is a static test and for a

brittle material like ice it is not certain that Brinell hardness and impact hardness ( $H_i$ ) would be the same. The theory of the present test can be worked out with reference to Fig. 33, in which  $a$  is the radius of the shot, and  $x$  and  $r$  are the instantaneous values of the penetration of the shot into the surface and

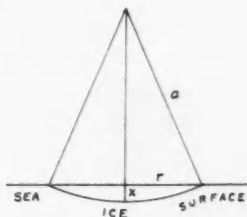


FIG. 33. Diagram for derivation of impact hardness equation.

the radius of the indentation. Let  $x_0$  and  $r_0$  be the final values reached when the shot comes to rest. The impact hardness may be defined as the resistance to crushing per unit plane area of indentation. The retarding force at any instant is thus  $H_i \cdot \pi r^2$ , and the work done by the ball in a displacement  $dx$  is  $\pi r^2 H_i dx$ . The integral of this work should equal the loss of potential energy of the ball. If a ball of weight  $W$  is dropped from a height  $h$ ,

$$Wh = \int_0^{x_0} \pi r^2 H_i dx = H_i \int_0^{x_0} \pi [a^2 - (a-x)^2] dx$$

where we have assumed  $H_i$  to be constant throughout the impact. This is probably only roughly true. Since  $r_0$  is the quantity measured, we carry out the integration and use the geometry to express  $x_0$  in terms of  $r_0$ , with the following results:

$$(11) \quad H_i = \frac{Wh}{\pi (ax_0^2 - x_0^3/3)}$$

$$(12) \quad x_0 = a - (a^2 - r_0^2)^{1/2}.$$

Several measurements of this type were made on the ice in Foxe Channel on July 28. Values of  $H_i$  ranged from 660 to 900 p.s.i. Compression strengths found on this icebreaker trip ranged from 200 to 1300 p.s.i. One would expect the two quantities to be similar. These hardness values give the order of magnitude of the maximum pressures between and in floes during rafting, and of the maximum pressure on an icebreaker hull during operations in summer ice.

#### (h) Expansion and Contraction

Figure 34 shows a device, consisting of three dial indicators mounted on telescoping extension legs, used to measure the expansion and contraction of the top part of the ice in the region of the tide cracks near shore. It was placed in a position about 120 feet from the shore line. Of the three indicators, only the one measuring the strain perpendicular to the shore showed much change. In one test, on Feb. 22, the strain changed by 0.0148 inch in 1-meter length in

a period of 3.5 hours. The ice was 32 in. thick, and it can be shown that the radius of curvature thus introduced was about 3500 ft, if the ice sheet was originally flat. Since the elastic properties for such a slow rate of strain are not known, the stress cannot be calculated.

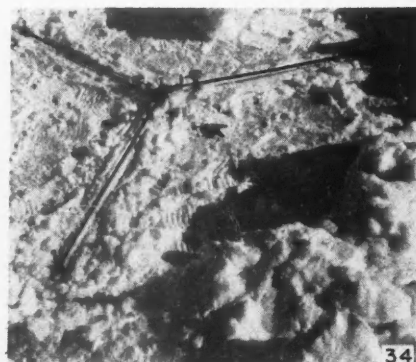
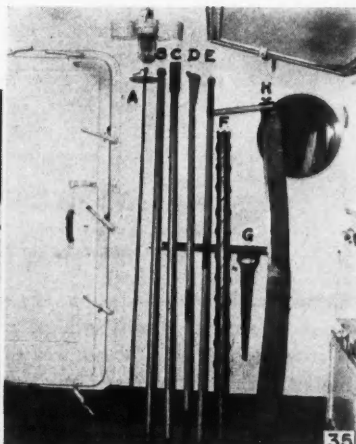


FIG. 34. Device for measuring expansion and contraction in the zone of tide cracks. Four 12-in. nails anchor the center and the ends of three 1-meter long telescoping arms. Changes in the lengths of the arms are recorded on the dial indicators.

FIG. 35. Miscellaneous instruments and tools used on the icebreaker.

Figure 35 shows some of the tools used in this work—indeed an odd lot for physicists. A torsion vane current meter is shown at A, used for measuring water currents through a hole in the ice. At C is a 2-in.  $\times$  6-ft ice chisel (of a design suggested by T. A. Harwood and Lt.-Cmdr. J. P. Croal of the Defence Research Board), and at D an ice scoop for removing the chips. The combination, with if necessary the extension rods at B and E, can be used to dig a hole in ice quite rapidly. The use of the pruning saw at G and the logger's saw at H is evident. Not shown is a gasoline-operated chain saw which proved very useful for cutting in a thick continuous ice cover. An ice corer (F), which was made in the ship's machine shop, was less satisfactory than the S.I.P.R.E. model. Another useful S.I.P.R.E. kit is a 1-in. drill with extensions for measuring ice thickness.

The authors wish to thank the Defence Research Board of Canada (and in particular Mr. T. A. Harwood) and Dr. Waldo K. Lyon and the other authorities of the U.S. Navy Electronics Laboratory who made this collaboration possible. Our thanks are due to the Department of Fisheries of Canada for the use of the building at Shippagan, to Mr. H. R. Found for making the arrangements, and to Mr. Hilarion Robichaud, officer-in-charge of the Shippagan biological station for his very great assistance throughout our winter pro-



gram. The Royal Canadian Navy supplied transportation to the Arctic and facilities on board H.M.C.S. *Labrador*. Excellent co-operation was received from Capt. T. C. Pullen and his crew, and from the other scientists (from Atlantic Oceanographic Group and the Canadian Hydrographic Service) on the expedition. This work was supported by the Defence Research Board through D.D.P. Contract C.69-10-157.

## REFERENCES

ASSUR, A. 1956. Snow, Ice, and Permafrost Research Establishment, SIPRE Report 36 (U.S. Army Corps of Engineers, Wilmette, Ill.).

BROWN, R. M. and GRUMMIT, W. E. 1956. Can. J. Chem. **34**, 220.

— 1958. Private communication.

BUTKOVICH, T. R. 1954. Snow, Ice, and Permafrost Research Establishment, SIPRE Research Paper 11 (U.S. Army Corps of Engineers, Wilmette, Ill.).

— 1956. Snow, Ice, and Permafrost Research Establishment, SIPRE Research Report 20 (U.S. Army Corps of Engineers, Wilmette, Ill.).

BYERS, H. R. 1937. Synoptic and aeronautical meteorology (McGraw-Hill Book Co., Inc.), p. 255.

DELAND, R. J. and PANOFSKY, H. A. 1957. Pennsylvania State University, Department of Meteorological Science, Report No. 2.

DICHTEL, W. J. and LUNDQUIST, G. A. 1949. An investigation into the physical and electrical characteristics of sea ice. U.S. Naval Ordnance Laboratory Report.

GIER, J. W. and DUNKLE, R. V. 1951. Proc. Am. Inst. Elec. Engrs. **70**, 339.

HAURWITZ, B. 1941. Dynamic meteorology (McGraw-Hill Book Co., Inc.), p. 200.

KUSONOKI, K. and TABATA, T. 1954. Some remarks on the method of sampling of sea ice. L'Association Internationale d'Hydrologie (Gen. Assembly of Rome, Book 4), publication 39.

MALMGREN, F. 1927. Norwegian north polar expedition with the "Maud", 1918-25. Scientific results, Vol. 1 (5).

MANTIS, H. T. 1951. Snow, Ice, and Permafrost Research Establishment, SIPRE Report 4 (U.S. Army Corps of Engineers, Wilmette, Ill.).

THORNTWaight, C. W. and HALSTEAD, M. H. et al. 1954. Climatology, Vol. 7 (2) (Johns Hopkins University Publications).

WEEKS, W. F. 1957. Bull. Geol. Soc. Am. **68** (12).

WHITMAN, W. G. 1926. Am. J. Sci. **211**, 126.

# QUASI-PERSISTENT CURRENTS IN RINGS COMPOSED OF SUPERCONDUCTING AND NON-SUPERCONDUCTING REGIONS<sup>1</sup>

H. J. FINK

## ABSTRACT

A number of rings composed of a superconductor (Pb, In) apart from a small insert of normal metal (Cu) perpendicular to the current flow have been investigated between 1.30° K and 4.33° K for Pb-Cu and between 1.30° K and 3.20° K for In-Cu. It was found that for samples with good electrical contact the decay of the magnetic field due to the current is exponential and that the effective resistance increased compared with the bulk resistance of Cu by approximately 2.1 for the Pb-Cu rings and by 18.5 for the In-Cu rings. Two different thicknesses of the Cu inserts (0.0125 cm and 0.0053 cm) were used and it was found that the resistivity of the thin Cu insert increased with respect to the thick foil by 16% for the Pb-Cu system and by 36% for the In-Cu system. Part of this relative increase can be explained as a size effect due to electron scattering in the Cu insert. The effective resistance of the Pb-Cu rings shows a maximum at approximately 3.4° K. The resistance of the In-Cu samples decreases by about 10% between 3.2° K and 1.3° K. The resistivity of the Cu foil when measured separately was constant for the above temperature range. For samples with "poor" electrical contact (probably due to some copper oxide on the insert) two definite relaxation times were observed. For these samples the effective resistance was current and temperature dependent and it was decreasing for decreasing currents and decreasing temperatures. This can be explained in terms of a rectification effect of the two oxide layers on the insert. The decay of the magnetic field of the ring is consistent with the decay of a current in an  $L-R$  circuit.

## I. INTRODUCTION

When a current is flowing from a superconductor into a normal conductor, then under steady-state conditions the boundary surface will be an equipotential surface because the electric field in the superconducting metal is zero. From Maxwell's second equation it follows that for steady-state conditions  $\text{curl } \mathbf{E} = -\dot{\mathbf{B}} = 0$  and therefore the current will be homogeneously distributed over the contact surface as it is over any cross section of the normal conductor (von Laue 1949; London 1950). Because the superconducting current is a surface current and the current in the normal conductor is evenly distributed over the cross section the path of the current must be bent in the superconductor at the normal-superconducting boundary such that the above boundary conditions are satisfied. In addition one could imagine that some of the electrons moving from the superconducting into the normal metal (or vice versa) are scattered at the boundary. It was decided to investigate a closed system (circular ring) composed almost entirely of a superconductor apart from a small segment of a normal metal. When a current is induced in the ring and the normal metal is perpendicular to the current flow then one would expect the current to decay exponentially with a time constant  $L/R$ , where  $L$  is the inductance of the ring determined by its geometrical dimensions, and  $R$  is the resistance of the ring due to the normally

<sup>1</sup>Manuscript received December 24, 1958.

Contribution from the Department of Physics, University of British Columbia, Vancouver, B.C.

conducting insert. When the decay of the magnetic field due to the decay of the current in the ring is measured one is able to determine the time constant of the ring and from this one can derive the effective resistance. When the current decays in the ring curl  $\mathbf{E}$  is no longer zero as in the steady-state case. It seems worth while to perform experiments to measure the effective resistance of the rings for different metals to see if there is any large deviation from the bulk resistance of the foil. These results should give some information about scattering at the normal and superconducting boundaries. On removal of an external magnetic field a quasi-persistent current is induced in the ring and its initial value should be proportional to the magnitude of the applied magnetic field as long as the applied magnetic field is smaller than or approximately equal to half the critical field of the superconductor. If a magnetic field perpendicular to the plane of the ring which is larger than the critical field is removed from the ring, the superconducting material will be in the normal state as long as the magnetic field on the surface of the metal due to the current is larger than the critical field. When the current drops to its critical value the metal should go over into the superconducting state. Therefore it seems also worth while to investigate by direct magnetic measurements if the maximum effective initial current is determined by the critical field of the superconductor.

## II. EXPERIMENTAL PROCEDURES AND RESULTS

The resistivity of the Cu foils was measured by a conventional current-voltage method. Two different thicknesses of the Cu insert were used. Figure 1(a) shows the arrangement of the samples. A and B are the current leads and C and D are the connections to measure the potential drop across  $l$ ;  $l$  was

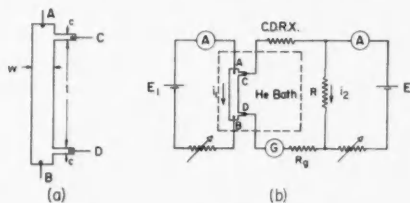


FIG. 1. (a) Cu sample for resistance measurement.  
(b) Potentiometer circuit for resistance measurement of Cu samples.

approximately 10 to 11 cm,  $w \simeq 1/2$  cm, and  $c \leq 0.1$  cm. The thickness of the Cu foils was 0.0125 and 0.0053 cm. Figure 1(b) shows the circuit diagram of the potentiometer circuit for measuring the resistance of the above samples.  $E_1$  is a bank of storage batteries of 110 volts,  $E_2$  an ordinary battery,  $A$  are ammeters,  $R$  a standard resistor (0.1 ohm), and  $G$  a galvanometer which was critically damped. The sensitivity of  $G$  was  $3.88 \times 10^{-4}$   $\mu$ a/mm on a scale 4 meters from  $G$ . The internal resistance of  $G$  was 22.2 ohms and the critical external damping resistance was 45 ohms. The current  $i_1$  was varied between 100 ma and 500 ma. When the voltage drop across  $CD$  is the same as the voltage drop across the standard resistor  $R$  then  $G$  gives no deflection. Whenever the temperature was changed one had to wait approximately 1/2 hour

until the fluctuations of  $G$  died away but small fluctuations remained such that the readings could be taken only within  $\pm 2$  mm. The only limitation on the accuracy is the sensitivity of  $G$ , the fluctuations, and the accuracy of the ammeters. The resistance of the samples could then be measured within 1%. For the Cu foil of thickness 0.0125 cm the resistivity was  $6.62 \times 10^{-9}$  ohm-cm and for the 0.0053-cm foil,  $8.06 \times 10^{-9}$  ohm-cm. All readings were constant between  $1.3^\circ$  K and  $4.3^\circ$  K. From experimental results of the anomalous skin effect by Chambers (1950) the mean free path of the electrons may be calculated from  $\rho l = 6.5 \times 10^{-12}$  ohm-cm $^2$ ;  $l$  is then of the order of  $10^{-3}$  cm. The mean free path of the electrons is of the same order of magnitude as the thickness of the foils. If one applies a correction for the size effect of "thick" films (MacDonald 1956) the bulk resistance of the 0.0125-cm foil is approximately 3% smaller and that of the 0.0053-cm foil approximately 6%.

The copper foils were carefully covered with 99.98% pure lead foil or 99.95% pure indium. Heat was then applied simultaneously on both sides of the foil, the temperature being just a few degrees above the melting point of lead or indium. Some samples were prepared in air and some while blowing helium gas across the foil. There were no differences in the final result within the accuracy of the experiment. The surface of the Cu foil had to be free from oxide, otherwise In and Pb did not stick on the copper and especially the Pb-Cu samples were difficult to prepare. A number of lead and indium rings were cast around copper inserts in an aluminum mold. Samples 1c, 2b, 2c, and 4b (see Table I) were prepared 1 day before the experiments were performed and the rest of the samples were cast approximately 3 months before measurements were taken. All the rings were of the same dimensions. The mean radius,  $a$ , of the rings was 1.305 cm and the radius of the circular cross section,  $b$ , was 0.205 cm. Therefore for an entirely superficial current the inductance of the ring was  $31.7 \times 10^{-9}$  henries (Shoenberg 1952).

The actual field measurements were performed by comparing the horizontal components of the magnetic field due to the decaying current with the horizontal component of the magnetic field of the earth. The instant at which these components are equal and opposite could be observed by the "flip-over" of a compass needle. By observing the times of flip-overs at different distances from the ring the decay of the current could be determined. Figure 2(a) shows the magnetic field components due to the current in the ring. When the compass needle flipped over, the horizontal component of the earth's magnetic field  $H_h$  balances the horizontal component of the magnetic field due to the current. Therefore (Smythe 1950) at balance:

$$(1) \quad H_h = H_p = \frac{I_0 e^{-t/\tau}}{2\pi} \cdot \frac{z}{\rho[(a+\rho)^2+z^2]^{1/2}} \left[ \frac{a^2+\rho^2+z^2}{(a-\rho)^2+z^2} E - K \right],$$

where  $I_0$  is the current at  $t = 0$ ,  $\tau$  the time constant of the ring,  $a$  the radius of the ring,  $\rho$ ,  $z$ , and  $H_p$  the quantities as defined in Fig. 2(a), and  $K$  and  $E$  are complete elliptic integrals of the first and second kind and they are functions of  $k^2$ , where  $k^2$  is defined by:

$$(1a) \quad k^2 = \frac{4a\rho}{(a+\rho)^2+z^2}.$$

TABLE I

Superconducting materials, thickness of the Cu inserts, time constants, effective resistivity of the Cu inserts, and relations between the resistivities ( $\rho_0$  is the resistivity of the bulk Cu)

Sample No.	Superconducting material	Thickness of Cu insert, $\times 10^3$ cm	Range of temperatures investigated, °K	$(\tau)_{av}$ sec	$\rho \times 10^9$ ohm-cm	$\rho/\rho_0$	$\rho_{12.5}/\rho_{5.3}$	$\rho_{In}/\rho_{Pb}$
1a	Pb	12.5	4.22 1.35	21.2				
1b	Pb	12.5	4.23 1.30	23.6				
1c	Pb	12.5	4.21 1.32	26.3				
1d	Pb	12.5	4.22 1.33	38.2				
Average				27.4	12.2	1.90		
2a	Pb	5.3	4.23 1.32	33.4				
2b	Pb	5.3	4.23 1.31	42.4				
2c	Pb	5.3	4.23 1.31	52.4				
2d	Pb	5.3	4.22 1.35	55.9				
Average				46.0	17.2	2.26	0.710	
3a	In	12.5	3.20 1.34	3.36				
3b	In	12.5	2.32 1.33	3.82				
Average				3.59	93.4	14.5		7.65
4a	In	5.3	2.31 1.38	4.59				
4b	In	5.3	2.35 1.30	4.59				
Average				4.59	172	22.6	0.543	10.0

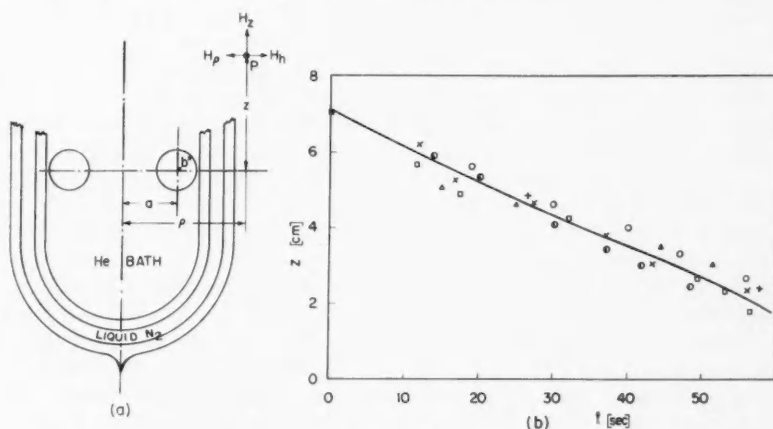


FIG. 2. (a) The magnetic field distribution at a point P.  $H_p$  and  $H_z$  are due to the current in the ring and  $H_h$  is the horizontal component of the magnetic field of the earth.

(b) The "flip-over" of a small compass needle for sample 1a at 4.22°K;  $z$  is the distance as shown in Fig. 2(a).

Figure 2(b) shows a plot when the compass needle "flipped over", where the distance  $z$  is plotted as a function of time. This method is not very accurate to determine  $\tau$ ; its main purpose was to check if the magnetic field at  $t = 0$  for a ring with a non-superconducting insert is the same as compared with a ring without an insert. The curve in Fig. 2(b) was extrapolated to  $t = 0$ . Then a separate experiment was performed with a completely superconducting ring of the same dimensions and the same superconducting material. In both cases the external applied field which was removed was larger than  $H_c/2$ . The current was therefore the maximum possible persistent current for the completely superconducting ring. For the ring with the normal insert the current at  $t = 0$  (due to the extrapolation) may be compared with the above current. For an applied field larger than  $H_c/2$  the initial current will be larger than  $I_c$ , but this current will decay very rapidly because the material of the ring is in the normal state. When the current reaches the critical current (within a fraction of a second) the ring (except the insert) does become superconducting and the effective initial current as determined from Fig. 2(b) is just this current and it is the same as the maximum persistent current within the accuracy of the experiment. In the further discussion of this paper the maximum persistent current is always considered the maximum initial current. Figure 2(b) shows the experimental points of sample 1a for currents circulating in clockwise and counterclockwise direction in the ring. The plot in Fig. 2(b) was calibrated by the magnetic field measurements of the completely superconducting sample. The ratio  $I_0/H_h$  was calculated for the above sample from eq. (1) and (1a) for  $z = 7.1$  cm,  $t = 0$ , and  $\rho = 3.00$  cm. With the above ratio the solid line in Fig. 2(b) was plotted for  $\tau = 21.5$  seconds.

To determine the time constants of the rings accurately (better than 2%) the rings were coupled to a coaxial coil which was in series with a sensitive galvanometer and an external critical damping resistance. The undamped period of the galvanometer was 4.7 seconds. When the external magnetic field was removed a switch in the galvanometer circuit was closed and the rate of decay of the magnetic field due to the quasi-persistent current was observed. For observation times larger than 5 to 6 seconds after removal of the external field the galvanometer follows accurately (within 1%) the induced current in the coaxial coil due to the decaying magnetic field of the ring. The rate of decay of the magnetic field for all the samples in Table I was of the form  $I = I_0 e^{-t/\tau}$ .

Figure 3a shows the galvanometer deflection of sample 4a plotted as a function of time for various initial currents at  $1.38^\circ\text{K}$  and  $2.31^\circ\text{K}$ . For  $I_0 < I_c$  in Fig. 3a  $I_0$  was the same for both temperatures. Figure 3b shows a similar plot for sample 1d for initial currents  $I_0 = I_c$  at various temperatures. From the slope of the galvanometer versus time plot the time constants of the various samples were determined and the average tabulated in Table I. The tabulated values of the time constants are average values over the temperature range stated in Table I for various initial currents.  $I_0$  was varied for some samples from  $I_c$  to approximately  $I_c/7$ . No variation of  $\tau$  for different current was found within the accuracy of the experiment. Figure 4(a) shows

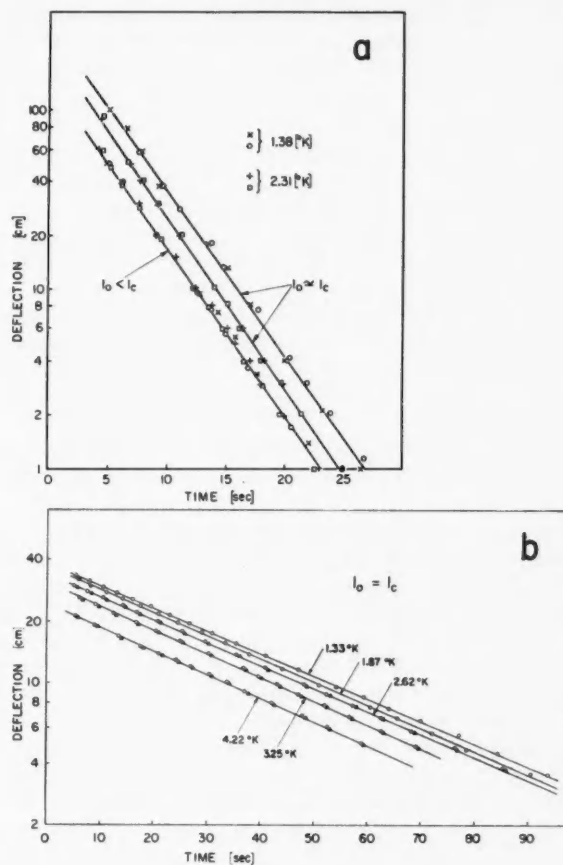


FIG. 3. The deflection of the galvanometer due to the decaying current in the ring for (a) sample 4a and (b) for sample 1d.

$\tau$  plotted as a function of temperature for samples 1a and 1d and Fig. 4(b) shows the same for sample 3a. The time constants of the Pb-Cu system showed a minimum of approximately 3% at  $3.4^\circ$  K as compared with the time constant at  $4.22^\circ$  K, and for the In-Cu samples the time constant was increasing between  $3.2^\circ$  K and  $1.3^\circ$  K by approximately 10%. However, the effective resistance of the rings was very much different for the two systems with the same thickness of the Cu insert. The effective resistance in the In-Cu systems was approximately nine times larger than in the Pb-Cu rings, and in the average the absolute value of the resistivity of the Cu insert increased by a factor of approximately 2.1 in the Pb-Cu ring as compared with 18.5 in the In-Cu ring. The ratio of the bulk resistivity of the "thick" to the "thin"

foil is 0.847. When this value is compared with the measured ratios due to the decay of the current (Table I) one notices that for the Pb-Cu system the above ratio decreased by approximately 16% and for the In-Cu rings by 36%.

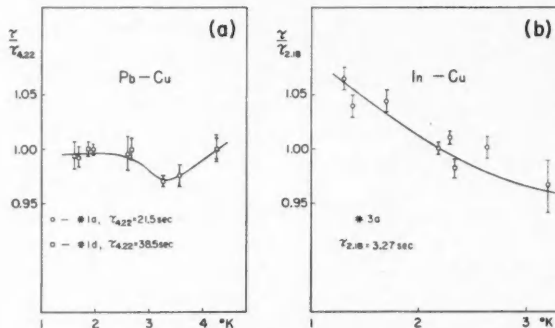


FIG. 4. The ratio of the time constants as a function of temperature (a) samples 1a and 1d (Pb-Cu), (b) sample 3a (In-Cu).

However, due to the difficulties in preparing the Pb-Cu rings the measured time constants for these systems strayed (Table I). This is probably due to different quality in electrical contact between the lead and the copper. The surface at the contact between Pb and Cu was visually inspected with a magnification of 10 and it was found that the copper foil for samples 1a, 1b, and 2a was slightly bent, the Pb at the surface on the contact surface showed small holes, and the contact was not as clean as for samples 1d, 2c, and 2d. Samples 1c and 2b were of intermediate quality between the above two groups as far as visual inspection is concerned. Therefore the rings with the longer

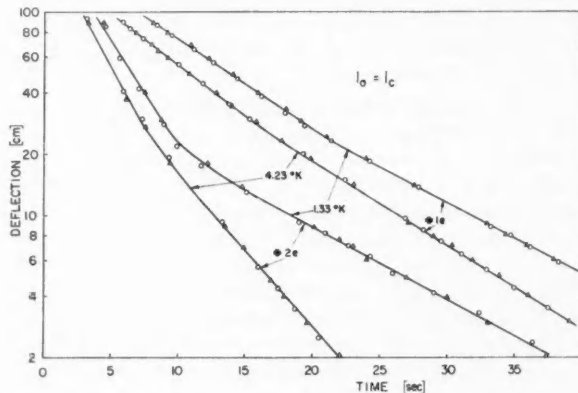


FIG. 5. The deflection of the galvanometer as a function of time for two "faulty" Pb-Cu samples, No. 1e with  $a = 0.0125$  cm and No. 2e with  $a = 0.0053$  cm Cu insert. The number of turns of the pick-up coil coaxial to the ring was different for the two samples.

time constants appear to be more reliable samples. Comparing the rings with the longest time constants only, one finds that the resistance of the Cu insert in the Pb-Cu rings increases by a factor of approximately 1.6 as compared with the bulk Cu and in the In-Cu rings it increases by 18.1. The ratio of the resistivity of the "thick" to the "thin" foil decreases for the Pb-Cu rings by 26% and for the In-Cu rings by 40%.

The Pb of sample 1e ( $12.5 \times 10^{-3}$  cm Cu insert) and of sample 2e ( $5.3 \times 10^{-3}$  cm Cu insert) had a "poor" electrical contact with the Cu foil (they are not included in Table I). Figure 5 shows the plot of the galvanometer deflection versus time for these samples at  $1.33^\circ\text{K}$  and  $4.23^\circ\text{K}$  for initial currents  $I_0 = I_c$ . There are two distinct time constants. The same curves were reproduced when the current direction in the rings was reversed. After the experiment of sample 2e, the Pb ring could be pulled apart from one side of the Cu insert which indicated a poor mechanical contact. No such curves were obtained for In-Cu samples.

### III. UNCERTAINTIES OF THE MEASUREMENTS

The accuracy of the resistance measurement of the Cu samples by the current-voltage method was  $\sim 1\%$ ; the accuracy of the time constant measurement for various initial current ( $I_0 = I_c$  to  $I_c/7$ ) was better than 2% for constant temperature. For constant temperature the dissipation of energy in the Cu insert due to the current was varied approximately by a factor of 50. This did not change the effective resistance within the above accuracy of the measurement, and therefore errors due to the heating of the Cu foil may be neglected. At  $1.3^\circ\text{K}$  the critical current of the In samples was 3.3 times smaller than that of Pb and at higher temperatures even smaller. Therefore the increased resistance in the Cu foil in the In rings compared with the Pb rings was not due to overheating of the insert. No interdiffusion data for Pb and Cu, and Cu and In could be found in the literature. Probably the diffusion rates are very small and have not been measured. The mean free path of the electrons in the bulk Cu is of the same order of magnitude as the thickness of the inserts.

The main uncertainty is in the contact between the superconducting material and the Cu insert. A good contact was fairly easy to achieve for the In-Cu samples and difficult for the Pb-Cu rings: therefore the large stray in  $\tau$  for the latter. However, the author believes that the samples with the larger time constants had a good contact over the whole cross section of the ring. The thickness of both Cu foils varied by  $\pm 3\%$  and their impurity content was unknown. For the determination of the effective resistivity of the rings  $L$  was calculated for an entirely superficial current. This is not exactly correct because the current in the insert is not superficial. The error in  $L$ , however, can be neglected compared with the above uncertainties.

### IV. DISCUSSION

(a) When one performs experiments with multiply connected bodies such as rings the measurements which are taken are actually magnetic and from

these one deduces the electrical properties of the sample. By measuring the ratio of the magnetic moment to the angular momentum when a magnetic field was applied to a superconducting sphere, Kikoin and Goobar (1938, 1940) and Pry, Lathrop, and Houston (1952) showed that the Landé *g*-factor of a superconductor is approximately unity, which indicates that the diamagnetism of a superconductor is caused by ordinary electron flow and not in any way by the electron spin. The present experiments confirm the electrical properties of a superconductor. By decreasing the thickness of a small non-superconducting insert the time constant of an exponential decay of a magnetic field increased correspondingly. For zero thickness of the insert the magnetic field will be equal to the initial magnetic field with finite insert. Because the maximum initial magnetic field on the surface of the ring is equal to the critical field of a completely superconducting ring and the ring behaves externally like an *L*-*R* circuit, one may conclude by analogy with an *L*-*R* circuit that a current is flowing in the ring and that for *R* approaching zero the permanent magnetic field of a ring is due to a persistent current; its maximum value is determined by the critical magnetic field of the superconductor.

(b) The effective resistance of the thin copper foil increased with respect to the thick foil by approximately 16% for the Pb-Cu system and by 36% for the In-Cu system. The absolute value of the resistivity increased by a factor of 2.1 for the Pb-Cu rings and by 18.5 for the In-Cu samples. Because the "thick" and the "thin" copper foils are only 12.6 and 6.2 times larger than the mean free path of the electrons in the bulk material one would expect to get scattering at the boundary surfaces between the normal and superconducting material. If one assumes that such scattering surfaces exist, and if the electrons in the normal metal are scattered at the normal-superconducting boundaries only, and if one also assumes that the increase in resistivity of the insert is the same as that of a "thick" film, then one can estimate  $\rho/\rho_0$  from (Fuchs 1938; Wilson 1954):

$$(2) \quad \frac{\rho_0}{\rho} \simeq 1 - \frac{3 l_0}{8 t}$$

where  $l_0$  is the mean free path in the bulk and  $t$  is the thickness of the insert. For  $l_0 = 1.01 \times 10^{-3}$  cm and  $0.855 \times 10^{-3}$  cm for the bulk material of the "thick" and "thin" foils, respectively, one obtains  $\rho/\rho_0 = 1.033$  and 1.069. This checks barely with the Pb-Cu samples and not at all with the In-Cu rings (see Table I). Experimentally the ratios are always larger than the calculated values. However,  $\rho/\rho_0$  increases for the thinner foil as expected from eq. (2). Equation (2) takes into consideration only the scattering inside the Cu insert. It neglects scattering at the boundary surface when the electrons are in the superconducting material. The increase in  $\rho/\rho_0$  is experimentally very much larger for the In-Cu rings as compared with the Pb-Cu samples and this is probably due to some barrier effect but it is not clear why there is such a large discrepancy.

The Pb-Cu samples showed a small but definite increase in resistivity at 3.4° K. Gerritson and Linde (1951) found for silver and gold manganese alloys

that the resistance after passing through a minimum passes through a subsequent maximum at some lower temperature and falls once more with reduction of temperature. Mendoza and Thomas (1951) observed only a resistance minimum in copper alloys. The resistance of the above Cu foil was constant between 1.3° K and 4.3° K when measured separately. However, in the Pb-Cu rings a resistance maximum appeared. Similarly for the In-Cu samples the effective resistance was temperature dependent and decreased with decreasing temperatures (Fig. 4). No interdiffusion data of the above metals could be found in the literature and any effect due to interdiffusion has been neglected in the above considerations. Because electron-scattering processes at low temperatures are not very well understood the present results are of considerable interest.

(c) When a current is induced in a ring composed of a superconductor apart from a small insert of normal metal perpendicular to the current flow, then the maximum initial current which can be induced in the ring is the same as the maximum persistent current in an entirely superconducting ring of the same dimensions and the same superconducting material provided the bulk of the ring is in the superconducting state.

(d) If the electrical contact on both sides of the insert are of good quality, then the decay of the magnetic field due to the current in the ring is exponential.

(e) However, if the electrical contacts are not of good quality on both sides of the normally conducting insert, the rate of decay of the magnetic field is initially larger and then decreases (Fig. 5). For one sample the initial time constant is approximately the same for 4.23° K and 1.33° K, the second time constant increases for decreasing temperatures. For these samples the initial current was the critical current. The effective resistance of the above rings was decreasing for decreasing currents and the decrease was larger for lower temperatures. The only explanation of the two time constants could be due to the rectifying effect of small patches of copper oxide on both sides of the insert (they were not visible to the naked eye) which are likely to occur. Groetzinger, Schneider, and Schwend (1956) showed that rectification between a superconductor and a semiconductor does exist at low temperatures. Bedard and Meissner (1956) measured the contact resistance between normal and superconducting metals when they were separated by their natural oxide layers. They found that two of their samples showed rectification at low currents. An oxide layer shows barrier rectification only if it is of the order of 100 Å or thicker. Very thin oxide layers show rectification because of the tunnel effect of the electrons. If one assumes that the copper insert and the oxide layers on both sides of the foil can be represented by two rectifiers back to back\* connected by the resistance of the insert, then the combined voltage-current characteristic of this assembly is able to explain the decrease in resistance with decreasing current and also the fact that when the current is reversed the same galvanometer deflections are obtained. The decrease of the resistance with decreasing temperatures is consistent with the above picture

\*I am grateful to Professor R. E. Burgess for suggesting this explanation.

and it also explains the increase in resistance with increasing currents in Bedard and Meissner's experiments.

#### ACKNOWLEDGMENTS

The author wishes to acknowledge many helpful discussions with Professor R. E. Burgess and Professor J. B. Brown. Thanks are due to Mr. H. H. M. Zerbst for his help in performing the experiments and preparing the drawings. The author also wishes to thank the National Research Council, Canada, for a studentship and for the support received.

#### REFERENCES

BEDARD, F. and MEISSNER, H. 1956. *Phys. Rev.* **101**, 26.  
CHAMBERS, R. G. 1950. *Nature* **165**, 239. See also *Handbuch der Physik*, **XIV**, 188 (1956).  
FUCHS, K. 1938. *Proc. Cambridge Phil. Soc.* **34**, 100.  
GERRITSEN, A. N. and LINDE, J. O. 1951. *Physica*, **17**, 573, 584.  
— 1952. *Physica*, **18**, 877.  
GROETZINGER, G., SCHNEIDER, J., and SCHWEND, P. 1956. *Bull. Am. Phys. Soc. Ser. II*, **1**, 58.  
KIKOIN, I. K. and GOBAR, S. V. 1936. *Compt. rend. acad. sci. U.R.S.S.* **19**, 249.  
— 1940. *J. Phys. U.S.S.R.* **3**, 333.  
VON LAUE, M. 1949. *Theorie der Superleitung*, Vol. 2 (Springer-Verlag), Chap. 8.  
LONDON, F. 1950. *Superfluids*, Vol. I (John Wiley & Sons, Inc.), p. 37.  
MACDONALD, D. K. C. 1956. *Handbuch der Physik*, **XIV**, 185.  
MENDOZA, E. and THOMAS, J. G. 1951. *Phil. Mag.* **42**, 291.  
PRY, R. M., LATHROP, A. L., and HOUSTON, V. 1952. *Phys. Rev.* **86**, 905.  
SHOENBERG, D. 1952. *Superconductivity* (Cambridge University Press), p. 30.  
SMYTHE, W. R. 1950. *Static and dynamic electricity* (McGraw-Hill Book Co.), p. 271.  
WILSON, A. H. 1954. *The theory of metals*, 2nd ed. (Cambridge University Press), p. 242.

# THE DESTRUCTION OF SUPERCONDUCTIVITY IN TANTALUM WIRES BY A CURRENT<sup>1</sup>

H. J. FINK

## ABSTRACT

The transition from the superconducting to the normal state of various pre-stretched tantalum wires carrying current was investigated. When the resistance of the wire jumps discontinuously from the superconducting to the normal or intermediate state as a current is passed through it, then this current is defined as the critical current  $I_c$ . For temperatures  $T < (T_c - 5 \text{ millidegrees K})$  the resistance of the wire jumps directly from zero resistance to its normal value at the critical current, such that the total cross section of the wire goes effectively into the normal state. Between  $(T_c - 5 \text{ millidegrees K})$  and  $T_c$  the resistance of the wire jumps at  $I_c$  to any fraction of the normal resistance between approximately zero and one. For constant temperatures the resistance-current plots show a large hysteresis effect. The transition temperature,  $T_c$ , of the various samples is strongly dependent upon their normal resistivity at helium temperatures. If the wires with a small constant current (4.2 ma) flowing in them are cooled from above the transition temperature, the resistance decreases above  $T_c$  and approaches zero at approximately  $T_c$ , where  $T_c$  is defined by the extrapolation of the  $I_c - T$  curve to  $I_c = 0$ . If the wires are heated from below  $T_c$  the same resistance-temperature curves are reproduced.

## 1. INTRODUCTION

When a current is passed through a superconducting wire, then a resistance appears when the magnetic field at the surface of the wire reaches the critical field,  $H_c$ . This is Silsbee's hypothesis (Silsbee 1916) and it has been experimentally verified by a number of authors (Scott 1948; Rinderer 1956).

London (1937) showed that for  $I \geq I_c$  a core in the wire must exist which can be neither normal nor superconducting but must be in the intermediate state. Assuming (a) the intermediate state exists in a core where the magnetic field at any point is equal to  $H_c$ , (b) the current density is continuous at the boundary surface of the core (which is in the intermediate state) and the normal conducting shell, and (c) the electric field is constant over the total cross section of the wire, one is able to find an expression for the increase of resistance  $R$  with current  $I$ :

$$(1) \quad R/R_n = (1/2)[1 + \sqrt{1 - (I_c/I)^2}] \quad \text{for } I \geq I_c,$$

where  $R_n$  is the resistance of the wire in the normal state. When the current approaches the current  $I_c$  as defined above, the resistance of the wire should jump abruptly to  $1/2 R_n$  and for very large currents approach the value  $R_n$  asymptotically. The above assumptions do not specify anything about the detailed structure of the intermediate state, but London (1950) assumes that the core consists of superconducting and normal disks perpendicular to the current flow in the wire.

<sup>1</sup>Manuscript received November 17, 1958.

Contribution from the Department of Physics, University of British Columbia, Vancouver, B.C.

Kuper (1952) employs London's suggestion of a disk-like intermediate state core. He derives an expression for  $R/R_n$ , assuming that the thickness of the normal disks is small compared with the mean free path of the electrons in the normal state. The electrons are scattered on the interfaces between the normal and superconducting disks and this increases the resistance  $R$ . The initial jump of  $R/R_n$  for  $I = I_e$  is no longer  $1/2$  but larger. He also assumes that distortions of the electron path do not change the resistance (only the Gibb's function), that the surface energy does not change the Gibb's function very much, and that the singularities of London's model on the axis of the wire may be neglected. With these assumptions and some approximations Kuper obtains the following expression:

$$(2) \quad R/R_n = (1/2) \left( 1 + \sqrt{1 - \left( \frac{I_e}{I} \right)^2 \left[ 1 - \frac{2I}{I_e y} \left\{ 1 - \exp \left( -\frac{y I_e}{2I} \right) \right\} \right]} \right) \quad \text{for } I \geq I_e,$$

where  $y = a/l$ ,  $a$  is the radius of the cylindrical wire,  $l$  is the mean free path of the electrons. Therefore at  $I = I_e$  the resistance ratio  $R_e/R_n$  is a function of  $y$ . For  $y = 0$ ,  $R_e/R_n = 1$  and for  $y = \infty$ ,  $R_e/R_n = 1/2$ . Hence metals in which the mean free path of the electrons is very small compared with the radius of the wire should satisfy eq. (1). In the present experiments  $y$  is large compared with previous experiments.

Gorter's model (Gorter 1957) is a dynamic model which employs the phenomenon of supercooling of the normal phase. In the intermediate state the boundaries between the superconducting and normal phase are assumed to be parallel to the current. These boundaries would move continuously in the direction perpendicular to the (constant) current and the local magnetic field and the voltage drop observed in the direction of the current flow would be due to induction. If one assumes that the normal phase persists when the magnetic field falls below the critical value  $H_c$  and that an intermediate state mixture is set up everywhere  $H < H_c$  if the field has fallen to a value  $q_r H_c$  in the normal phase ( $q_r$  is a parameter smaller than 1), then the critical resistance is approximately 0.7 of the normal resistance (for  $0.75 \leq q_r \leq 1.0$ ). The supercooling introduces periodicity into the dynamic model and Gorter and Potters (1958) have made some numerical calculations of the velocity of the phase boundary, the upper limit of the amplitudes of the voltage variations, and their frequency. In the above model the heat of transformation and the surface energy between the normal and superconducting phase have been neglected.

The first conclusive investigations concerning the transition from the superconducting to the normal state were performed by Schubnikow and Alekseyevsky (1936) and Alekseyevsky (1938). They observed that  $R_e/R_n \approx 0.8$  at  $1.95^\circ\text{K}$  for a polycrystalline tin wire of radius 0.0056 cm and a monocrystalline wire of radius 0.0080 cm. At approximately  $2I_e$  the resistance of the wire approaches  $R_n$  in contradiction with eq. (1) and (2). They estimated the temperature rise due to current heating inside the wire to approximately  $10^{-4}^\circ\text{K}$ .

Scott (1948) performed some experiments on polycrystalline indium wires of radius 0.005, 0.014, and 0.0175 cm between  $3.34^\circ\text{K}$  and  $3.38^\circ\text{K}$ . He

estimates that the temperature rise due to the heating effect of the current has no influence upon  $R_e/R_n$ , and he finds that  $R_e/R_n$  is 0.85, 0.79, and 0.77 for the wire of radius 0.005, 0.014, and 0.0175 cm respectively in the above temperature range. He also verifies Silsbee's hypothesis. Scott's results do not satisfy eq. (1) but they fit eq. (2) with  $l = 2.4 \times 10^{-3}$  cm.

Rinderer (1956) investigated tin wires of various impurity content of radius 0.0375 cm between  $T_e = 3.72^\circ$  K and  $3.27^\circ$  K. He estimates the maximum temperature rise for his purest sample to approximately  $3 \times 10^{-4}^\circ$  K. He confirms Silsbee's hypothesis. He finds that his purest sample satisfies approximately eq. (1); however,  $R_e/R_n$  is temperature dependent as well as dependent upon the impurity content of his samples. His samples satisfy eq. (2) only qualitatively.  $R_e/R_n$  increases with increasing  $y$  by varying the impurity content in contradiction with Kuper's theory. For currents smaller than 4 amperes the transition becomes continuous. He states that the impurity content of his samples is responsible for the continuous transition.

## 2. EXPERIMENTAL PROCEDURE AND RESULTS

The present experiments were designed to test London's and Kuper's equation for large  $y$ . Various experiments were performed on tantalum wires of radius 0.0127 cm and 0.00635 cm. The wires were purchased from the Fansteel Metallurgical Corporation, North Chicago. According to specification they were stretched 15, 21, 22% and annealed. The impurity content was not known. Therefore it was decided to perform some metallurgical tests in order to find the relative strain and impurity content of the above three different samples. Three pieces of each wire were mounted in bakelite at approximately  $160^\circ$  C, polished, and etched with hydrofluoric acid. The shape of the grains was studied under the microscope and they were found to be equiaxed for all three samples. This implies that if there were any strains in the metal, those strains must be very small. Then another four pieces of wire were mounted in bakelite mounts and metallographically polished. These four pieces of each wire were tested in triplicate microhardness measurements using a  $136^\circ$  square pyramid diamond penetrator and a 200-g load. The diamond pyramid hardness (D.P.H.) is defined as the load per unit area of surface contact in kilograms per square millimeter. Table I shows that for sample 3 the D.P.H. is the smallest and that the D.P.H. increases as the normal resistivity at helium temperatures. Assuming that the strain in the wires may be neglected, sample 3 appears to be the purest because generally

TABLE I  
Length, radius, stretch, resistance, and diamond pyramid hardness of samples

Sample	Length CD, cm	Radius, cm	Stretch, %	$R_{300}$ , ohms	$R_n/R_{300}$	$\rho_n$ at $4.4^\circ$ K, ohm-cm	D.P.H.
1	13.6	$12.7 \times 10^{-3}$	22	0.412	0.112	$1.72 \times 10^{-6}$	192
1a	2.37	$12.7 \times 10^{-3}$	22	0.0722	0.119	$1.89 \times 10^{-6}$	192
2	1.61	$6.35 \times 10^{-3}$	15	0.222	0.175	$3.05 \times 10^{-6}$	204
3	1.38	$12.7 \times 10^{-3}$	21	0.039	0.0703	$1.00 \times 10^{-6}$	167

the hardness increases with increasing impurity content. The resistivity of the tantalum is fairly large at 300° K (see Table I) as well as the normal resistivity at helium temperatures compared with tin and indium. This has the advantage that one can measure the resistance of the samples fairly accurately for small currents (near the transition temperature) with conventional methods. For the measurement of the resistance of the above samples a standard current-voltage method was used. The current and voltage leads were copper and were spot-welded to the tantalum wire.

Figure 1 shows the plot of the critical current versus the temperature difference ( $T - T_c$ ). The values of  $T_c$  are compiled in Table II. The transition temperatures increase strongly with decreasing  $R_n/R_{300}$ . For sample 2, two

TABLE II  
Transition temperature, slope at  $T_c$ , external applied field, and noise of samples

Sample	$T_c$ °K	Slope at $T = T_c$ , oersted/°K	$H_{\text{external}}$	Maximum noise ampli- tude per unit length in CD, $\mu\text{v/cm}$
1	4.232 <sub>8</sub>		Earth mag. field	$\sim \pm 10$
1a	4.221 <sub>6</sub>		0	$\sim \pm 20$
2	4.109 <sub>5</sub>	-276	Earth mag. field	$\sim \pm 30$
2	4.109 <sub>7</sub>	-320	0	$\sim \pm 100$
3	4.323 <sub>0</sub>	-334	0	$\sim \pm 20$

separate experiments were performed: one with the magnetic field of the earth compensated, the other without compensation. Between these experiments the sample was kept at room temperature for about a week. The

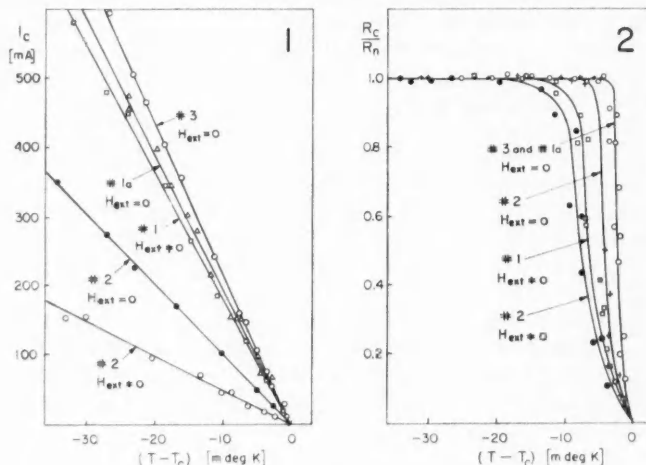


FIG. 1. Critical current vs. temperature difference  $T - T_c$ .  
FIG. 2.  $R_n/R_c$  versus temperature difference  $T - T_c$ .

difference in  $T_c$  is remarkably small. For samples 1a, 2, and 3 the magnetic field of the earth was compensated to less than 1% of its value with two Helmholtz coils 34 and 24 cm in diameter. Sample 2 and sample 1 were measured in the magnetic field of the earth. The samples were suspended vertically. The vertical component of the magnetic field of the earth was approximately .55 oersted and the horizontal component .20 oersted. The measurements for the uncompensated magnetic field of the earth are rather a complex case of superposition of a longitudinal and transverse field, and the field due to the current which is of the same order of magnitude as the magnetic field of the earth for small current values.

Figure 2 shows a plot of  $R_e/R_n$  versus temperature for the above samples. The transition temperatures determined from the  $I_c$  versus temperature plot are not of basic importance for the sample with uncompensated magnetic field of the earth. The value  $R_e/R_n$  approaches unity for temperatures 4 to 6 millidegrees below the transition temperature. For the samples with uncompensated magnetic field of the earth the transition bandwidth was about 15 to 20 millidegrees. For these samples the transition was sharp even for values of  $R_e/R_n < 1/2$  and no tails were observed. For increasing currents  $R/R_n$  approached unity. Figure 3a shows the resistance plotted versus the current for four different critical currents of sample 1. For example when  $R_e/R_n$  was 0.80,  $R/R_n$  approached unity at  $I/I_c = 1.3$ , and when  $R_e/R_n$  was 0.15,  $R/R_n$  approached unity at  $I/I_c = 2.7$ . For resistances smaller than  $R_n$  large voltage fluctuations were observed across the samples. Because the time constant of the galvanometer was 2 seconds and the galvanometer was under

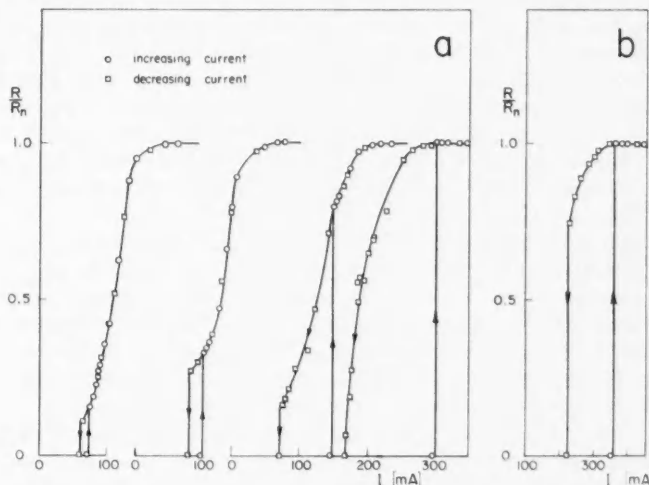


FIG. 3. (a) The resistance of sample 1 as a function of current at constant temperatures when the magnetic field of the earth was not compensated.

(b) The resistance of sample 3 as a function of current at  $T = 4.307^\circ\text{K}$  when the magnetic field of the earth was compensated.

damped, the frequencies of the fluctuations which could be observed were close to 1 c.p.s. The largest amplitudes of fluctuations were not observed at the transition but approximately at  $I/I_e = 1.1$ . Table II also shows the maximum noise voltages as observed by the galvanometer deflections. These values are only approximate. For the case of the compensated earth's magnetic field the fluctuations were narrowed to a region of approximately 4 to 6 millidegrees. The fluctuations were mostly of random nature as observed on the galvanometer, but sometimes over short periods of time the galvanometer deflections were "kicks" in one direction only. The transition points (Fig. 2) of the  $R_e/R_n$  versus  $T - T_e$  plot for  $R_e/R_n < 1$  (especially for the samples with compensated magnetic fields of the earth) are therefore accurate to 10 to 20% only. For small currents ( $< 50$  ma) the voltage fluctuations were very strong as soon as the critical current was approached. Therefore for those currents it is not clear if this initial deflection of the galvanometer at  $I = I_e$  was due to the fluctuations. However, for the samples with uncompensated earth's magnetic field the initial deflection of the galvanometer at  $I = I_e$  was due to a discontinuity in  $R/R_n$  and it is believed that the same is true when the magnetic field of the earth is compensated. With the magnetic field of the earth compensated only the resistance at  $I/I_e$  was measured. The current was then increased to approximately  $3I_e$ , the normal resistance of the wire was checked, and then the current was decreased until  $I = I_t$ , where  $I_t$  is the current when the metal goes from the normal into the superconducting state. Figure 3b shows the resistance of sample 3 plotted as a function of current at  $T = 4.307^\circ$  K.

When the current was increased above the critical current and then decreased, all the samples showed a strong hysteresis effect as observed by other investigators (Scott 1948; Rinderer 1956). For sample 3,  $I_t/I_e$  decreased linearly from approximately 0.8 at  $I_e = 100$  ma to 0.5 at  $I_e = 400$  ma. For sample 1a  $I_t/I_e$  was 0.55 at  $I_e = 100$  ma and 0.45 at  $I_e = 400$  ma. For one temperature  $I_t$  is not always exactly reproducible and the  $I_t/I_e$  values stray approximately 10%. Table II shows also the slope of the  $H_e-T$  curves at  $T = T_e$  based on the assumption that Silsbee's hypothesis holds.

The transition from the superconducting to the normal state with increasing temperature and constant current was also studied. The current was 4.2 ma for samples 1a, 2, and 3 for which the magnetic field of the earth was compensated. The smaller  $R_n/R_{300}$  the sharper is the transition (Fig. 4). Sample 3 was warmed up as well as cooled at a rate of 3 millidegrees per hour, samples 1a and 2 at a rate of 5 to 8 millidegrees per hour. The same curves were produced for cooling and heating for the above temperature drift rates, which shows that the samples were at the same temperature as the helium bath. The transition width for sample 3 was less than 2 millidegrees for a current of 4.2 ma. Sample 3 is believed to be purer than sample 1a and 1a purer than 2.

When a superconducting wire is cooled from above the transition temperature with a constant current flowing in it, then according to eq. (1) at temperature  $T_e$  the intermediate core should appear. A further reduction of the temperature will decrease the resistance. The core will grow until it occupies the whole wire. Then the resistance will drop suddenly and go into the super-

conducting state. However, this picture is not consistent with the present experiment. The extrapolation of the  $I_c$ - $T$  curves toward the temperature axis defines  $T_c$ . The origin of Fig. 4 is taken at  $T_c$ . This  $T_c$  is at  $R/R_n \simeq 0$  and not at  $R/R_n = 1$  as implied by eq. (1). The breadth of the transition is

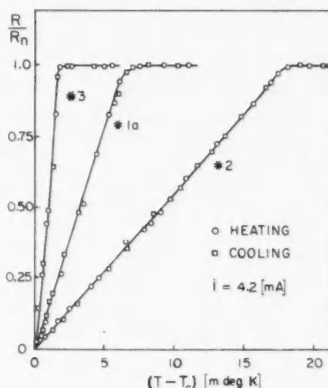


FIG. 4.  $R/R_n$  vs. temperature difference  $T - T_c$  for  $I = 4.20$  ma.

probably due to impurities and strains (de Haas and Voogd 1931), but there is no satisfactory explanation why the resistance of the wires begins to decrease above the transition temperatures.

It was fairly easy to keep the temperature constant with two needle valves in series. Above  $4^\circ$  K a temperature change of 1 millidegree corresponds approximately to a change in helium vapor pressure of 1 mm of mercury. No other temperature-regulating devices were used. The temperature was determined from the vapor pressure of helium read on a mercury manometer with a cathetometer and the 1948 temperature scale was used.

### 3. UNCERTAINTIES

The temperature was kept constant for most measurements between 1 and 2 millidegrees, except for the measurements of Fig. 4 where the resistance readings correspond to temperature readings to better than half a millidegree. The over-all accuracy of the resistance measurement was 2% or better. The values of the diamond pyramid hardness test strayed by approximately  $\pm 3\%$ .

The error in temperature due to the static pressure of the liquid helium was smaller than  $10^{-3}^\circ$  K and was neglected.

As soon as a resistance appears the wire will be heated due to the dissipation of electric energy. The increase in temperature of the wire  $\Delta T$  can be separated into two terms  $\Delta T = \Delta T_1 + \Delta T_2$ , where  $\Delta T_1$  is the increase in temperature at the axis of the wire relative to the surface and it will depend upon the thermal conductivity  $K$  of the wire.  $\Delta T_2$  is the temperature difference between the

helium bath and the surface of the wire and it will depend upon the thermal contact resistance  $\alpha$ .

$$(3) \quad \Delta T = \frac{Q}{2\pi} \left( \frac{1}{2K} + \frac{1}{a\alpha} \right),$$

where  $Q$  is the dissipated energy in watts/cm length of the wire, and  $a$  is the radius of the wire. The first term does not contain any correction for an intermediate state core. For the smallest currents which make  $R_e/R_n \simeq 1$ ,  $Q$  varies from approximately  $2 \times 10^{-5}$  to  $10 \times 10^{-5}$  watts/cm length of the wires. From Hulm's (1950) measurements on 0.1% impure tantalum at  $4.1^\circ$  K the thermal conductivity  $K = 48.2 \times 10^{-3}$  watts/cm deg K. The measurements of Mendelssohn and Olsen (1950) and Mendelssohn and Rosenberg (1952) give considerably larger values for 99.95% and 99.98% pure tantalum respectively. With the above smaller value for  $K$  the temperature rise  $\Delta T_1$  of the above samples varies from  $6.6 \times 10^{-5}$  K for sample 3 to  $3.4 \times 10^{-4}$  K for sample 2. Only the second term of eq. (3) is of importance and there is no value of the thermal contact resistance for tantalum and helium I in the literature. If one takes the value of  $\alpha$  for tin and helium I at  $4.1^\circ$  K as  $\sim 1.5$  watts/cm<sup>2</sup> deg K (Rinderer 1956), then  $\Delta T_2$  is of the order of  $10^{-4}$  K for samples 1a and 3, and  $1.7 \times 10^{-3}$  K for sample 2 at the above currents. Sample 2 would then have an error of larger than 2 millidegrees for current values larger than 65 mA. For smaller current values  $R_e/R_n < 1$  and in this range the increase in temperature can be neglected compared with the accuracy of the temperature measurements. If one compares samples 2 and 3, one finds that  $R_e/R_n$  approaches unity when the dissipation of heat due to the current of sample 2 is five times larger than that of sample 3. This shows that the increase in  $R_e/R_n$  above 1/2 according to eq. (1) is not due to overheating of the samples.

#### 4. DISCUSSION

(a) For temperatures smaller than 5 millidegrees below the transition temperature  $R_e/R_n$  is essentially unity for the samples used above. The normal resistivity for these samples at helium temperatures was relatively large and from this one may conclude that the mean free path of the electrons at this temperature is small. Because no data for the mean free path of tantalum at helium temperatures can be found in the literature the mean free path is estimated from the Fermi energy at absolute zero. Because

$$E_F = \frac{\hbar^2}{2m} \left( \frac{3n}{8\pi} \right)^{2/3} = \frac{mv_F^2}{2} \quad \text{and} \quad \rho = \frac{mv_F}{ne^2 l},$$

one gets

$$\rho l = \frac{\hbar}{e^2} \left( \frac{3}{8n^2} \right)^{1/3},$$

where  $n$  is the number of free electrons per unit volume,  $\rho$  the bulk resistivity of the metal, and  $l$  the mean free path of the electrons. Because tantalum has five valence electrons per atom,  $\rho l \simeq 3 \times 10^{-12}$  ohm-cm<sup>2</sup>. For the above samples

the mean free path is then of the order of  $10^{-6}$  cm. The ratio  $a/l$  is plotted versus  $R_e/R_n$  in Fig. 5. However, some authors assume that only one electron per atom contributes to the conductivity of multivalent metals. Therefore for  $n = 1$  the values of  $y$  for Ta in Fig. 5 have to be divided by 2.9. Figure 5 shows that neither eq. (1) nor eq. (2) is satisfied. Kuper's equation requires a modification for large ratios of  $a/l$ .

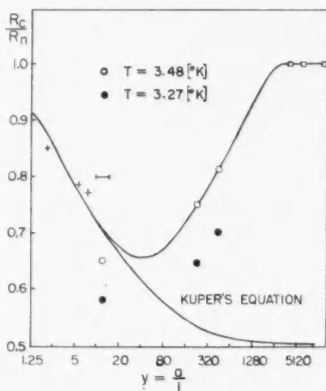


FIG. 5.  $R_e/R_n$  vs.  $a/l$ . + results by Scott on indium (estimated by Kuper), |—| results by Alekseyevsky on tin, ○ results by Rinderer on tin, □ results on tantalum.

(b) The ratio of  $R_e/R_n$  close to the transition temperature is believed to have any value from zero to one. However, over this narrow temperature range (5 millidegrees) no conclusive results can be derived because of large low-frequency voltage fluctuations which made accurate resistance measurements impossible. These fluctuations are probably due to the instability of the intermediate state over part of the cross section of the wire. The observed voltage fluctuations are not that predicted by Gorter and Potters (1958). According to their model the lowest frequencies one should expect for the above samples are of the order of  $10^6$  to  $10^7$  c.p.s. for  $H/H_e = 1.1$ . Voltage fluctuations in the intermediate state of Ta were previously observed by Webber (1947) and Kaplan and Daunt (1955) and studied by Baird (1958, 1959). Near the transition temperature the resistance of the samples is varying strongly with temperature and one could imagine that local temperature variations and minor fluctuations in the supply current give rise to magnified voltage fluctuations across the wires. For current values corresponding to  $R_e/R_n = 1$ , the voltage fluctuations will not be magnified, because local temperature variations in the samples will not change the resistance of the metal and hence no magnification will occur. Although the magnetic field of the earth was compensated to better than 1%, the stray magnetic field due to the current in the current leads of the samples made probably the above compensation not better than 2%. Because the transition bandwidth in Fig. 2

decreases for decreasing magnetic field it is likely that Fig. 2 approaches a step function for no stray magnetic fields at all.

(c) For constant temperature a marked hysteresis loop was observed when the current was increased to and decreased from above the critical current. When the resistance of the wire jumps from the normal into the superconducting state the currents were only reproducible within 10%. However, for increasing  $I_e$ 's the area underneath the hysteresis loop increased also. For equal  $I_e$ 's the purer sample (sample 3) showed generally a smaller area underneath the loop compared with sample 1a. If one makes supercooling alone responsible for the hysteresis effect, then it is not obvious why the purer sample has a smaller area. One would expect that impurities favor the growth of nuclei of the stable phase. Probably the magnetic field of the current and inhomogeneities in the metal are partly responsible for the hysteresis effect.

(d) The transition temperatures decreased markedly with increasing resistivity of the samples at helium temperatures; the difference between samples 3 and 1a is more than 200 millidegrees K. According to the theory of superconductivity by Bardeen, Cooper, and Schrieffer (1957) the transition temperature,  $T_e$ , is given by:

$$kT_e = 1.14(\hbar\omega) \exp(-1/N(0)V)$$

where  $(\hbar\omega)$  is the average phonon energy,  $N(0)$  is the density of Bloch states of one spin per unit energy at the Fermi surface, and  $V$  is the average of the sum of the attractive phonon interaction and the repulsive Coulomb interaction. The criterion of the above theory is that the attractive part of  $V$  dominates the repulsive. Because tantalum has only one stable isotope, the difference in  $T_e$  of the various samples cannot be due to the isotope effect.  $N(0)$  as well as  $V$  could be affected by impurities, and strains in the metal would change the vibrational spectrum of the lattice and hence  $(\hbar\omega)$ . Pines (1958) estimates  $N(0)V = 0.296$  for Ta under the assumption that  $\hbar\omega = k\theta_D/2$ , where  $\theta_D$  is the Debye temperature. However, the present state of the theory does not allow any quantitative calculations of the changes of the above three quantities with impurities and strain and, therefore, one cannot estimate which quantity is dominant in this experiment.

(e) When a prestretched tantalum wire is cooled from above the transition temperature with a small constant current (4.2 ma) flowing in it, then the resistance decreases above the transition temperature and approaches zero at  $T \simeq T_e$ , where  $T_e$  is defined by the extrapolation of the  $I_e-T$  curve to  $I_e = 0$ . When a prestretched tantalum wire is heated from below the transition temperature with a small constant current flowing in it, then at approximately the transition temperature a small resistance appears and the resistance approaches its normal value well above the transition temperature.

#### ACKNOWLEDGMENTS

The author is indebted to Professor R. E. Burgess and Dr. J. B. Brown for their advice and encouragement in these experiments. Special thanks are due to Dr. V. Griffiths, who supplied two of the Ta samples; to Mr. A. W. Greenius

from the British Columbia Research Council, who performed the micro-hardness tests; and to Mr. H. H. M. Zerbst, who prepared the drawings. The author wishes to thank the National Research Council, Canada, for a studentship and for the support of the project.

## REFERENCES

ALEKSEYEVSKY, N. E. 1938. *J. Exptl. Theoret. Phys. U.S.S.R.* **8**, 342.  
BAIRD, D. C. 1958. *Can. Met. Phys. Conf.*, Queen's Univ., Kingston, 3-5 Sept.  
——— 1959. *Can. J. Phys.* **37**, 129.  
BARDEEN, J., COOPER, L. N., and SCHRIEFFER, J. R. 1957. *Phys. Rev.* **108**, 1175.  
GORTER, C. J. 1957. *Physica*, **23**, 45.  
GORTER, C. J. and POTTERS, M. L. 1958. *Physica*, **24**, 169.  
DE HAAS, W. J. and VOOGD, J. 1931. *Commun. Phys. Lab. Univ. Leiden*, **214c**.  
HULM, J. K. 1950. *Proc. Roy. Soc. (London)*, A, **204**, 98.  
KAPLAN, B. and DAUNT, J. G. 1955. *Phys. Rev.* **89**, 907.  
KUPER, C. G. 1952. *Phil. Mag.* **43**, 1264.  
LONDON, F. 1937. *Une conception nouvelle de la supraconductibilité* (Herrmann & Cie, Paris).  
——— 1950. *Superfluids*, Vol. I (John Wiley & Sons, Inc.), p. 120.  
MENDELSSOHN, K. and OLSEN, J. L. 1950. *Proc. Phys. Soc. (London)*, A, **63**, 2.  
MENDELSSOHN, K. and ROSENBERG, H. M. 1952. *Proc. Phys. Soc. (London)*, A, **65**, 388.  
PINES, D. 1958. *Phys. Rev.* **109**, 280.  
RINDERER, L. 1956. *Helv. Phys. Acta*, **29**, 339.  
SCHUBNIKOW, L. W. and ALEKSEYEVSKY, N. E. 1936. *Nature*, **138**, 804.  
SCOTT, R. B. 1948. *J. Research Natl. Bur. Standards*, **41**, 581.  
SILSBE, F. B. 1916. *J. Wash. Acad. Sci.* **6**, 597.  
WEBBER, R. T. 1947. *Phys. Rev.* **72**, 1241.

## NORMAL GRAIN GROWTH IN ZONE-REFINED HIGH-PURITY METALS<sup>1</sup>

E. L. HOLMES AND W. C. WINEGARD

### ABSTRACT

Comparisons are made between theoretical and experimental rates of boundary migration during grain growth in zone-refined metals; these indicate that a single-atom process is involved. A model is proposed for the mechanism of grain-boundary migration based on the assumption of a single-atom process and the fact that the energies of activation for grain growth, both in zone-refined lead and tin, are similar to the energy barrier to be overcome by an atom in transferring from the solid to the liquid state during melting.

### INTRODUCTION

The similarity between the experimental activation energies for grain growth in zone-refined lead (1958) and tin (1959), and the activation energies for liquid self-diffusion in these metals, has been noted by Holmes and Winegard (1959). The calculated free energies of activation for grain growth, grain-boundary self-diffusion, and liquid self-diffusion were also found to be similar. No attempt was made at that time to suggest a definite mechanism for boundary migration or to really establish that a single-atom process was involved. In the present paper, comparisons are made between the experimental rates of boundary migration and the calculated rates assuming both a single-atom process and a group-type mechanism. On the basis of a single-atom process, a mechanism of grain-boundary migration is proposed.

### COMPARISON BETWEEN THEORETICAL AND EXPERIMENTAL RATES OF MIGRATION

Following the treatment of Cole, Feltham, and Gilliam (1954), the rate of grain-boundary migration assuming a single-atom process may be expressed as

$$(1) \quad V = \frac{2\nu b}{kT} \Delta F \exp\left(-\frac{Q}{RT}\right)$$

where  $V$  is the rate of boundary migration,

$\nu$  is the frequency of atomic jumps,

$b$  is the distance moved forward locally by the boundary as an atom transfers from one grain to an adjoining grain, i.e., one atomic diameter, taken as  $2.5 \text{ \AA}$ ,

$Q$  is the activation energy for grain-boundary migration,

$\Delta F$  is the free energy per atom available for migration, taken as  $2b^3\sigma/r$

$r$  is taken as average grain diameter, as indicated by a surface count.

<sup>1</sup>Manuscript received December 9, 1958.

Contribution from the Department of Metallurgical Engineering, University of Toronto, Toronto, Ontario.

$\sigma$  is the specific grain-boundary free energy, taken as 200 ergs  $\text{cm}^{-2}$  for lead and as 100 ergs  $\text{cm}^{-2}$  for tin, as estimated by Aust and Chalmers (1951, 1950).

The values of the rates calculated from equation (1) are compared with the experimental values, at various temperatures, in Table I.

TABLE I  
Comparison between theoretical and experimental rates of boundary migration

Metal	Temperature, $^{\circ}\text{C}$	Observed rate, $\text{cm sec}^{-1}$	Calculated rate		Source of experimental results
			Based on single- atom process theory, $\text{cm sec}^{-1}$	Based on group- process theory, $\text{cm sec}^{-1}$	
Lead	318	$6.2 \times 10^{-4}$	$11.0 \times 10^{-4}$	$16 \times 10^{-4}$	Bolling and Winegard (1958)
	251	$4.2 \times 10^{-4}$	$7.5 \times 10^{-4}$	$11 \times 10^{-4}$	
	168	$2.7 \times 10^{-4}$	$3.3 \times 10^{-4}$	$5 \times 10^{-4}$	
Tin	220	$8.4 \times 10^{-4}$	$7.0 \times 10^{-4}$	$4.1 \times 10^{-4}$	Holmes and Winegard (1959)
	200	$7.0 \times 10^{-4}$	$2.8 \times 10^{-4}$	$3.7 \times 10^{-4}$	
	180	$6.0 \times 10^{-4}$	$2.5 \times 10^{-4}$	$3.3 \times 10^{-4}$	
	167	$5.7 \times 10^{-4}$	$2.3 \times 10^{-4}$	$3.0 \times 10^{-4}$	

Also shown in Table I are the rates of boundary migration calculated on the basis of the group-process theory of Mott (1948) whereby it is suggested that a group of " $n$ " atoms in one crystal "melt" and then "resolidify" on to the adjoining crystal yielding a rate

$$(2) \quad V = \frac{2vb}{kT} n \Delta F \exp \left[ \frac{Q}{R} \left( \frac{1}{T_M} - \frac{1}{T} \right) \right].$$

The value of  $n$  is determined by the fact that  $nL$  ( $L$  is the latent heat of melting per g-atom) =  $Q$ , the observed activation energy, and  $T_M$  is the melting temperature.

It is clear from Table I that reasonable agreement exists between the experimental rates and the rates calculated on the basis of a single-atom process. This agrees with the recent results of Aust and Rutter (1959) on single grain-boundary migration in zone-refined lead.

#### COMPARISON BETWEEN GRAIN GROWTH AND MELTING

Jackson and Chalmers (1956) have suggested the possibility that the same energy barriers that limit the movement of atoms in liquid self-diffusion control the movement of atoms from liquid to solid during freezing, and thus it might be expected that the activated state for the two processes should be the same. A similar proposal has also been made by Frenkel (1946). Jackson and Chalmers (1956) then suggest that the activation energy for freezing is equal in magnitude to the activation energy for liquid self-diffusion  $Q$ , and that the activation energy for melting, i.e., the energy barrier to be overcome in transferring an atom from solid to liquid, is approximately equal

to the sum of the latent heat of fusion and the activation energy for liquid self-diffusion.

From the above considerations, the values of the activation energy for melting for lead and tin would be approximately 5.75 kcal/g-atom and 5.7 kcal/g-atom respectively, taking  $Q$  as 4.55 kcal/g-atom for lead (Rothman and Hall 1956) and 4.0 kcal/g-atom for tin (Careri and Paoletti 1955). It is immediately apparent that the values for the activation energy of melting are similar in magnitude to the values  $6.7 \pm 0.7$  kcal/g-atom and  $6.0 \pm 0.6$  kcal/g-atom obtained as the activation energies for grain growth in zone-refined lead (1958) and tin (1959).

#### CONCLUSION

On the basis of (a) the evidence that a single-atom process is involved and (b) the similarity in magnitude between the activation energy for grain growth in zone-refined materials and the activation energy for "melting", as proposed by Jackson and Chalmers (1956), it is suggested that the mechanism of grain growth in high-purity zone-refined metals is similar to that whereby an atom is transferred from the solid to the liquid during melting.

It should be noted that the above considerations are limited to random high-angle boundaries for which the grain growth results apply.

#### ACKNOWLEDGMENTS

The authors are grateful to the Defence Research Board of Canada (Grant No. 9535-01) for financial support. One of the authors (E.L.H.) received an International Nickel Co. Fellowship during the course of some of this work. The helpful discussions and constructive criticisms offered by Dr. J. W. Rutter and Dr. K. T. Aust of the General Electric Co., Schenectady, are gratefully acknowledged. The staff and graduate students of the Department of Metallurgical Engineering of the University of Toronto are to be thanked for their interest and stimulating discussions.

#### REFERENCES

AUST, K. T. and CHALMERS, B. 1950. Proc. Roy. Soc. (London), A, **201**, 210.  
— 1951. Proc. Roy. Soc. (London), A, **204**, 359.  
AUST, K. T. and RUTTER, J. W. 1959. To be published.  
BOLLING, G. F. and WINEGARD, W. C. 1958. Acta Met. **6**, 283.  
CARERI, A. and PAOLETTI, G. 1955. Nuovo cimento, **2** (10), 574.  
COLE, D. G., FELTHAM, P., and GILLIAM, E. 1954. Proc. Phys. Soc. (London), B, **67**, 131.  
FRENKEL, J. 1946. Kinetic theory of liquids (Oxford University Press), p. 415.  
HOLMES, E. L. and WINEGARD, W. C. 1959. Acta Met. To be published.  
JACKSON, K. A. and CHALMERS, B. 1956. Can. J. Phys. **34**, 473.  
MOTT, N. F. 1948. Proc. Phys. Soc. (London), **60**, 391.  
ROTHMAN, S. J. and HALL, L. D. 1956. Trans. Am. Inst. Mining Met. Engrs. **206**, 199.

## ABSOLUTE $\beta$ -COUNTING IN A PROPORTIONAL FLOW-COUNTER<sup>1</sup>

J. P. ROALSVIG AND R. N. H. HASLAM

### ABSTRACT

Self-absorption and backscattering of  $\beta$ -particles have been studied in a proportional flow-counter, and empirical formulae are obtained to correct for these factors in absolute  $\beta$ -counting. The correction factors will depend on the thickness of the sample, the atomic number of the backscattering material, and the maximum energy of the  $\beta$ -particles. Relationships between the mass-absorption coefficient and the maximum energy of the  $\beta$ -particles for the primary  $\beta$ -particles, and between the mass-absorption coefficient, the maximum energy of the  $\beta$ -particles, and the atomic number of the backscattering material for the back-scattered  $\beta$ -particles, are obtained. The backscattering function is found to depend on the atomic number of the backscattering material alone.

### I. INTRODUCTION

When the absolute disintegration rate of electrons from a  $\beta$ -particle-emitting source is to be determined, several correction factors have to be applied to the experimentally measured counting rate. Following Zumwalt (1947, 1950a) and Burtt (1950), these can be classified as follows:

$$(1) \quad c/m = (dis/m) f_w \cdot f_c \cdot f_A \cdot f_B \cdot f_H \cdot f_S \cdot f_E \cdot f_G$$

where

$c/m$  = observed counts per minute, after background is subtracted;

$dis/m$  = absolute number of disintegrations per minute;

$f_w$  = factor for the effect of absorption of  $\beta$ -particles by the counter window and by the air in the space between the counter tube and the source;

$f_c$  = factor for the effect of finite resolving time of the counting tube and the circuit;

$f_A$  = factor for the effect of air in scattering of the  $\beta$ -particles;

$f_B$  = factor for the effect of increase in counting rate due to backscattering by the material supporting the source;

$f_H$  = factor for the effect of the source-support structure and walls of the housing in scattering  $\beta$ -particles into the counter tube;

$f_S$  = factor for the effect of the mass of the source in causing both scattering and absorption of  $\beta$ -particles;

$f_E$  = factor for the effect of variation of the ionization efficiency inside the tube at different positions;

$f_G$  = factor for the effect of the geometry of the counter.

In many cases Geiger-Müller tubes have been used in determinations of absolute disintegration rates. Some of the correction factors have been hard to calculate, especially  $f_A$ ,  $f_H$ ,  $f_E$ , and to some degree  $f_G$ , thus making the

<sup>1</sup>Manuscript received December 30, 1958.

Contribution from the Physics Department, University of Saskatchewan, Saskatoon, Saskatchewan, Canada.

absolute values of the disintegration rates uncertain to several per cent. It was therefore thought desirable to use a proportional flow-counter in order to eliminate the most troublesome of these factors. Also, when the counting rate is low, a high geometry flow-counter is to be preferred to a narrow-angle Geiger-Müller tube. In a proportional flow-counter, the following correction factors do not need to be taken into consideration:  $f_W$ ,  $f_A$ , and  $f_R$ . The factor  $f_G$  was taken to be 0.5, assuming pure  $2\pi$ -geometry when using samples in the form of thin disks. The manufacturers guarantee in this case the geometry of the counter to be  $2\pi$  within 0.5%. The factor  $f_C$  was found to be unity within 0.1% when the counting rate was kept below 200,000 counts/min (see Part IIA, iii). The factor  $f_E$  was also found to be unity for the disks used as sources in the present work (see Part IIA, i and ii). We thus arrive at the formula for correction of the counting rate in a proportional flow-counter:

$$(2) \quad c/m = (dis/m) \cdot f_S \cdot f_B \cdot 0.5.$$

The two correction factors  $f_S$  and  $f_B$  cannot, as with Geiger-Müller tubes, be investigated separately, since both self-absorption and backscattering occur when a sample is counted in the flow-counter. A special method must therefore be used to investigate and determine the two factors. The development of such a method is described in this paper. Investigations of the product of these two factors have been made only by using a quite different technique. Nervik and Stevenson (1951, 1952) precipitated an aliquot of activity with various amounts of inactive carrier on a defined area to form pill-shaped samples. No valid formula for  $f_S$  and  $f_B$  were, however, obtained.

## II. EXPERIMENTAL TECHNIQUE

### A. COUNTER EFFICIENCY

#### (i) *Horizontal Direction*

In order to find out whether the efficiency of the counter varied in the horizontal direction from the center of the counter chamber, the following experiment was carried out. Copper disks of the same thickness, but with diameters ranging from 1 to 5 cm were irradiated in the center of the X-ray beam, from the University of Saskatchewan betatron, all at the same distance from the target and with the same maximum betatron energy. The irradiation times were the same for all disks, 1 minute, and the relative doses were measured with a monitor in connection with an  $R-C$  circuit whose time constant equaled the mean life of the  $Cu^{62}$   $\beta$ -activity. The disks were mounted on a backscatterer of copper, 5 cm in diameter and 1.6 mm thick, and counted in the flow-counter. The numbers of counts between 15 and 20 minutes after irradiation stopped were recorded, and after subtraction of background, divided by the relative dose, by the disk area, and by a correction factor which takes into account "peaking" of the X-ray beam.

The resulting values are plotted in Fig. 1 as a function of the radii of the disks. It is seen that the horizontal efficiency of the counter is constant for a radius up to 1.5 cm, then decreases for higher radii. The higher values at  $r = 0.5$  cm are probably due to slight irregularities in the circular shape of

this small disk. Since we have been using disks of 1.25 cm in radius throughout this work, no correction for the horizontal efficiency of the counter was found necessary.

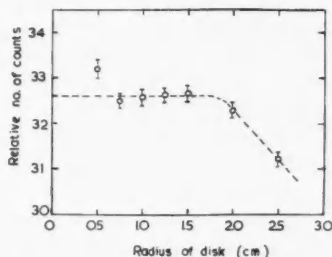


FIG. 1. Relative counting rate as a function of sample radius.

#### (ii) Vertical Direction

The efficiency of the counter chamber in the vertical direction was also investigated by using backscatterers of the same material but of different thicknesses, ranging from the thickness corresponding to saturated back-scattering with the material used and  $\text{Cu}^{62}$   $\beta$ -particles (see Part IIIB, ii(a)), up to the maximum thickness that could be moved into position in the counter.

No change in efficiency in vertical position was observed up to a thickness of 4 mm of backscattering material.

#### (iii) Dead Time of the System

The dead time of a proportional flow-counter is very low compared with that of Geiger-Müller counters. Copper samples with very high initial activity were counted; logarithmic plots of counts per minute versus time showed only very small deviations from straight lines at high counting rates. The counting loss was found to be less than 0.1% for a counting rate of 200,000 counts/minute. Since the counting rate in this work at no time exceeded 50,000 counts/minute, no correction for counting loss was found necessary.

### B. IRRADIATION AND COUNTING TECHNIQUE

Circular disks of copper, zinc, nickel, molybdenum, and polystyrene were irradiated at the center of the X-ray beam from a 25-Mev betatron at a fixed position 54.7 cm from the target. The disks had a diameter of 2.5 cm and thicknesses varying from about 10 mg/cm<sup>2</sup> to several hundred milligrams per square centimeter. All disks of the same material were irradiated at the same maximum betatron energy, which was selected to give initial counting rates below 50,000 counts/minute, in order to avoid any counting loss.

The disks were either (a) given a constant total dose, the effect of variations in irradiation time,  $t_R$ , being removed by multiplication by the factor  $t_R/(1 - e^{-\lambda t_R})$  or (b) irradiated for a fixed time, the dose being measured by a monitor in connection with an  $R-C$  circuit of proper time constant. In the latter case the counting rates were divided by the relative doses.

The disks were counted in a proportional flow-counter\* containing P-10 gas. The counter was found to have a 200-volt  $\beta$ -plateau with no detectable slope. As backscatterers were used circular disks of aluminum, copper, cadmium, and lead, 4 cm in diameter and 1.6 mm in thickness.

The irradiated disk was placed upon one backscatterer and the number of counts in 1 minute recorded. This was repeated for each backscatterer in turn, the decay being followed for several half lives to make sure that no spurious activities were present. The logarithm of the number of counts per minute (less background) was plotted as a function of time. From this plot, the counting rates at a fixed time, 10 minutes after irradiation stopped say, were obtained. These were corrected either for finite irradiation time or for relative dose as mentioned above. The corrected counting rates thus obtained were then divided by numbers proportional to the number of atoms present in the disks (either the weight in milligrams or the number of moles of the  $\beta$ -emitting isotope).

Thus for each  $\beta$ -emitter was obtained a series of corrected relative counting rates corresponding to different sample thicknesses with each of the four above-mentioned backscattering materials.

### III. ANALYSIS OF RESULTS

#### A. TREATMENT OF RESULTS

For one particular  $\beta$ -emitter, the corrected counting rate per milligram or mole will depend on the thickness  $x$  of the disk, given in  $\text{mg}/\text{cm}^2$ , and on the atomic number  $Z$  of the backscatterer. These counting rates will be referred to as  $N(x, Z)$ . The relation between  $N(x, Z)$  and the value with an infinitely thin sample and zero backscattering  $N(0, 0)$  (i.e. no self-absorption and no backscattering) is assumed to be of the form:

$$(3) \quad N(x, Z) = F_1(x) [1 + S(Z) \cdot F_2(x, Z)] N(0, 0)$$

where  $F_1(x)$  is the factor due to self-absorption ( $\equiv f_s$ ). This is assumed to approach unity when  $x$  goes to zero.

$S(Z)$  gives the amount of the primary  $\beta$ -radiation that is scattered back.  $S(Z)$  is assumed to go to zero when  $Z$  goes to zero.

$F_2(x, Z)$  is the factor due to absorption of the backscattered radiation in the disk.  $F_2(x, Z)$  is assumed to go to unity when  $x$  goes to zero.

$[1 + S(Z) \cdot F_2(x, Z)]$  is the factor previously called  $f_B$ .

Formula (3) and the three above assumptions were used to obtain values for  $N(0, 0)$ ,  $F_1(x)$ ,  $S(Z)$ , and  $F_2(x, Z)$ . Copper will here be used as an example of the procedure that was followed.

(a)  $N(x, Z)$  was plotted as a function of  $Z$  for each different value of  $x$ . The curves were extrapolated to  $Z = 0$  to give  $N(x, 0) = F_1(x) N(0, 0)$ . Figure 2 gives four examples chosen from the 17  $x$  values used.

(b)  $N(x, Z)$  was plotted as a function of  $x$  for each value of  $Z$ . The curves were extended back to  $x = 0$  to give  $N(0, Z) = [1 + S(Z)] N(0, 0)$  (Fig. 3).

\*Nuclear measurements: alpha-beta-gamma proportional counter Model PC-3 Serial No. 40.

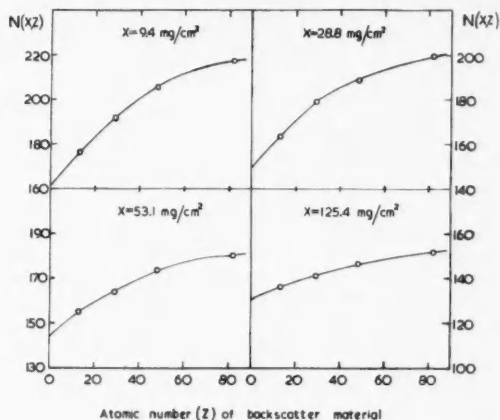


FIG. 2. Relative counting rate,  $N(x, Z)$ , versus  $Z$  of backscattering material for four different sample thicknesses,  $x$  (for  $\text{Cu}^{62}$  positrons).

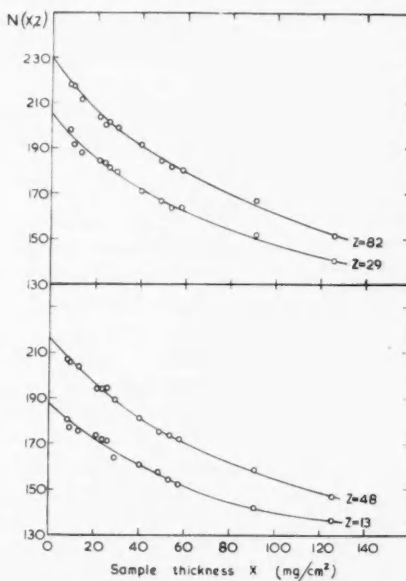


FIG. 3. Relative counting rate,  $N(x, Z)$ , versus sample thickness,  $x$ , for four backscattering materials (for  $\text{Cu}^{62}$  positrons).

(c)  $N(x, 0)$  was plotted as a function of  $x$ , and was extended back to  $x = 0$  to give  $N(0, 0)$  (Fig. 4). As is seen from this figure the minimum value of  $N(0, 0)$  is well fixed.

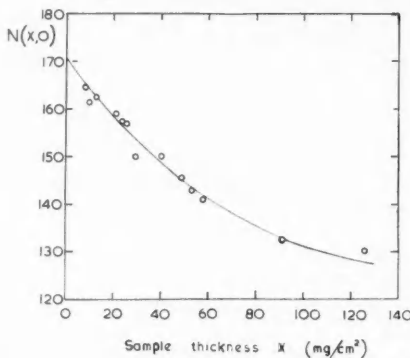


FIG. 4. Relative counting rate with zero backscattering,  $N(x, 0)$ , versus sample thickness,  $x$  (for  $\text{Cu}^{62}$  positrons).

(d)  $N(0, Z)$  was plotted as a function of  $Z$ , and was extended back to  $Z = 0$  to give  $N(0, 0)$  (Fig. 5). As is seen from this figure the maximum value of  $N(0, 0)$  is well fixed.

(e) The values of  $N(0, 0)$  from Figs. 4 and 5 were compared, and the best average value of  $N(0, 0)$  assumed. In the case of  $\text{Cu}^{62}$  the value  $N(0, 0) = 171$  was selected.

(f)  $S(Z)$  was calculated by using the formula  $S(Z) = [N(0, Z)/N(0, 0)] - 1$ , and is shown in Fig. 6 as a function of  $Z$ .

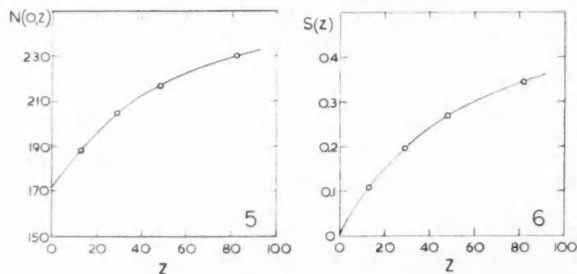


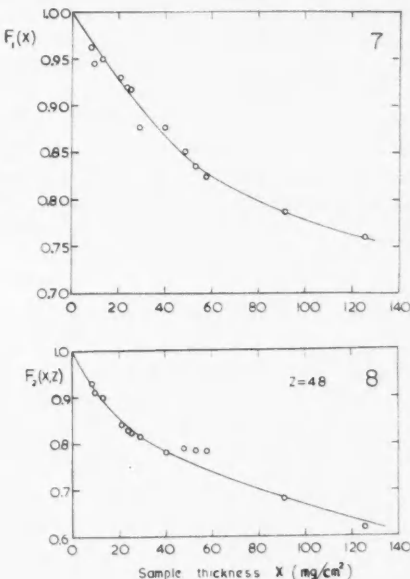
FIG. 5. Relative counting rate for 'zero' sample thickness,  $N(0, Z)$ , versus  $Z$  of backscattering material (for  $\text{Cu}^{62}$  positrons).

FIG. 6. Backscattering function  $S(Z)$  versus  $Z$  of backscattering material (for  $\text{Cu}^{62}$  positrons).

(g)  $F_1(x)$  was calculated from  $F_1(x) = [N(x, 0)/N(0, 0)]$  and is given in Fig. 7.

(h)  $F_2(x, Z)$  was calculated as a function of  $x$  for different values of  $Z$  by using the formula  $F_2(x, Z) = \{[N(x, Z)/N(x, 0)] - 1\}/S(Z)$ . Figure 8 gives an example ( $Z = 48$ ).

The form of the functions  $F_1(x)$ ,  $S(Z)$ , and  $F_2(x, Z)$  and their dependence on the energy of the  $\beta$ -particles will be discussed in the following sections.

FIG. 7. Self-absorption function  $F_1(x)$  versus sample thickness  $x$  (for  $\text{Cu}^{64}$  positrons).FIG. 8. Absorption function for backscattered  $\beta$ -particles,  $F_2(x, Z)$ , versus sample thickness,  $x$ , for  $Z = 48$  of backscattering material (for  $\text{Cu}^{64}$  positrons).

## B. DISCUSSION OF THE FUNCTIONS $F_1(x)$ , $S(Z)$ , AND $F_2(x, Z)$

### (i) Self-Absorption and Self-Scattering

An exact theoretical treatment of the self-absorption of the  $\beta$ -particles in the  $\beta$ -emitting sample itself is very hard to handle, and so far no attempt has been made in this direction. This is due to the complicated and often not fully known energy spectrum of the  $\beta$ -particles from allowed and forbidden transitions, to the variation of the mass-absorption coefficient for the  $\beta$ -particles with their energy, and also to the elastic scattering of the  $\beta$ -particles by the atoms in the sample.

#### (a) Self-Scattering

A brief discussion of the last effect will be mentioned first. It must be assumed that the original angular distribution of the  $\beta$ -particles is isotropic. However, after leaving the sample, the angular distribution is anisotropic, and, moreover, it is dependent on the thickness of the sample. This was first pointed out by Collie *et al.* (1950) and has later been confirmed by Elliot *et al.* (1951), Brownell (1952), Graf *et al.* (1951), and Baker and Katz (1953). It has been found that for samples of thickness greater than  $0.2R$ , where  $R$  is the range of the  $\beta$ -particles with maximum energy, the angular distribution follows a cosine law to a very good approximation. For thinner samples there will be more  $\beta$ -particles scattered into greater angles to the normal to the sample, and this effect will increase with decreasing sample thickness. Thus,

if a narrow-angle geometry is used, the counter records a relatively smaller fraction of  $\beta$ -particles from thin samples ( $<0.2R$ ) than from thick samples ( $>0.2R$ ). In a combined self-absorption and self-scattering curve this gives rise to a maximum value of the relative counting rate at a small, non-zero sample thickness (e.g. for  $\text{Cu}^{62}$ , the maximum was found at  $x \simeq 150 \text{ mg/cm}^2$  (Baker and Katz 1953)). However, since in the present work we are using  $2\pi$ -geometry, and all  $\beta$ -particles between 0 and 90 degrees to the normal are counted, the self-scattering effect should be of small or no importance. This is also confirmed by the curves of  $N(x, 0)$  versus  $x$ , which show no maximum values at small but non-zero  $x$ .

(b) *Self-Absorption*

Since no exact theoretical formula for the self-absorption curve can be given, approximate formulas have to be assumed and their fit to the experimental values investigated. The first assumption made is that  $F_1(x)$  is of the form  $F_1(x) = F_1(kx)$ , where  $k$  is the mass-absorption coefficient, given in  $\text{cm}^2/\text{mg}$ ;  $k$  is a constant for one particular  $\beta$ -emitter and depends only on  $E_{\max}$ , the maximum energy of the  $\beta$ -spectrum. Values for  $k$  must be found empirically by fitting the curves of the chosen formula to the experimental points.

The most simple formula will be  $F_1(kx) = e^{-kx}$ . This formula was first used by Broda *et al.* (1948), who found  $k \propto (1/R)$ . The formula was only approximate for medium sample thickness.

Using a narrow-angle geometry, Schweitzer and Stein (1950) assumed all  $\beta$ -particles to go in the normal direction and integrated over the thickness of the sample to get the formula:

$$(4) \quad F_1(kx) = \frac{1 - e^{-kx}}{kx}.$$

The same formula has later been used for wide-angle geometry also, giving a good fit to the experimental points (Suttle 1952; Baker and Katz 1953). However, an attempt to relate the experimental values of the present work to a curve for  $F_1(kx)$  of this formula was unsuccessful. A new formula, integrating both over the thickness of the sample and over the angles from 0 to  $\pi/2$ , assuming isotropic distribution, was therefore carried through, yielding:

$$(5) \quad F_1(k_1x) = \frac{1}{2} \left[ \frac{1 - e^{-k_1x}}{k_1x} + e^{-k_1x} + k_1x \text{Ei}(-k_1x) \right]$$

where  $\text{Ei}(-k_1x)$  is the exponential integral of  $(-k_1x)$ . Values for  $\text{Ei}(-k_1x)$  were taken from Lowan (1940).  $F_1(y)$  versus  $y$  ( $\equiv k_1x$ ) is given in Fig. 9. (For explanation of  $F_2(y)$ , see Part IIIB, iii.) The experimental points are found to follow curves of this shape very well if the correct value of  $k_1$  is chosen.

The value of  $k_1$  for each  $\beta$ -emitter that gave the best fit was calculated. These are given in Table I together with the corresponding  $E_{\max}$  values. Also given are the standard deviations from the means.

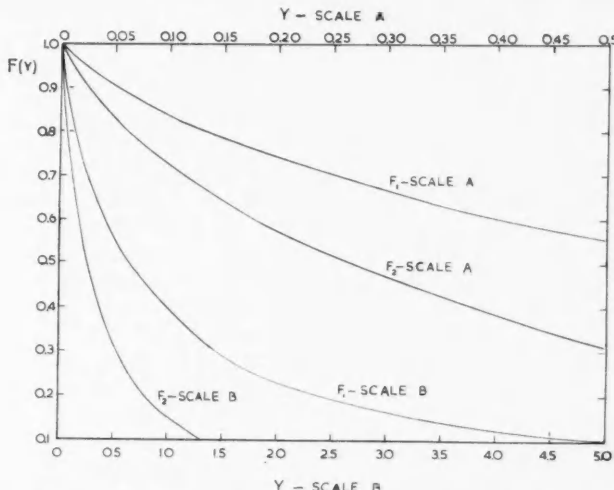


FIG. 9. Functions  $F_1(y)$  and  $F_2(y)$  versus  $y$ , where  $y = k_1 x$  and  $k_2 x$  respectively. These functions are defined in equations (5) and (8) respectively.

TABLE I  
Mass-absorption coefficient  $k_1$  (in  $\text{cm}^2/\text{mg}$ ) of primary  $\beta$ -particles versus maximum energy of the  $\beta$ -particles,  $E_{\max}$  (in Mev)

Isotope	$E_{\max}$ , Mev	$k_1$ , $\text{cm}^2/\text{mg}$
$\text{Ni}^{67}$	0.84	$0.0175 \pm 0.0025$
$\text{C}^{11}$	0.99	$0.0110 \quad 0.0010$
$\text{Zn}^{65}$	2.36	$0.00265 \quad 0.00030$
$\text{Cu}^{62}$	2.92	$0.00160 \quad 0.00014$
$\text{Mo}^{91}$	3.44	$0.00122 \quad 0.00009$

A plot of  $\log k_1$  versus  $\log E_{\max}$  is given in Fig. 10. As seen from this figure, the points can be fairly well represented by a straight line. The best-fitting line yields:

$$(6) \quad k_1 = 0.0119 E_{\max}^{-1.83}$$

where  $k_1$  is in  $\text{cm}^2/\text{mg}$  and  $E_{\max}$  in Mev. This relationship between the mass-absorption coefficient  $k_1$  and the  $\beta$ -ray end-point energy  $E_{\max}$  may be compared with relations found by:

$$\text{Gleason et al. (1951)} \quad k_1 = 0.017 E_{\max}^{-1.43}$$

$$\text{Evans (1947)} \quad k_1 = 0.022 E_{\max}^{-1.33}$$

$$\text{Baker and Katz (1953)} \quad k_1 = 0.0155 E_{\max}^{-1.41}$$

It should be noted that these formulae apply to different cases. The first two were obtained by the use of external absorbers in which case the relation  $F(kx) = e^{-kx}$  applies; the third was obtained for self-absorption by the use

of equation (4) rather than the equation (5) which is used in the present work.

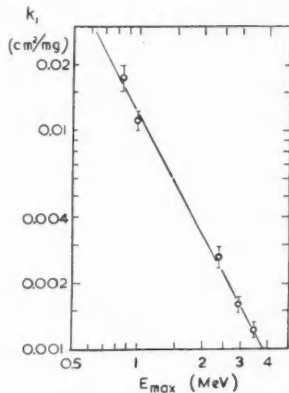


FIG. 10. Mass-absorption coefficient  $k_1$  (in  $\text{cm}^2/\text{mg}$ ) of primary  $\beta$ -particles versus maximum energy of the  $\beta$ -particles,  $E_{\max}$  (in Mev).

### (ii) Backscattering

#### (a) Saturated Backscattering

Pure backscattering effect can be obtained by using very thin samples mounted on the backscatter material. Self-absorption and absorption of backscattered radiation will then be negligible. Pure backscattering has been investigated by several authors. Yaffe and Justus (1949) and Yaffe (1950) found that for a given sample and backscatter material, i.e. with fixed values of  $E_{\max}$ ,  $x$ , and  $Z$ , the backscattering effect will vary with the thickness  $t$  of the backscatterer, the effect increasing with increasing  $t$ . However, above a thickness  $t_{\max}$  (in  $\text{mg}/\text{cm}^2$ ) the backscattering effect will become constant; this is called saturated backscattering. The value of  $t_{\max}$  was found to be independent of  $Z$ , and a function of  $E_{\max}$  only.

Yaffe and Justus found empirically that  $t_{\max}^2 \simeq 36R$ , where  $t_{\max}$  is given in  $\text{mg}/\text{cm}^2$ , and  $R$ , the range of the maximum energy  $\beta$ -particles, is in  $\text{mg}/\text{cm}^2$ . Using Libby's (1947) relation between  $R$  and  $E_{\max}$ , this may also be written  $t_{\max} \simeq 116 E_{\max}^{2/3}$ , where  $E_{\max}$  is given in Mev.

The highest value of  $E_{\max}$  used in this work is 3.44 Mev, for  $\text{Mo}^{91}$   $\beta$ -particles. Using the formula of Yaffe and Justus and the range-energy relation as given by Katz and Penfold (1952), we arrive at  $t_{\max} \simeq 270 \text{ mg}/\text{cm}^2$ . Backscatter disks of thicknesses  $\geq 270 \text{ mg}/\text{cm}^2$  will thus give us saturated backscattering for  $\text{Mo}^{91}$   $\beta$ -particles, and this will of course also ensure saturated backscattering for all  $\beta$ -particles with lower  $E_{\max}$ .

Since the lightest backscatter material used in the present work is aluminum with a density of  $2.70 \text{ g}/\text{cm}^3$ , a thickness of  $1.0 \text{ mm}$  will be sufficient for this material, and smaller thicknesses for the heavier backscatter materials. Actually all backscatter disks were of the same thickness,  $1.6 \text{ mm}$ , so we should

be well within the region of saturated backscattering with the  $\beta$ -particles and the backscatter material used in these experiments. Our function  $S(Z)$  thus refers to saturated backscattering.

(b) *Angular Distribution*

Yaffe and Justus (1949) also measured the angular distribution of the backscattered  $\beta$ -particles and found it to be anisotropic with a maximum in the direction vertical to the backscatterer. This anisotropy increases with increasing  $t$  until  $t_{\max}$  is obtained. From then on it is fairly constant.

Zumwalt (1950b) also finds  $S(Z)$  to vary with distance from source to counter, i.e. with the geometry, indicating anisotropy of the backscattered radiation. He finds that the backscattered radiation tends to be preferentially concentrated in the direction perpendicular to the backscattering surface for atomic numbers  $Z > 37$ . On the other hand, for  $Z < 37$ , the backscattered radiation was found to be preferentially concentrated in directions close to the plane of the backing material.

Following Zumwalt, it should be expected, when going from narrow-angle geometry to  $2\pi$ -geometry, that  $S(Z)$  should increase for small  $Z$  ( $< 37$ ) and decrease for higher  $Z$  ( $> 37$ ).

Angular distribution was also measured by Brownell (1952), who found a nearly isotropic distribution for small  $Z$  ( $< 12$ ), approaching a cosine distribution for higher  $Z$ .

(c) *The Function  $S(Z)$*

The calculated values of  $S(Z)$  for the four backscatter materials are given in Table II for the  $\beta$ -emitters used, in order of increasing value of  $E_{\max}$ . Also given are the mean values for each  $Z$  and their standard deviations.

TABLE II

Values of the backscattering function  $S(Z)$  versus  $Z$  of the backscattering material for five different  $\beta$ -emitters

$Z$	$\text{Ni}^{67}$	$\text{C}^{14}$	$\text{Zn}^{65}$	$\text{Cu}^{62}$	$\text{Mo}^{91}$	Mean
13	0.103	0.111	0.103	0.111	0.121	$0.110 \pm 0.007$
29	0.207	0.197	0.191	0.199	0.206	$0.200 \pm 0.007$
48	0.276	0.250	0.265	0.269	0.261	$0.264 \pm 0.010$
82	0.345	0.347	0.360	0.345	0.333	$0.346 \pm 0.010$

It is seen that  $S(Z)$  is independent of  $E_{\max}$  in the region 0.84 to 3.44 Mev. This is in agreement with Yaffe and Justus (1949), who found  $S(Z)$  independent of  $E_{\max}$  for  $E_{\max} > 1$  Mev; also with Burtt (1949 and 1950), who found  $S(Z)$  independent of  $E_{\max}$  for  $E_{\max} > 0.6$  Mev; and with Engelkemeir *et al.* (1951), who found it independent in the region 1.0 to 2.5 Mev. It is in contradiction with the work of Christian *et al.* (1952), who found  $S(Z)$  dependent of  $E_{\max}$ , with decreasing values of  $S(Z)$  for increasing  $E_{\max}$ .

The mean values of  $S(Z)$  are given in Fig. 11 as a function of  $Z$ , curve I.

$S(Z)$  has been measured in narrow-angle geometry ( $\approx 7\%$ ) by Yaffe and Justus (1949), Yaffe (1950), Burtt (1949, 1950), Engelkemeir *et al.* (1951),

Zumwalt (1950b), and Tobias (1948). Their values agree well within experimental error, and the mean of their results is shown in Fig. 11, curve II.

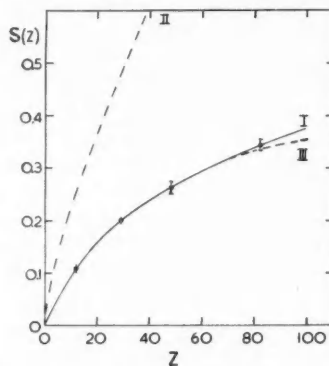


FIG. 11. Backscattering function  $S(Z)$  versus  $Z$  of backscattering material, averaged for five different  $\beta$ -emitters.

These values are all much higher than the values from the present work, even at small  $Z$ . This would be predicted if the angular distribution of Yaffe and Justus (1949) is correct, but is in contradiction with the work of Zumwalt (1950b) and Borkowski (1950).

Glendenin and Solomon (1950) measured  $S(Z)$  for 9 and 25% geometry, obtaining no variation of  $S(Z)$  with geometry. Their values lie still higher than curve II.

The simplest mathematical formula that can be used to describe  $S(Z)$  is of the form  $S(Z) = a(1 - e^{-bZ})$ . The best-fit curve of this form for the present values of  $S(Z)$  is:

$$(7) \quad S(Z) = 0.37 (1 - e^{-0.0275Z}).$$

This curve is also given in Fig. 11, curve III. Suttle (1952) showed that the  $S(Z)$  values obtained by Glendenin and Solomon (1950) could be represented by a similar relation, with  $a = 1.30$  and  $b = 0.0231$ .

### (iii) Absorption of Backscattered Radiation

The calculated values for the function  $F_2(x, Z)$  are subject to great uncertainty. Since  $[N(x, Z)/N(x, 0)]$  is near 1, a small error in this ratio will introduce a rather high error in  $F_2(x, Z)$ . For intermediate sample thicknesses (50–100 mg/cm<sup>2</sup>) an error of 1% in  $F_1(x)$  introduces an error of 10 to 20% in  $F_2(x, Z)$  and this effect increases with increasing thickness.

The form of the functions  $F_2(x, Z)$  must be assumed to be very complicated, due to the double anisotropy in the angular distribution taking place in (1) self-scattering and in (2) backscattering. One must therefore, as in self-absorption, assume a simple form for  $F_2(x, Z)$  and investigate how well the experimental points will fit these curves. The first assumption is then that  $F_2(x, Z) = F_2[k_2(Z)x]$ .

The simplest form is  $F_2(x, Z) = e^{-k_2(Z)x}$ , assuming all backscattered

$\beta$ -particles to go in the vertical direction. However, the experimental points do not fit curves of this form very well, the deviations from the curves being greater than the expected error.

Assuming isotropic distribution of the backscattered radiation, an integration over the angles from 0 to  $\pi/2$  was carried through, similar to the one under self-absorption. This formula yields:

$$(8) \quad F_2[k_2(Z) \cdot x] = e^{-k_2 x} + k_2 x \cdot \text{Ei}(-k_2 x).$$

The experimental points followed curves of this form to within experimental error.  $F_2(y)$  vs.  $y$  is given in Fig. 9 ( $y \equiv k_2(Z) \cdot x$ ).

The values of  $k_2$  calculated to fit these curves are given in  $\text{cm}^2/\text{mg}$  in Table III;  $k_2$  is as expected a function of both  $E_{\max}$  and  $Z$ .

TABLE III  
Absorption coefficient  $k_2$  (in  $\text{cm}^2/\text{mg}$ ) for backscattered  $\beta$ -particles  
versus  $Z$  of the backscattering material for five different  $\beta$ -emitters

$Z$	$\text{Ni}^{67}$	$\text{C}^{11}$	$\text{Zn}^{65}$	$\text{Cu}^{63}$	$\text{Mo}^{91}$
13	0.0074	0.0077	0.0039	0.0029	0.0028
29	0.0063	0.0055	0.0031	0.0024	0.0022
48	0.0052	0.0045	0.0026	0.0017	0.0016
82	0.0058	0.0050	0.0026	0.0019	0.0016

Of more interest than  $k_2$  itself is the ratio  $k_2/k_1$ . This is plotted in Fig. 12

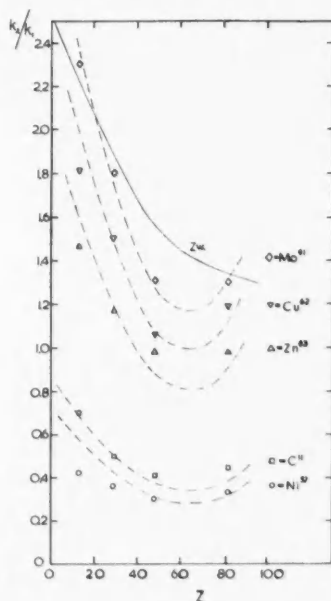


FIG. 12. Ratio of absorption coefficients for backscattered and primary  $\beta$ -particles,  $k_2/k_1$ , versus  $Z$  of the backscattering material, for five  $\beta$ -emitters.

as a function of  $Z$  for the different  $\beta$ -emitters. Several conclusions can be drawn from these curves.

1. The shapes of the curves are generally the same with respect to  $Z$ ;  $k_2/k_1$  can therefore be assumed to be of the form  $k_2/k_1 = f(E_m) \cdot g(Z)$ .

2.  $g(Z)$  decreases when  $Z$  goes from 0 to  $\sim 60$ . Results obtained for the one backscatterer, lead, indicate that it then increases for higher  $Z$ .

3.  $f(E_m)$  increases with increasing values of  $E_{\max}$ . It is also seen that for  $E_{\max}$  greater than about 2 Mev,  $k_2/k_1$  is generally greater than 1, while for lower values of  $E_{\max}$ ,  $k_2/k_1$  is generally less than 1. This means that for  $E_{\max} > 2$  Mev, the backscattered radiation is softer than the initial radiation, whereas for  $E_{\max} < 2$  Mev the backscattered radiation is harder than the initial radiation. Two competing effects might be assumed to occur:

(a) Higher self-absorption for the soft (low energy) part of the  $\beta$ -spectrum than for the hard. This will make the backscattered radiation harder than the initial. This effect is seen to be predominant for low original  $E_{\max}$  ( $< 2$  Mev).

(b) Inelastic backscattering. This will decrease the energy of the back-scattered  $\beta$ -particles and thus soften the backscattered radiation. This effect is seen to be predominant for higher values of original  $E_{\max}$  ( $> 2$  Mev).

When using pure backscattering with negligible self-absorption, only the latter effect will be observed. This was done by Glendenin and Solomon (1950), who found the half-thickness of the backscattered radiation to be approximately half that of the original radiation. Zumwalt (1950b) found the ratio of the half-thicknesses of the two radiations to increase with  $Z$ , ranging from about 0.4 for  $Z = 0$  to about 0.8 for  $Z = 90$ . To a first approximation he also found the ratio to be independent of  $E_{\max}$ ; the spread is, however, too great to say this with any degree of certainty. Since  $k = \ln 2/R_{\frac{1}{2}} \cdot \rho$  where  $R_{\frac{1}{2}}$  is the half-thickness and  $\rho$  the density,  $k_2/k_1$  corresponds to  $[R_{\frac{1}{2}}^{(1)}]/[R_{\frac{1}{2}}^{(2)}]$ . Thus Zumwalt's values correspond to  $k_2/k_1 \simeq 2.5$  for  $Z = 0$  and  $\simeq 1.3$  for  $Z = 90$ . This curve is also given in Fig. 12, curve  $Zw$ . As expected, it lies higher than all the experimental curves from the present work.

In order to find some empirical equations for  $f(E_{\max})$  and  $g(Z)$ ,  $k_2/k_1$  was plotted as a function of  $E_m$  for different values of  $Z$  (Fig. 13). To a very good approximation the experimental points yield straight lines through the origin. The function  $f(E_{\max})$  might therefore be taken to be  $f(E_{\max}) = E_{\max}$ , and the slopes of the lines will give  $g(Z)$ .

This function  $g(Z)$  is plotted in Fig. 14. The drawn line is given by the formula:

$$(9) \quad g(Z) = 1.31 \times 10^{-4}(Z - 64)^2 + 0.340$$

and gives a good approximate fit to the points. Thus, to a first approximation we arrive at the empirical formula,

$$(10) \quad k_2/k_1 = f(E_{\max}) \cdot g(Z) = [1.31 \times 10^{-4}(Z - 64)^2 + 0.340]E_{\max},$$

where  $E_{\max}$  is given in Mev. This is the formula used to draw the curves of Fig. 12. It can be seen to represent the experimental points well, at least for  $E_{\max} \geq 1$  Mev. By substituting for  $k_1$ , we get for  $k_2$ :

$$(11) \quad k_2 = [1.56 \times 10^{-6}(Z - 64)^2 + 4.05 \times 10^{-3}]E_{\max}^{-0.83}.$$

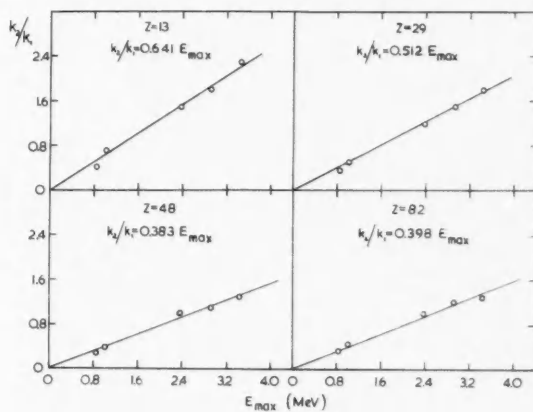


FIG. 13. Ratio of absorption coefficients for backscattered and primary  $\beta$ -particles,  $k_2/k_1$ , versus maximum energy of the  $\beta$ -particles,  $E_{\max}$ , for four backscattering materials.

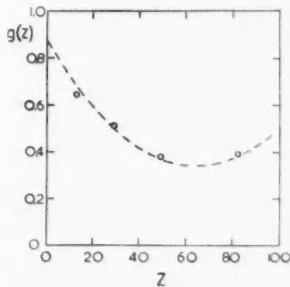


FIG. 14. Figure showing the dependence of the ratio of absorption coefficients for backscattered and primary  $\beta$ -particles on the atomic number  $Z$  of the backscattering material, when dependence on maximum energy is removed (see equation (9)).

#### IV. SUMMARY

The correction factor for the counting rate in a  $2\pi$ -geometry proportional flow-counter is given by

$$(2) \quad c/m = 1/2(dis/m) \cdot f_S \cdot f_B.$$

Assuming that  $f_S \cdot f_B$  is of the form:

$$(3) \quad f_S \cdot f_B = F_1(x) [1 + S(Z) F_2(x, Z)]$$

where

$F_1(x)$  is the factor due to self-absorption and self-scattering,

$S(Z)$  is the factor due to saturated backscattering alone,

$F_2(x, Z)$  is the factor due to absorption of the backscattered radiation,

the following empirical relations were found:

$F_1(x) = F_1(k_1 x)$  where  $k_1$  is the mass-absorption coefficient.

$$(5) \quad F_1(k_1 x) = 1/2 \{ [(1 - e^{-k_1 x})/k_1 x] + e^{-k_1 x} + k_1 x \operatorname{Ei}(-k_1 x) \}$$

$$(6) \quad k_1 = k_1(E_{\max}) = 0.0119 E_{\max}^{-1.83}$$

where  $k_1$  is given in  $\text{cm}^2/\text{mg}$  and  $E_{\max}$  in Mev.

$S(Z)$  is given in Fig. 11 or by the formula

$$(7) \quad S(Z) = 0.37 (1 - e^{-0.0275 Z})$$

$$(8) \quad F_2(x, Z) = F_2(k_2 x) = e^{-k_2 x} + k_2 x \operatorname{Ei}(-k_2 x)$$

where

$$(11) \quad k_2 = k_2(E_{\max}, Z) = [1.56 \times 10^{-6}(Z - 64)^2 + 4.05 \times 10^{-3}] E_{\max}^{-0.83}.$$

#### REFERENCES

BAKER, R. G. and KATZ, L. 1953. Nucleonics, **11** (2), 14.

BORKOWSKI, C. F. 1950. Oak Ridge National Laboratory (unpublished). (Results are given in L. R. Zumwalt (1950b).)

BRODA, E., GRUMMIT, W. E., GUERON, J., KOWARSKI, L., and WILKINSON, G. 1948. Proc. Phys. Soc. **60**, 460.

BROWNELL, G. L. 1952. Nucleonics, **10** (6), 30.

BURTT, B. P. 1949. Nucleonics, **5** (2), 28.

— 1950. In Conference on absolute  $\beta$ -counting. N.R.C. Washington, Report 8, Nuclear Science Series, paper No. 1.

CHRISTIAN, D., DUMMINGS, W. W., and MARTIN, D. S. 1952. Nucleonics, **10** (5), 41.

COLLIE, C. H., SHAW, P. F. D., and GALE, H. F. 1950. Proc. Phys. Soc. A, **63**, 282.

ELLIOT, N., ENGELKEMEIR, D. W., and RUBINSON, W. 1951. In Radiochemical studies: the fission products. National Nuclear Energy Series, IV-9 (McGraw-Hill Book Co., Inc., New York), p. 25.

ENGELKEMEIR, D. W., SEILER, J. A., STEINBERG, E. P., WINSBERG, L., and NOVEY, T. B. 1951. In Radiochemical studies: the fission products. National Nuclear Energy Series (McGraw-Hill Book Co., Inc., New York), p. 56.

EVANS, R. D. 1947. In The science and engineering of nuclear power (Addison-Wesley Press, Cambridge, Mass.), p. 53.

GLEASON, G. I., TAYLOR, J. D., and TABERN, D. L. 1951. Nucleonics, **8** (5), 12.

GLENDENIN, L. E. and SOLOMON, A. K. 1950. Science, **112**, 623.

GRAF, W. L., COMAR, C. L., and WHITNEY, I. B. 1951. Nucleonics, **9** (4), 23.

KATZ, L. and PENFOLD, A. S. 1952. Revs. Modern Phys. **24**, 28.

LIBBY, W. F. 1947. Anal. Chem. **19**, 2.

LOWAN, A. N. 1940. Tables of sine, cosine and exponential integrals. (National Bureau of Standards, New York).

NERVIK, W. E. and STEVENSON, P. C. 1951. University of California Report, U.C.R.L. 1575.

— 1952. Nucleonics, **10** (3), 18.

SCHWEITZER, G. K. and STEIN, B. R. 1950. Nucleonics, **7** (3), 65.

SUTTLE, A. D. 1952. Ph.D. Thesis, University of Chicago, Illinois, U.S.A.

TOBIAS, C. A. 1948. In Handbook of radioactivity and tracer methodology, edited by W. Siri (Air Force Technical Report No. 5669), p. 473.

YAFFE, L. and JUSTUS, K. M. 1949. J. Chem. Soc. Suppl. **72**, 341.

YAFFE, L. 1950. In Conference on absolute  $\beta$ -counting, paper No. 5.

ZUMWALT, L. R. 1947. U.S. Atomic Energy Commission Declass. Document MDDC-1346.

— 1950a. U.S. Atomic Energy Commission Declass. Document AECU-567.

— 1950b. In Conference on absolute  $\beta$ -counting, paper No. 4.

## SELF AND EXTERNAL MESON FIELDS<sup>1</sup>

R. T. SHARP<sup>2</sup>

### ABSTRACT

Instead of a single (isotopic vector) field to describe pions, it is sometimes advantageous to introduce several such fields with identical properties except for their coupling to the sources of the field (the baryons). In this way one can formally distinguish between self pions (roughly, those which can be emitted and absorbed by the same baryon) and external pions (roughly, those which are only exchanged between baryons or emitted into or absorbed from free states).  $K$ -mesons can be treated similarly. The device, which is of general applicability, simplifies many derivations and calculations in quantum field theory. As an illustration of the method it is used to derive the Low equations for scattering of pions and  $K$ -mesons by nucleons and for associated production. A suggestion is made for treating the nucleon-nucleon interaction.

### I. INTRODUCTION

It is known that the static two-nucleon potential problem is simplified by using two pion fields instead of one (Sharp 1958). The fields are coupled to the nucleons in such a way that each nucleon emits and absorbs the pions of its own field, but only absorbs the pions of the field of the other. Then when the exchanged mesons are treated as a perturbation, the two nucleons are uncoupled in zero order while the interaction of each with its own field is taken completely into account. An alternative formulation making use of four pion fields is also possible, and yields equivalent results. Each nucleon has its own "self" field, the quanta of which it emits and absorbs; in addition one introduces two "external" fields such that the quanta of each are emitted specifically by one nucleon and absorbed by the other. The purpose of this paper is to extend these ideas to scattering of mesons by baryons and to the relativistic nucleon-nucleon interaction.

### II. PION-NUCLEON SCATTERING

A Hamiltonian which describes pion-nucleon scattering is

$$(1) \quad H_N + H_1 + \mathfrak{H}_1,$$

where  $H_N$  and  $H_1$  describe the noninteracting nucleon and pion fields and  $\mathfrak{H}_1$  is the interaction.  $\mathfrak{H}_1$  can be decomposed into an emission part and an absorption part for pions:

$$(1a) \quad \mathfrak{H}_1 = \sum_p a_p^* V_p^* + \sum_p a_p V_p,$$

where  $V_p^*$ ,  $V_p$  operate on the state of the nucleon field. Figure 1(a) is the Feynman diagram for pion-nucleon scattering.

We now reformulate the physical problem by postulating three pion fields:

<sup>1</sup>Manuscript received December 9, 1958.

Contribution from the Imperial College, London, England. This work was done under a Nuffield Fellowship.

<sup>2</sup>Present address: Department of Mathematics, McGill University, Montreal, Que.

a self field 1 as before (the quanta of which are emitted and absorbed by the nucleon) and two external fields (2, the quanta of which are absorbed only, and 3, the quanta of which are emitted only). The new Hamiltonian is

$$(2) \quad H_N + H_1 + H_2 + H_3 + \mathfrak{H}_1 + \mathfrak{H}_2^{(-)} + \mathfrak{H}_3^{(+)}$$

where  $H_N$ ,  $H_1$ ,  $H_2$ ,  $H_3$  describe the noninteracting nucleon and pion fields ( $H_1$ ,  $H_2$ ,  $H_3$  are the same as  $H_1$  in (1) except for the different labels), and  $\mathfrak{H}_1$ ,  $\mathfrak{H}_2^{(-)}$ ,  $\mathfrak{H}_3^{(+)}$  are respectively

$$(2a) \quad \mathfrak{H}_1 = \sum_p a_p^{(1)*} V_p^* + \sum_p a_p^{(1)} V_p,$$

$$(2b) \quad \mathfrak{H}_2^{(-)} = \sum_p a_p^{(2)} V_p,$$

$$(2c) \quad \mathfrak{H}_3^{(+)} = \sum_p a_p^{(3)*} V_p^*$$

Four types of scattering process are possible, for the nucleon can absorb an incident self pion or external pion and emit an outgoing self pion or external pion. The Feynman diagrams are shown in Fig. 1.

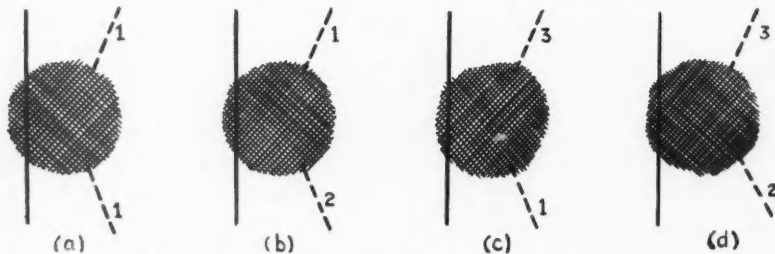


FIG. 1. Four equivalent descriptions of pion-nucleon scattering: (a) absorption and emission of a self pion; (b) absorption of an external pion and emission of a self pion; (c) absorption of a self pion and emission of an external pion; (d) absorption and emission of external pions.

It is important to notice that the  $S$ -matrix element for each of these scattering processes is the same; the incident and outgoing lines are identical in the four diagrams except for the pion labels; only self pions contribute internal lines, so these are also the same in the four cases. Diagram 1(a) is unaffected by external pions and is in fact identical with the correct diagram. Therefore the matrix element for each of the four scattering processes permitted by the Hamiltonian (2) is equal to that for the pion-nucleon scattering described by the correct Hamiltonian (1). In this proof of the "equivalence" of Hamiltonians (1) and (2) all interactions have been treated by perturbation theory to all orders.

Consider the process of Fig. 1(b): absorption of an external pion and emission of a self pion. Treat the interaction of the external pions as a perturbation, including the interaction of the self pions in the zero-order Hamiltonian. First-order perturbation theory gives an exact result in this case, since only when the perturbation acts just once can the system go from initial to final state. The matrix element for scattering of a pion from state  $p$  to state  $p'$  is therefore

$$(3) \quad \langle p' | V_p | \rangle ;$$

the states in (3) are eigenstates of the unperturbed Hamiltonian which includes the self field; the nucleon variables have been suppressed for brevity.

As an alternative description of the scattering, consider the process of Fig. 1(d), absorption and emission of external pions. Again take as the perturbation the interaction of the external pions only. Then second-order perturbation theory gives an exact result:

$$(4) \quad - \sum_n \left[ \frac{\langle |V_{p'}^*|n\rangle \langle n|V_p| \rangle}{E_n - q_0 - p_0} + \frac{\langle |V_p|n\rangle \langle n|V_{p'}^*| \rangle}{E_n - q_0 + p_0} \right]$$

the sum is over all eigenstates  $n$  of the unperturbed Hamiltonian, i.e., over all states of the nucleon and its self field;  $q_0$  is the initial energy of the nucleon. Equating (3) and (4) gives the oft-derived covariant Low equation. See, for example, equation (6) of a recent paper by Amati and Vitale (1957).

### III. BARYON STATES

In what follows it is convenient to regard hyperons and nucleons as states of a single particle—the baryon. The interaction of the pion field with this baryon field can still be decomposed as in (1a). Then  $V_p$  (and  $V_p^*$ ) contains as a factor an operator connecting different baryon states. According to the Nishijima-Gell-Mann scheme for strong interactions this operator must be a vector  $\bar{A}$  in isotopic spin space and cannot connect baryon states of different strangeness; this restricts  $\bar{A}$  to be a linear combination of four terms, the isotopic spins  $\bar{\tau}_N, \bar{\tau}_\Sigma, \bar{\tau}_\Xi$  for nucleon,  $\Sigma$  and  $\Xi$  states respectively, and the operator  $\bar{\nu}$  connecting  $\Lambda$  and  $\Sigma$  states. The components of  $\bar{\nu}$  are defined by the equations

$$(5) \quad \nu_+ \Lambda = -\sqrt{2} \Sigma^+, \quad \nu_- \Lambda = \sqrt{2} \Sigma^-, \quad \nu_0 \Lambda = \Sigma^0,$$

and their Hermitian conjugates. Similarly the coupling of  $K$ -mesons to baryons defines a baryon operator  $U_k$ ; it contains as a factor a spinor  $B$  in isotopic spin space which connects nucleon and  $\Xi$  states to  $\Lambda$  and  $\Sigma$  states. This notation is discussed at greater length by Sharp and Gupta (1959).

### IV. $K$ -MESON SCATTERING AND ASSOCIATED PRODUCTION

For  $K$ -meson scattering the treatment is similar to that for pions. Postulate three  $K$ -meson fields, a self field and incident and outgoing external fields. To take account of virtual pions, include a self pion field in the Hamiltonian. Treat interactions of external fields with the baryon as the perturbation. Then the matrix element for absorption of an external  $K$ -meson and emission of a self  $K$ -meson is

$$(6) \quad \langle k' | U_k | \rangle.$$

The matrix element for absorption and emission of external  $K$ -mesons is

$$(7) \quad - \sum_n \left[ \frac{\langle |U_{k'}^*|n\rangle \langle n|U_k| \rangle}{E_n - q_0 - k_0} + \frac{\langle |U_k|n\rangle \langle n|U_{k'}^*| \rangle}{E_n - q_0 + k_0} \right].$$

Equating (6) and (7) gives the covariant Low equation for  $K$ -meson scattering, equation (17) of Amati and Vitale (1957). The Low equation for  $\bar{K}$ -meson scattering, equation (24) of Amati and Vitale, follows in the same way.

To treat associated production of a  $K$ -meson and a hyperon from a pion and a nucleon, use two  $K$ -meson fields, a self field and an outgoing external field, and two pion fields, a self field and an incident external field. The matrix element for absorption of a self pion with emission of an external  $K$ -meson is

$$(8) \quad \langle |U_k^*|p \rangle;$$

the matrix element for absorption of an external pion with emission of a self  $K$ -meson is

$$(9) \quad \langle k|V_p| \rangle;$$

the matrix element for absorption of an external pion and emission of an external  $K$ -meson is

$$(10) \quad - \sum_n \left[ \frac{\langle |U_k^*|n \rangle \langle n|V_p| \rangle}{E_n - q_0 - p_0} + \frac{\langle |V_p|n \rangle \langle n|U_k^*| \rangle}{E_n - q_0 + p_0} \right].$$

Equating (8), (9), and (10) gives two forms of the Low equation for associated production. See equation (11) of Amati and Vitale.

Low type equations for other scattering and production processes including multiple meson production are easily derived by this method.

#### V. NUCLEON-NUCLEON INTERACTION

Consider the scattering of two nucleons by the exchange of pions. A Hamiltonian which describes this is given by equation (1). The matrix element for the process is illustrated by the Feynman diagram of Fig. 2. The nucleon part of this diagram consists of two open nucleon lines which are continuous

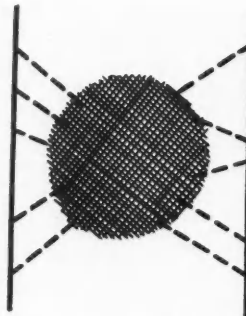


FIG. 2. Scattering of two nucleons by exchange of pions.

from bottom to top, together with any number of closed loops (in the shaded area). These nucleon lines are joined by any number of pion lines.

Now reformulate the problem by postulating two identical nucleon fields and two pion fields. Each nucleon has its own pion field, the quanta of which

it emits and absorbs, and, in addition, each absorbs the quanta of the field of the other. The new Hamiltonian is

$$(11) \quad H_{N1} + H_{N2} + H_1 + H_2 + \mathfrak{H}_1^1 + \mathfrak{H}_2^2 + \mathfrak{H}_1^{2(-)} + \mathfrak{H}_2^{1(-)},$$

where  $H_{N1}$ ,  $H_{N2}$ ,  $H_1$ ,  $H_2$  describe the noninteracting nucleon and pion fields and  $\mathfrak{H}_1^1$ ,  $\mathfrak{H}_2^2$ ,  $\mathfrak{H}_1^{2(-)}$ ,  $\mathfrak{H}_2^{1(-)}$  are respectively

$$(11a) \quad \mathfrak{H}_1^1 = \sum_p a_p^{(1)*} V_p^{(1)*} + \sum_p a_p^{(1)} V_p^{(1)},$$

$$(11b) \quad \mathfrak{H}_2^2 = \sum_p a_p^{(2)*} V_p^{(2)*} + \sum_p a_p^{(2)} V_p^{(2)},$$

$$(11c) \quad \mathfrak{H}_1^{2(-)} = \sum_p a_p^{(1)} V_p^{(2)},$$

$$(11d) \quad \mathfrak{H}_2^{1(-)} = \sum_p a_p^{(2)} V_p^{(1)}.$$

Consider the scattering of a nucleon of field 1 by a nucleon of field 2. The  $S$ -matrix element is not quite the same as that for the nucleon-nucleon scattering described by the Hamiltonian (1) and illustrated in Fig. 2. The difference, apart from the trivial one that the open nucleon lines are labelled 1 and 2, is that closed loops can now belong to either field 1 or field 2; this leads to duplicated diagrams. The difficulty is resolved by a suitable convention about the identity of nucleons in closed loops; this is discussed further below.

To use the scheme as an aid to calculation, one now treats  $\mathfrak{H}_1^{2(-)} + \mathfrak{H}_2^{1(-)}$  as the perturbation. Then  $n$ th order perturbation theory takes account of exchanges of up to  $n$  pions between the nucleons.

Any convention which makes the labelling of nucleons in closed loops unique is theoretically satisfactory in the sense that it ensures the "equivalence" of Hamiltonians (1) and (11). In practice it is important that a closed loop or loops connected by pion lines only to the open nucleon line 1 or 2 should be labelled 1 or 2 respectively. Then in the perturbation calculation of the preceding paragraph the eigenstates of the unperturbed Hamiltonian are simply direct products of eigenstates involving one nucleon; the nucleons are uncoupled in zero order. The matrix elements for nucleon-nucleon scattering are expressible in terms of the vertex functions and matrix elements appearing in the pion-nucleon scattering problem (equation (4)). It is convenient to label a closed loop or loops in a pion self-energy part so that the two ends of the part belong to the same pion field. For other closed loops the labelling could be symmetrized with respect to 1 and 2.

Another formulation makes use of four pion fields. Each nucleon has its own self field the pions of which it emits and absorbs; but instead of allowing each to absorb the pions of the other, introduce two external fields, emitted by 1 and absorbed by 2, and emitted by 2 and absorbed by 1 respectively. Again a convention about closed loops is needed.  $2n$ th order perturbation theory describes the exchange of  $n$  pions. This formulation is preferable when it is desired to split off terms corresponding to iterated lower order diagrams.

These considerations are easily generalized to include scattering of baryons by exchange of pions and  $K$ -mesons.

## ACKNOWLEDGMENTS

The author thanks his former colleagues at Imperial College, and especially P. T. Matthews, for helpful discussions. He thanks the Nuffield Foundation for financial assistance in the form of a Dominion Travelling Fellowship.

## REFERENCES

AMATI, D. and VITALE, B. 1957. *Nuovo cimento*, **6**, 1273.  
SHARP, R. T. 1958. *Nuovo cimento*, **9**, 23.  
SHARP, R. T. and GUPTA, M. L. 1959. Submitted to *Nuovo cimento*.

---

## NOTES

---

### THE NOSE-ON RADAR CROSS SECTIONS OF CONDUCTING RIGHT CIRCULAR CONES

J. E. KEYS AND R. I. PRIMICH

To the knowledge of the authors, an exact expression for the nose-on radar cross section of a conducting right circular cone has never been published. Various approximations exist for the Rayleigh region where the base diameter is less than about one-quarter wavelength, and for the resonant region where the base diameter lies between one-quarter and about five wavelengths (Siegel 1957).

To check these approximations, a series of measurements has been made on cones whose diameters lay between about one-tenth and three wavelengths and whose total included nose angles lay between  $8^\circ$  and the limiting case of a thin disk ( $180^\circ$ ). Since theories for the resonant region usually assume that the chief contribution to the cross section comes from the sharply discontinuous ring at the base, a series of wire loops was measured at normal incidence for comparison. The measurements were made at wavelengths of 0.8565 cm and 3.426 cm on a modified balanced hybrid tee system to be described in a future publication. The minimum detectable cross section is about 0.0005 square wavelength. The results are reproducible to within 1 decibel in power or  $10 \log \sigma$  where  $\sigma$  is the radar cross section of the target.

The results are shown in Fig. 1 where the cross section in decibels relative

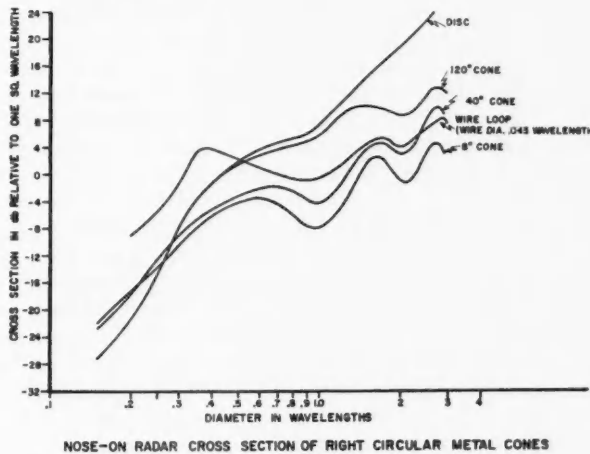


FIG. 1.

to the one square wavelength is plotted as a function of base diameter, measured in wavelengths.

It will be noted that, as predicted, the cone resonance can be approximated by the resonance of the wire loop except for the position of the first maximum. In the Rayleigh region, it is usually assumed that the cross section varies as the square of the volume. This would mean, for example, that the 8° cone should have a cross section 28 decibels higher than the 120° cone. It can be seen from the curves, however, that although the small angle cone has a higher cross section, the difference is only 4 or 5 decibels at the most. This seems to indicate that the approximation should be modified to place more emphasis on the projected area rather than on the volume.

It is hoped, in the near future, to publish the complete results on the cross section of a cone as a function of aspect angle, polarization, nose angle, and diameter.

SIEGEL, K. M. 1957. Far field scattering from bodies of revolution. Paper delivered at URSI XII General Assembly in Boulder, Colorado.

RECEIVED DECEMBER 18, 1958.  
DEFENCE RESEARCH TELECOMMUNICATIONS ESTABLISHMENT,  
DEFENCE RESEARCH BOARD,  
DEPARTMENT OF NATIONAL DEFENCE,  
OTTAWA, ONTARIO.

#### NUCLEAR MAGNETIC RESONANCE IN LEAD-CONTAINING COMPOUNDS

J. M. ROCARD, M. BLOOM, AND L. B. ROBINSON<sup>1</sup>

The purpose of this research is to investigate the diamagnetic (or paramagnetic) shifts and nuclear spin-spin interactions in compounds containing heavy atoms; both effects (Bloembergen and Rowland 1955; Ramsey 1952), which depend on the electron density, are greatly enhanced in systems involving heavy atoms. Thus, for example, among the compounds which we have studied the resonance frequency of  $Pb^{207}$  differs by about 1.6% of the average frequency, as compared with about  $3 \times 10^{-4}\%$  for protons in organic compounds.

The results for the ratio of the  $Pb^{207}$  resonance frequency to that of deuterium in  $D_2O[\nu(Pb^{207})/\nu(D^2)]$  in different compounds are summarized in Table I and are mostly in agreement with those reported by Piette and Weaver (1958). A conventional crossed-coil spectrometer for the observation of  $\chi'$  was used in all these measurements. In our experiments, the frequency of our oscillator could be adjusted to a fixed value (between 2.5 and 4.5 Mc/sec) and the field  $H_0$  is slowly swept through resonance.

#### *Line Widths and Line Shapes*

The line widths  $\Delta H$  defined in Fig. 1 and reported in Table I are all larger

<sup>1</sup>Present address: Atomic Energy of Canada Ltd., Chalk River, Ontario.

TABLE I\*

Compound	$r = [\nu(\text{Pb}^{207})/\nu(\text{D}^2)]$	$\Delta H$ , gauss	$\delta = [(r_0 - r)/r_0] \times 100\%$	Piette and Weaver (1958)
Pb metal	$r_0 = 1.379$	4	0	0
PbO <sub>2</sub> powder	90% 94% 98%†	1.371 1.370 1.369 <sub>5</sub>	6.5 +0.58 +0.65 +0.69	+0.63
Pb(C <sub>2</sub> H <sub>4</sub> O <sub>2</sub> ) <sub>2</sub> ·3H <sub>2</sub> O single crystal	1.364	2.5	+1.09	
Pb(C <sub>2</sub> H <sub>4</sub> O <sub>2</sub> ) <sub>2</sub> ·3H <sub>2</sub> O solution	1.362	2	+1.23	+1.26
PbCl <sub>2</sub> crystalline powder	1.360	5	+1.38	+1.23
PbCO <sub>3</sub> single crystal	1.359	2.5	+1.44	
PbSO <sub>4</sub> crystalline powder	1.358	3.2	+1.52	+1.47
Pb(NO <sub>3</sub> ) <sub>2</sub> solution	1.359	2	+1.44	+1.41
Pb(NO <sub>3</sub> ) <sub>2</sub> ·H <sub>2</sub> O	1.358	3.3	+1.52	
Pb(NO <sub>3</sub> ) <sub>2</sub> crystalline powder	98% ?†	1.358 1.357	+1.52 +1.59	+1.46
Precision		$\Delta r = \pm 0.0004$	$\Delta \delta = \pm 0.03$	
$\Delta H$ includes contribution from inhomogeneity of field				

\*  $H_0 \approx 4590$  gauss for  $\pi$  (deuterium) = 3 Mc/sec.

† Degree of purity of samples.

than expected from dipole-dipole interactions between nuclei, except possibly for the lead acetate crystal and for the PbCO<sub>3</sub> crystal. Among the possible explanations of this are: (1) an anisotropic diamagnetic shift, (2) indirect spin-spin interactions of the pseudodipolar type, (3) diamagnetic shifts which depend on the vibrational states of a molecule in molecules having long lifetimes in individual vibrational states, (4) an effect of impurities.

As has been previously pointed out, these contributions could be separated out by experiments on single crystals, by studying the temperature dependences of the resonance frequencies or, in principle, but less unambiguously, by a study of the line shapes in powders. Our signal/noise is not good enough at this time to give a reliable line shape for any of the resonances studied, but we plan to study some temperature dependences, and some preliminary results in two single crystals are reported below. Professor Bloembergen has pointed out to us that an especially interesting case is that of Pb metal which has a broad line in spite of its cubic structure (Bloembergen and Rowland 1955). In a symmetrical structure such as this, one would expect a small anisotropy in the diamagnetic shift and small pseudodipolar term in the indirect spin-spin interactions since the pseudodipolar term depends on the *p*, *d*, etc., state terms in the electron distributions as opposed to the (line-narrowing) exchange term which involves only the *S*-state terms.

Two interesting cases from the point of view of line shape are lead nitrate and lead nitrite, both of which give a more complex structure than any of the others as indicated in Fig. 1 which shows recordings of  $d\chi'/dH$ . In some runs the spectra given by these compounds were more symmetrical than shown.

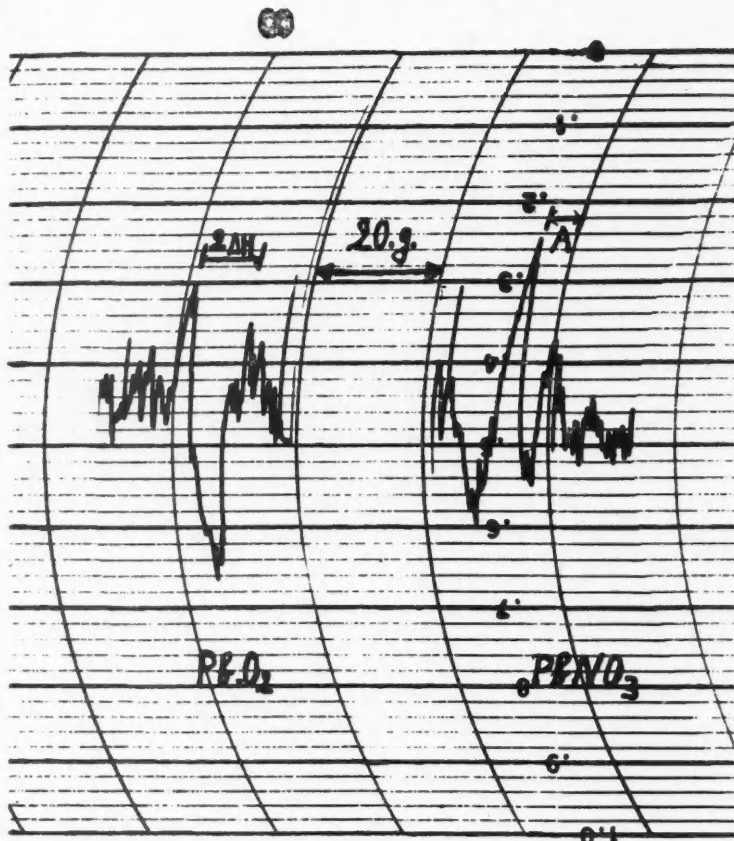


FIG. 1. Recordings of dispersion signal of  $\text{Pb}^{207}$  in lead dioxide ( $\text{PbO}_2$ ) and in lead nitrate ( $\text{Pb}(\text{NO}_3)_2$ ) (crystalline powder).

With "A" defined as in Fig. 1, we obtained  $A = 7, 2$ , and  $7$  gauss for  $\text{Pb}(\text{NO}_3)_2$  solid,  $\text{Pb}(\text{NO}_3)_2$  in  $\text{H}_2\text{O}$  solution, and  $\text{Pb}(\text{NO}_3)_2 \cdot \text{H}_2\text{O}$  solid, respectively. The structure observed in lead nitrate solution would seem to be inconsistent with the solution consisting of  $\text{Pb}^{++}$  ions.

#### *Anisotropy of the Diamagnetic Shift*

Thus far we have made measurements on two single crystals, lead acetate and lead carbonate. For both we have observed a definite anisotropy of the diamagnetic shift of the order of  $10^{-3}$  of the resonance frequency. Only the average values of the resonance frequencies in single crystals of these substances are given in Table I. It may be noted that the single crystal of  $\text{PbCO}_3$  gave a much better signal/noise than any other compound. The observed

anisotropy is to be compared with the only other anisotropy previously observed (Lauterbur 1958) ( $8.10^{-6}$ ) for the  $C^{13}$  resonance in single crystal of  $CaCO_3$ . Such anisotropies in compounds containing heavy atoms may be studied without the extreme homogeneity required for light atoms. In fact, our inability to observe resonances in  $Pb_3O_4$ ,  $PbBr_2$ ,  $PbI_2$ , and some other compounds such as lead acetate crystalline powder may be due to very large anisotropies of the diamagnetic shift causing a very broad line in samples composed of crystalline powder.

#### *Effect of Impurities*

Some of our results are not completely in agreement with those of Piette and Weaver ( $PbCl_2$  and  $Pb(NO_3)_2$  solid). This is probably due to an effect of impurities. We have observed a small but definite effect of impurity concentrations on the resonance frequencies. This is not unexpected, since the diamagnetic shift depends on the energies of excited states of electrons. In  $PbO_2$  the shift in resonance frequencies varies between  $+0.58$ ,  $+0.65$ ,  $0.69\%$  for samples having the purity factor of 90, 94, 98% respectively. Variations in stoichiometry might also be important. Our samples were taken directly from compounds supplied by chemical suppliers.

We wish to thank Mr. William Vogel, who carried out some of the measurements; Dr. H. E. Weaver for some very helpful correspondence; Dr. L. Reeves of the Chemistry Department, at University of British Columbia, for stimulating discussions; and especially Dr. G. M. Volkoff for his constant encouragement throughout this work. This research was supported by a grant to Dr. G. M. Volkoff from the National Research Council of Canada.

BLOEMBERGEN, N. and ROWLAND, T. J. 1955. *Phys. Rev.* **97**, 1697.  
LAUTERBUR, P. C. 1958. *Phys. Rev. Letters*, **1**, 343.  
PIETTE, L. H. and WEAVER, H. E. 1958. *J. Chem. Phys.* **28**, 735.  
RAMSEY, N. 1952. *Phys. Rev.* **86**, 243.

RECEIVED JANUARY 23, 1959.  
DEPARTMENT OF PHYSICS,  
UNIVERSITY OF BRITISH COLUMBIA,  
VANCOUVER, B.C.

#### THE SPECIFIC HEAT OF RUBIDIUM BETWEEN 1.2 AND $4.2^\circ K^*$

F. D. MANCHESTER†

In recent years the specific heats of several of the alkali metals have been measured at temperatures sufficiently low that values for the electronic specific heat coefficient  $\gamma$  and the Debye characteristic temperature  $\theta$  could be obtained (Parkinson and Quarrington 1955; Roberts 1957). To date,

\*Issued as N.R.C. No. 5127.

†National Research Council Postdoctorate Fellow. Present address: Department of Physics, University of Alberta, Edmonton, Alberta.

however, two of the alkali metals, rubidium and caesium, have not been measured below about  $20^{\circ}$  K (Dauphinee *et al.* 1955). This note presents data on the specific heat of one of these metals, rubidium, in the temperature range  $1.2$  to  $4.2^{\circ}$  K. These measurements were made to examine the form of the temperature dependence of the specific heat in this temperature range and to provide an estimate of  $\theta_0$ , which would serve until such time as measurements could be made below  $1^{\circ}$  K, to determine  $\theta_0$  with more certainty and also the value of  $\gamma$ .

The apparatus employed (Manchester 1959) was a cryostat of the mechanical-thermal-switch type, designed primarily for measurements of the electronic specific heats of some metals and alloys in the range above  $1^{\circ}$  K. The sample

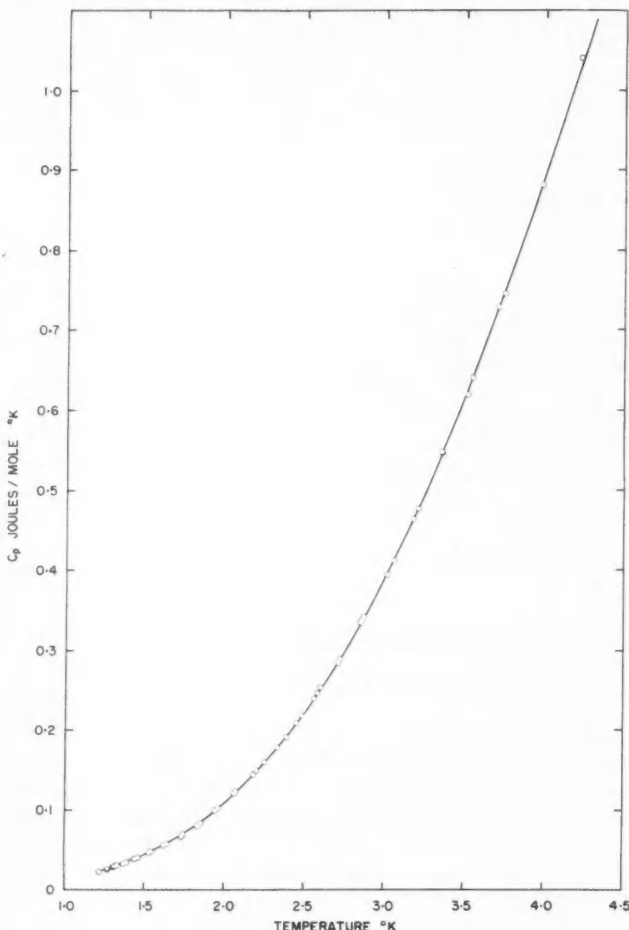


FIG. 1.  $C_p$  vs.  $T$  for rubidium.

of rubidium metal was obtained from A. D. MacKay, Inc., New York. It had a residual resistance ratio  $R_{4.2^\circ\text{K}}/R_{300^\circ\text{K}} = 2.92 \times 10^{-2}$  and spectroscopic examination showed caesium to be the main impurity. Just over 23 g of the metal was melted in glass, under vacuum, into a light copper calorimeter which was then sealed off from the atmosphere with a small metal to glass seal. A separate determination of the specific heat of the empty calorimeter was made before it was filled.

The specific heat curve obtained is shown in Fig. 1 and the corresponding curve of Debye  $\theta$  as a function of temperature in Fig. 2. From Fig. 2 it would appear that the value of  $\theta_0$  could be estimated as  $52.6^\circ\text{K}$ , making the assumption that the value of  $\theta$  would not vary greatly below  $\theta/50$  and neglecting

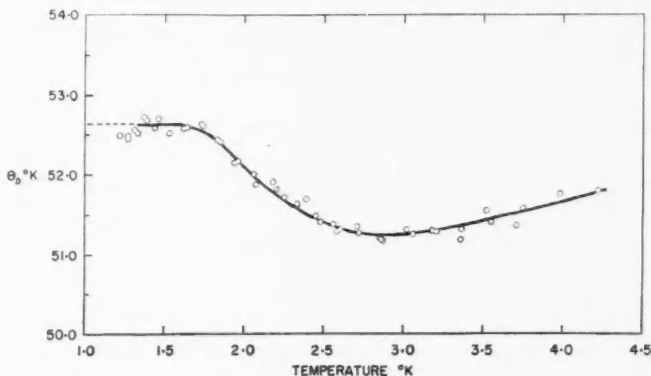


FIG. 2. Debye  $\theta$  vs.  $T$  for rubidium.

the contribution of the electrons to the total specific heat. This experimental estimate is compared with values of  $\theta_0$  obtained by other means in Table I.

TABLE I

Basis of computation	$\theta$ value, °K	Reference
Electrical resistance	65	MacDonald, White, and Woods (1956)
Previous estimate from specific heat at $25^\circ\text{K}$	61	Dauphinee <i>et al.</i> (1955)
Calculated from elastic constants	50.9	Fuchs (1936); de Launay (1954)
Experimental value at $1.2^\circ\text{K}$	52.6	This work

The elastic constants for rubidium were calculated using the method of Fuchs (1936a, b) and the compressibility data obtained by Swenson (1955). The value of  $\theta_0$  was obtained from the elastic constants using case (2) of the tables of de Launay (1954).

I am grateful to Miss Lorraine Peters for help with the calculation of the experimental results and to Miss Adele Castella for computing the theoretical value of  $\theta_0$ .

DAUPHINEE, T. M., MARTIN, D. L., and PRESTON-THOMAS, H. 1955. Proc. Roy. Soc. (London), A, **233**, 214.  
 FUCHS, K. 1936a. Proc. Roy. Soc. (London), A, **153**, 622.  
 ——— 1936b. Proc. Roy. Soc. (London), A, **157**, 444.  
 DE LAUNAY, J. 1954. J. Chem. Phys. **22**, 1676.  
 MACDONALD, D. K. C., WHITE, G. K., and WOODS, S. B. 1956. Proc. Roy. Soc. (London), A, **235**, 358.  
 MANCHESTER, F. D. 1959. To be published.  
 PARKINSON, D. H. and QUARRINGTON, J. E. 1955. Proc. Phys. Soc. (London), A, **68**, 762.  
 ROBERTS, L. M. 1957. Proc. Phys. Soc. (London), B, **70**, 744.  
 SWENSON, C. A. 1955. Phys. Rev. **99**, 423.

RECEIVED JANUARY 22, 1959.  
 DIVISION OF PURE PHYSICS,  
 NATIONAL RESEARCH COUNCIL,  
 OTTAWA, CANADA.

### THE EFFECTIVE HALF-LIVES OF Cs AND I IN THE BODY

K. G. MCNEILL AND R. M. GREEN

Information on the retention of chemicals in the body may be obtained by measuring the apparent decay of a radionuclide introduced into the body. The effective half-life,  $\tau_E$ , is connected to the nuclear half-life,  $\tau_N$ , and the biological half-life,  $\tau_B$ , by the relationship  $1/\tau_E = 1/\tau_N + 1/\tau_B$ . Apart from individual variation,  $\tau_B$  should only depend on the chemical considered.

The half-life for the retention of caesium in the body has been in dispute. In the National Bureau of Standards Handbook 52 (1953) the figure quoted for  $\text{Cs}^{137}$  is 17 days, whereas Miller (1956) found that with  $\text{Cs}^{134}$  the biological half-life was approximately 100 days, in agreement with work at Los Alamos.

The opportunity afforded by a caesium accident at Toronto was taken to measure the effective half-life for  $\text{Cs}^{137}$ , using a whole body counter (to be more fully described elsewhere). The detector was a 5-in. NaI crystal, feeding into a 100-channel pulse height analyzer. In the measurements, only counts in the 0.66-Mev photopeak of the Cs spectrum were accepted. Shielding was provided by a steel room, 5 ft  $\times$  6 ft  $\times$  7 ft with 8-in. walls, similar in construction to that at the Argonne National Laboratories.

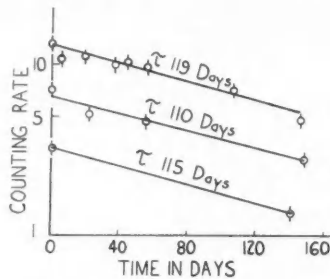


FIG. 1. A semilogarithmic plot of the counting rate of humans with an abnormal caesium body burden versus time in days. The counting rate scale is arbitrary.

The body content of caesium was measured in three subjects over a period of 140 days, and the results are shown graphically in the figure. In the case of the two subjects with most activity a number of counts was taken to establish the exponential nature of the decay, whereas the third subject served merely as a check on the half-life obtained with the first two.

It will be seen that the half-lives in the three cases are 119 days, 110 days, and 115 days. This is in agreement with the Argonne results and in disagreement with the figure given in the NBS handbook.

A check on the results of previous work (National Bureau of Standards Handbook 52, 1953) has also been obtained from three normal subjects who, for the purposes of an experiment on thyrotoxicosis, ingested  $I^{131}$ . After a period of 3 days, to allow for the initial excretion of inorganic iodine, their iodine gamma activity was measured as a function of time over a period of 50 days. To test the internal consistency of the detection apparatus, the counts from the 0.36-Mev and 0.64-Mev photopeaks were considered separately. For the stronger 0.36-Mev line,  $\tau_E$  was found to be 8.0, 7.8, and 8.1 days in the three cases, while the weaker 0.64-Mev line gave results of 8.2, 8.1, and 8.5 days.

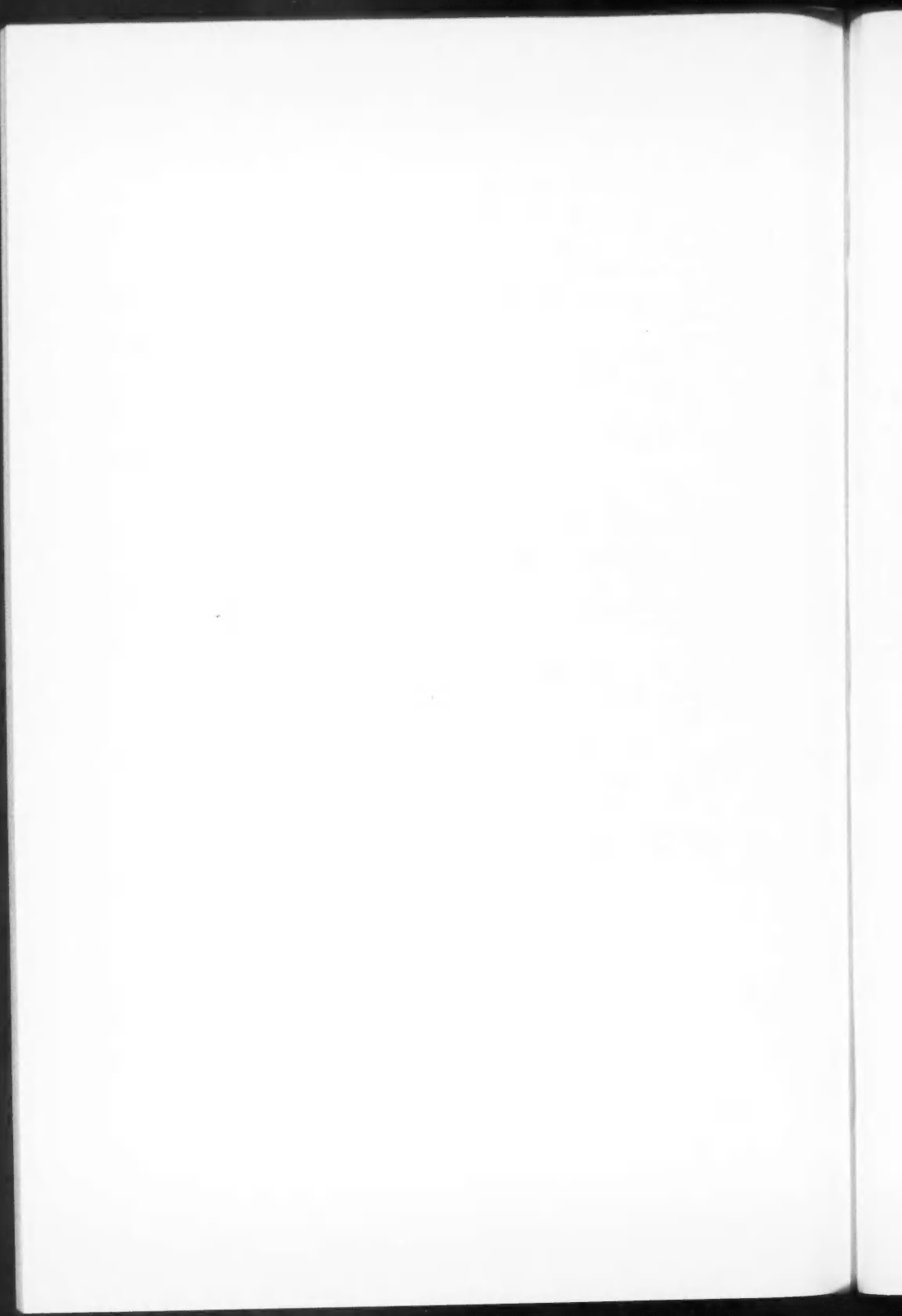
Bearing in mind that  $\tau_N$  for  $I^{131}$  is 8.1 days, this result indicates that the biological half-life for I in the body is much greater than 8 days, in agreement with previous results in this field.

#### ACKNOWLEDGMENTS

We wish to acknowledge, with thanks, a grant from the Department of Health and Welfare of the Dominion of Canada which enabled this work to be done.

MILLER, C. E. 1956. Measurements of gamma rays in vivo. Argonne National Laboratory Reports, No. 5596.  
NATL. BUR. STANDARDS (U.S.), HANDBOOK. 1953. No. 52. Maximum permissible amounts of radio-isotopes in the human body.

RECEIVED SEPTEMBER 29, 1958.  
DEPARTMENT OF PHYSICS,  
UNIVERSITY OF TORONTO,  
TORONTO, ONTARIO.



## THE PHYSICAL SOCIETY

MEMBERSHIP of the Society is open to all who are interested in Physics. FELLOWS pay an Entrance Fee of £1 1s. (\$3.15) and an Annual Subscription of £2 2s. (\$6.00).

STUDENTS: A candidate for Studentship must be between the ages of 18 and 26, and pays an Annual Subscription of 5s. (\$0.75).

MEETINGS: Fellows and Students may attend all Meetings of the Society including the annual Exhibition of Scientific Instruments and Apparatus.

PUBLICATIONS include the *Proceedings of the Physical Society*, published monthly, and *Reports on Progress in Physics*, published annually. Volume XXI, 1958, is now available (price £3 3s. (\$9.45)). Members are entitled to receive any of the Publications at a reduced rate.

Further information can be obtained from:

THE PHYSICAL SOCIETY  
1, LOWTHER GARDENS, PRINCE CONSORT ROAD  
LONDON, S.W.7, ENGLAND



## NOTES TO CONTRIBUTORS

### *Canadian Journal of Physics*

#### MANUSCRIPTS

**General.**—Manuscripts, in English or French, should be typewritten, double spaced, on paper  $8\frac{1}{2} \times 11$  in. **The original and one copy are to be submitted.** Tables and captions for the figures should be placed at the end of the manuscript. Every sheet of the manuscript should be numbered. Style, arrangement, spelling, and abbreviations should conform to the usage of recent numbers of this journal. Greek letters or unusual signs should be written plainly or explained by marginal notes. Characters to be set in boldface type should be indicated by a wavy line below each character. Superscripts and subscripts must be legible and carefully placed. Manuscripts and illustrations should be carefully checked before they are submitted. Authors will be charged for unnecessary deviations from the usual format and for changes made in the proof that are considered excessive or unnecessary.

**Abstract.**—An abstract of not more than about 200 words, indicating the scope of the work and the principal findings, is required, except in Notes.

**References.**—References should be listed **alphabetically by authors' names**, unnumbered, and typed after the text. The form of the citations should be that used in current issues of this journal; in references to papers in periodicals, titles should not be given and only initial page numbers are required. The names of periodicals should be abbreviated in the form given in the most recent *List of Periodicals Abstracted by Chemical Abstracts*. All citations should be checked with the original articles and each one referred to in the text by the authors' names and the year.

**Tables.**—Tables should be numbered in roman numerals and each table referred to in the text. Titles should always be given but should be brief; column headings should be brief and descriptive matter in the tables confined to a minimum. Vertical rules should not be used. Numerous small tables should be avoided.

#### ILLUSTRATIONS

**General.**—All figures (including each figure of the plates) should be numbered consecutively from 1 up, in arabic numerals, and each figure referred to in the text. The author's name, title of the paper, and figure number should be written in the lower left corner of the sheets on which the illustrations appear. Captions should not be written on the illustrations.

**Line drawings.**—Drawings should be carefully made with India ink on white drawing paper, blue tracing linen, or co-ordinate paper ruled in blue only; any co-ordinate lines that are to appear in the reproduction should be ruled in black ink. Paper ruled in green, yellow, or red should not be used. All lines must be of sufficient thickness to reproduce well. Decimal points, periods, and stippled dots must be solid black circles large enough to be reduced if necessary. Letters and numerals should be neatly made, preferably with a stencil (**do NOT use typewriting**) and be of such size that the smallest lettering will be not less than 1 mm high when the figure is reduced to a suitable size. Many drawings are made too large; originals should not be more than 2 or 3 times the size of the desired reproduction. Whenever possible two or more drawings should be grouped to reduce the number of cuts required. In such groups of drawings, or in large drawings, full use of the space available should be made; the ratio of height to width should conform to that of a journal page ( $4\frac{1}{2} \times 7\frac{1}{2}$  in.), but allowance must be made for the captions. **The original drawings and one set of clear copies (e.g. small photographs) are to be submitted.**

**Photographs.**—Prints should be made on glossy paper, with strong contrasts. They should be trimmed so that essential features only are shown and mounted carefully, with rubber cement, on white cardboard, with no space between those arranged in groups. In mounting, full use of the space available should be made. **Photographs are to be submitted in duplicate;** if they are to be reproduced in groups one set should be mounted, the duplicate set unmounted.

#### REPRINTS

A total of 50 reprints of each paper, without covers, are supplied free. Additional reprints, with or without covers, may be purchased at the time of publication.

Charges for reprints are based on the number of printed pages, which may be calculated approximately by multiplying by 0.6 the number of manuscript pages (double-spaced typewritten sheets,  $8\frac{1}{2} \times 11$  in.) and including the space occupied by illustrations. Prices and instructions for ordering reprints are sent out with the galley proof.

## Contents

<i>J. C. Roy and L. P. Roy</i> —Radioactive decay of $Au^{200}$ - - - - -	385
<i>J. E. Evans, B. B. Kinsey, and B. G. Whitmore</i> —Measurement of the energies of nuclear states excited by inelastic neutron scattering, and a search for electric monopole transitions in $Pb$ - - - - -	396
<i>William Woodside</i> —Water vapor permeability of porous media - - - - -	413
<i>J. A. Bland</i> —The thermal expansion of cubic barium titanate ( $BaTiO_3$ ) from $350^\circ C$ to $1050^\circ C$ - - - - -	417
<i>E. H. McLaren</i> —Intercomparison of 11 resistance thermometers at the ice, steam, tin, cadmium, and zinc points - - - - -	422
<i>Ll. G. Chambers</i> —Solution of the Hund gravitational equations - - - - -	433
<i>C. D. Niven</i> —The change of resistance of hydrophilic films subjected to constant voltage - - - - -	438
<i>E. R. Pounder and E. M. Little</i> —Some physical properties of sea ice. I. - - - - -	443
<i>H. J. Fink</i> —Quasi-persistent currents in rings composed of superconducting and non-superconducting regions - - - - -	474
<i>H. J. Fink</i> —The destruction of superconductivity in tantalum wires by a current - - - - -	485
<i>E. L. Holmes and W. C. Winegard</i> —Normal grain growth in zone-refined high-purity metals - - - - -	496
<i>J. P. Roalsvig and R. N. H. Haslam</i> —Absolute $\beta$ -counting in a proportional flow-counter - - - - -	499
<i>R. T. Sharp</i> —Self and external meson fields - - - - -	515
Notes:	
<i>J. E. Keys and R. I. Primich</i> —The nose-on radar cross sections of conducting right circular cones - - - - -	521
<i>J. M. Rocard, M. Bloom, and L. B. Robinson</i> —Nuclear magnetic resonance in lead-containing compounds - - - - -	522
<i>F. D. Manchester</i> —The specific heat of rubidium between $1.2$ and $4.2^\circ K$ - - - - -	525
<i>K. G. McNeill and R. M. Green</i> —The effective half-lives of $Cs$ and $I$ in the body - - - - -	528

